

Growth and characterization of InGaN-based solar cells

LEE Seunga

Growth and characterization of InGaN-based solar cells

LEE Seunga

Nagoya University

Graduate School of Engineering

Department of Electrical Engineering and Computer Science

InGaN 系太陽電池の成長および特性研究

李昇我

名古屋大学大学院

工学研究科

電子情報システム専攻電子工学分野

ABSTRACT OF THIS THESIS

Title: Growth and characterization of InGaN-based solar cells

LEE Seunga

Thesis Advisor: Professor Hiroshi Amano

In this thesis, the growth and characterization of InGaN-based solar cells were studied to obtain essential information about the development of highly efficient solar cells. First, a simple p-GaN/i-In_xGa_{1-x}N/n-GaN solar cell structure was investigated numerically to understand the effect of piezoelectric fields (P_{pz}) on carrier dynamics. A reliable simulation model was obtained by comparing the experimental results with simulated results, and the same p-i-n InGaN structures were again simulated with and without the effect of P_{pz} (in the simulation, spontaneous polarization remained constant). The results for the sample with P_{pz} indicated a higher short current density (J_{sc}), a staircase-like feature in the I-V curve, a higher open circuit voltage (V_{oc}) with a lower fill factor (FF), and a reduced conversion efficiency (CE) compared to that for the sample without P_{pz} . Moreover, as the content of In, x , was increased, the V_{oc} value gradually increased, whereas J_{sc} significantly decreased, leading to reductions in the CE and FF values for the structure with P_{pz} . As a method to solve the problem of current loss, various techniques which can eliminate the P_{pz} have also been simulated. Among these techniques, semipolar (11-22) InGaN/GaN MQWs solar cells were experimentally investigated compared to the conventional polar (0001) structure. Due to the P_{pz} characteristics in the semipolar plane, the quantum-confined Stark effect was negligible in the semipolar sample, unlike in the polar sample. Moreover, the semipolar sample exhibited a

rough surface with arrowhead-like features, while the polar sample had a mirror-like surface. The rough surface morphology of the semipolar sample may result in a high J_{sc} due to the low reflectivity. The In-fluctuation effect was observed in both samples, although a higher degree was observed in the polar sample. For this reason, the semipolar sample exhibited enhanced J_{sc} and FF values. However, since the semipolar sample contained a higher defect density than the polar sample, its overall device performances, particularly V_{oc} and CE, were significantly degraded. We applied the dislocation reduction technique by adding a SiN_x insertion layer, resulting in enhanced photovoltaic properties in the resultant p-i-n InGaN/GaN heterojunction solar cell. To understand the relationship between the photovoltaic behaviors and dislocations, we also prepared a sample without the SiN_x insertion layer. Regarding optical properties, the sample with the SiN_x insertion layer exhibited less non-radiative centers and a stronger In-fluctuation effect due to the decrease in dislocation density. However, the quantum-confined Stark effect was almost negligible in both samples. Regarding electrical properties, the sample with the SiN_x insertion layer showed a reduced saturation current and increased shunt resistance due to the reduced dislocation density. The interrelation between the various photovoltaic properties ranging from V_{oc} to FF and dislocation density was further confirmed by comparing the experimental results with the numerical model.

CONTENTS

Chapter 1. Introduction & research objectives	1
1.1 Global energy consumption and its problems.....	1
1.2 Renewable energy	3
1.2.1 Why solar energy (solar cells)?.....	4
1.2.2 Si and III-V solar cells	5
1.3 InGaN for highly efficient solar cells	6
1.3.1 III-N (InGaN) material system: advantages for solar cell applications	6
1.3.2 History of InGaN-based solar cells.....	10
1.3.3 Challenges for InGaN-based solar cells.....	10
1.4 Research objectives and synopsis	13
1.5 References.....	16
Chapter 2. Experimental approaches & characterization	21
2.1 Illumination source	21
2.1.1 Solar radiation.....	21
2.1.2 Solar simulator	23
2.2 Solar cell parameters.....	24
2.3 References.....	27

Chapter 3. Effect of piezoelectric fields on carrier dynamics in InGaN-based solar cells28

3.1 Background28

3.2 Simulation models and material parameters29

3.3 Results and discussion31

 3.3.1 Confirming the simulation reliability.....31

 3.3.2 Effect of piezoelectric fields on device performance.....32

 3.3.3 Determination of V_{oc}34

 3.3.4 Examination of J_{sc} 34

 3.3.5 Staircase-like I–V feature.....36

 3.3.6 Photovoltaic behavior as a function of In-content38

 3.3.7 Various methods to control P_{pz}42

3.4 Summary43

3.5 References44

Chapter 4. Comparison between Ga-polar and semipolar InGaN-based solar cells.....46

4.1 Background46

4.2 Experimental details.....48

4.3 Results and discussion51

 4.3.1 Photovoltaic performances of polar and semipolar InGaN/GaN MQW SCs51

 4.3.2 Optical properties of polar and semipolar InGaN/GaN MQW structures52

 4.3.3 Estimation of crystal quality53

 4.3.4 Examination of QCSE.....55

 4.3.5 Evaluation of surface morphology57

 4.3.6 Determination of In-fluctuation58

4.3.7 Correlation between various characteristics and photovoltaic performance	61
4.4 Summary	63
4.5 References	64
Chapter 5. Effect of defects on the device performances of InGaN-based solar cells ...	66
5.1 Background	66
5.2 Experimental details.....	67
5.2.1 Basic properties of the prepared GaN templates.....	67
5.2.2 Basic properties of p-i-n InGaN/GaN heterostructures	68
5.2.3 Characterization	70
5.3 Results and discussion	70
5.3.1 Optical properties of planar- and SiN _x -type p-i-n InGaN/GaN heterostructures....	70
5.3.2 Evaluation of the In-fluctuation effect	73
5.3.3 Determination of photovoltaic performances	75
5.4 Summary	80
5.5 References	81
Chapter 6. Conclusion of this thesis	83
Appendix.....	85
Acknowledgements	96
Achievement List.....	97

Chapter 1

Introduction & research objectives

1.1 Global energy consumption and its problems

At present, energy is an indispensable part of our daily lives; energy and electricity, in particular, are used in various ways ranging from home electronics to transportation. Accordingly, world energy demand continues to increase due to the global population growth and economic development in developing countries. As shown in Fig. 1.1, the BP Energy Outlook 2035 projected that global energy consumption will increase by 41% in the period from 2012 to 2035. The problem is that fossil fuels (i.e., coal, oil, and natural gas) are mainly used for electricity production to satisfy the world's energy demand. Figure 1.1 shows that fossil fuels made up 87% of the world's energy consumption in 2013.

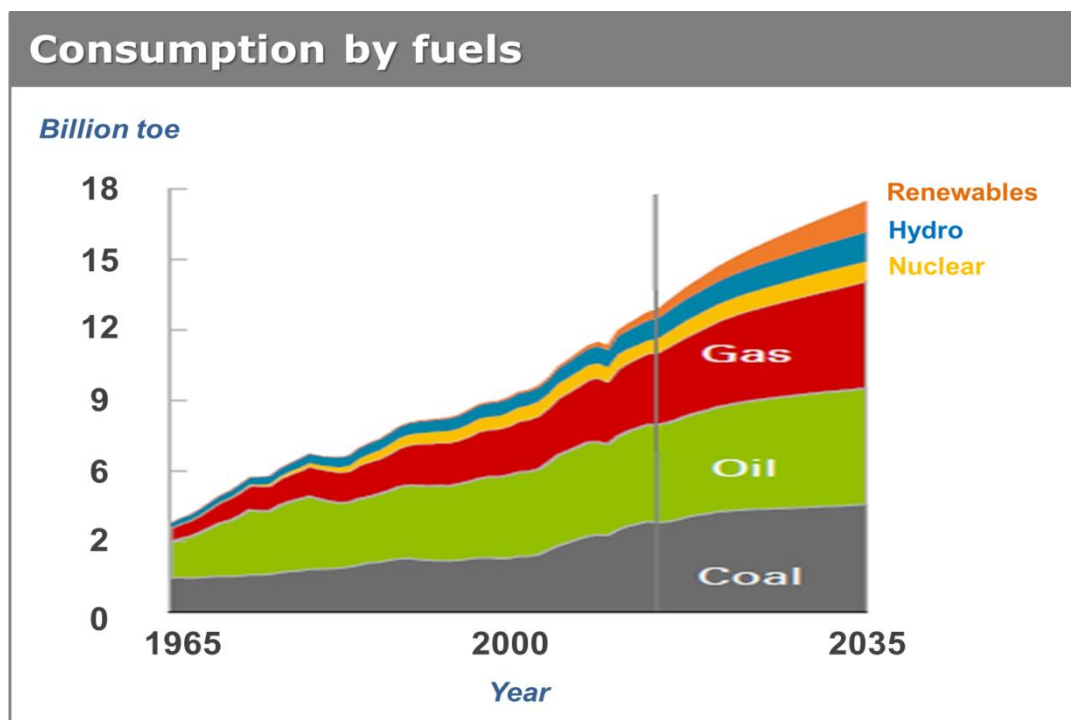


Figure 1.1 World energy demand and consumption by fuel ¹⁾

The use of fossil fuels leads to the following two serious problems: 1) environmental issues and 2) limited availability. In regards to environmental issues, burning fossil fuels for electricity production releases carbon dioxide into the atmosphere. For example, burning coal releases around 680 kg (1,500 lbs) of carbon dioxide per 1 MWh (Fig. 1.2). As a result, the average global temperature on Earth has increased by about 1.8°C. Thus, the burning of fossil fuels is causing serious global warming. Therefore in 2015 COP21, also known as the 2015 Paris Climate Conference, will, for the first time in over 20 years of UN negotiations, aim to achieve a legally binding and universal agreement on climate, with the aim of keeping global warming below 2°C. The limited availability of fossil fuels also creates severe problems. In Fig. 1.2, each circle represents the proven reserves in barrels of oil equivalent (boe), with the circle size indicating the predicted period of production remaining based on estimated production in 2013.¹⁾ As shown in this figure, since fossil fuels are finite resources, they will eventually be depleted.

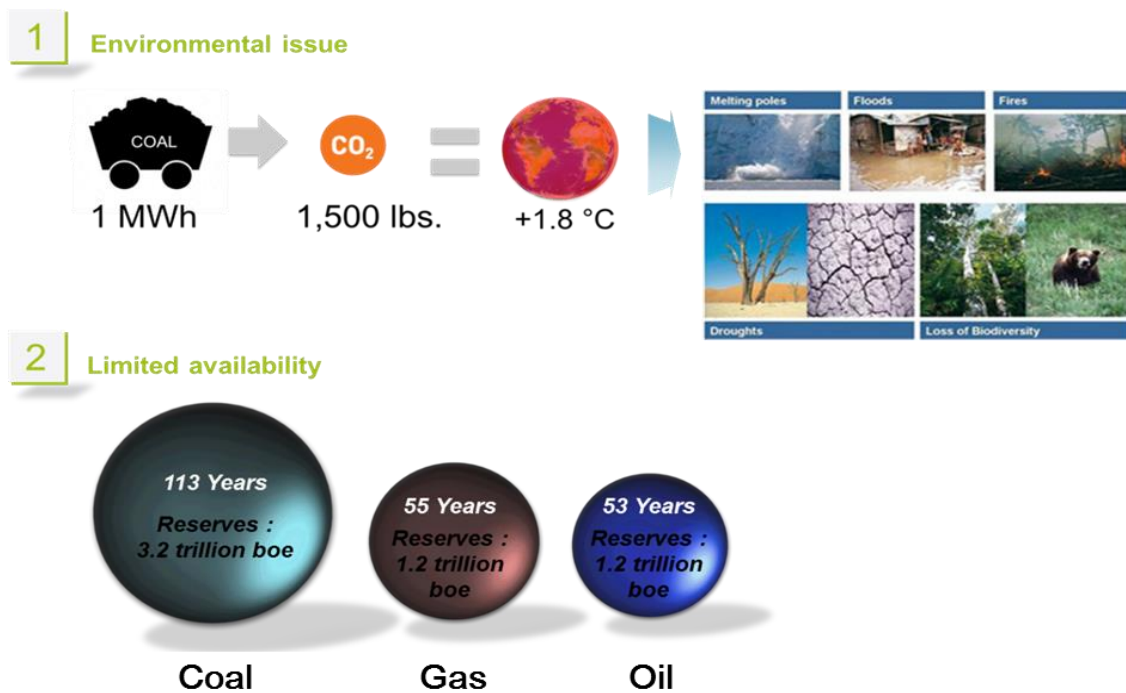


Figure 1.2 Two major problems related to fossil fuels: 1) environmental issues and 2) limited availability

1.2 Renewable energy

Renewable energy is one component of the solution to slow climate change as well as obtain secure energy sources for the future. In general, renewable energy is defined as the energy derived from resources that are naturally replenished on a human timescale, such as geothermal, solar, hydropower, ocean, biomass, and wind.²⁾ These renewable resources are the most eco-friendly forms of electricity generation; thus, environmental friendliness is an important advantage of renewable energy. As indicated in Fig. 1.3, a common source of energy used for power stations is the burning of fossil fuels to produce steam. The produced steam drives a turbine coupled to an electrical generator, and electricity is produced by electromagnetic induction. Burning the fuels contributes to global warming by increasing the amount of carbon dioxide in the atmosphere. However, we can significantly decrease carbon dioxide emissions by using renewable energy instead of fossil fuels. Moreover, renewable energy sources will be available as long as the Earth continues to exist, unlike fossil fuels, which are finite resources.

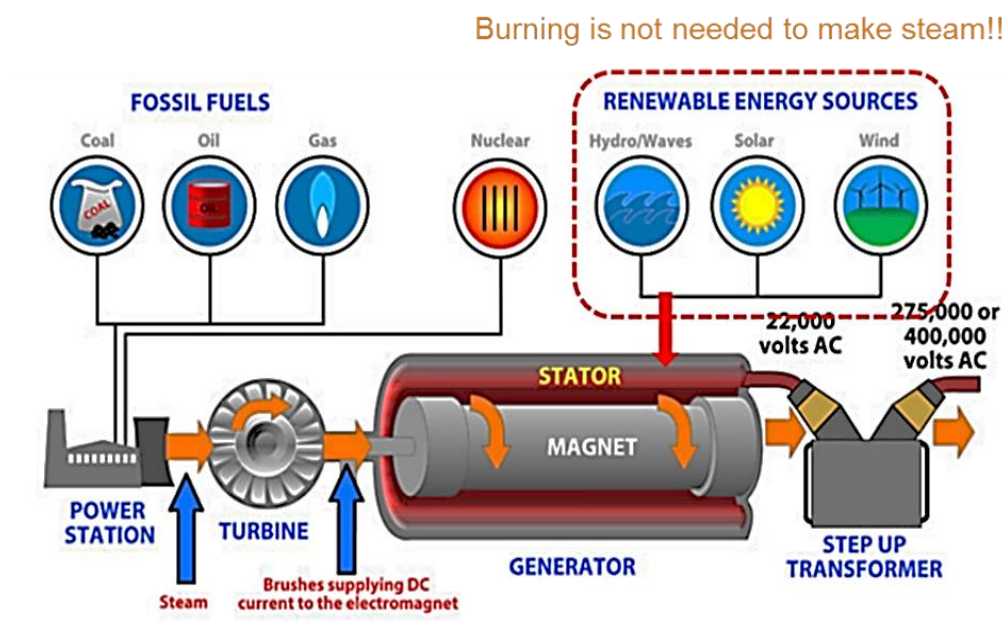


Figure 1.3 Schematic of electricity generation by fossil fuels and renewable fuels³⁾

1.2.1 Why solar energy (solar cells)?

Among the various types of renewable energy, solar energy is a promising alternative to fossil fuel energy due to its huge energy potential and environmental friendliness. In Fig. 1.4, the energy potential from renewable energy sources annually is compared to global energy consumption (the amount of produced energy is proportional to the area of the circle). This figure shows that the potential of solar energy is several orders of magnitude larger than all the other energy sources combined. Specifically, approximately 23,000 TW of power can be produced by land-based solar power generation; this power can cover the current global energy consumption of 16 TW per year.

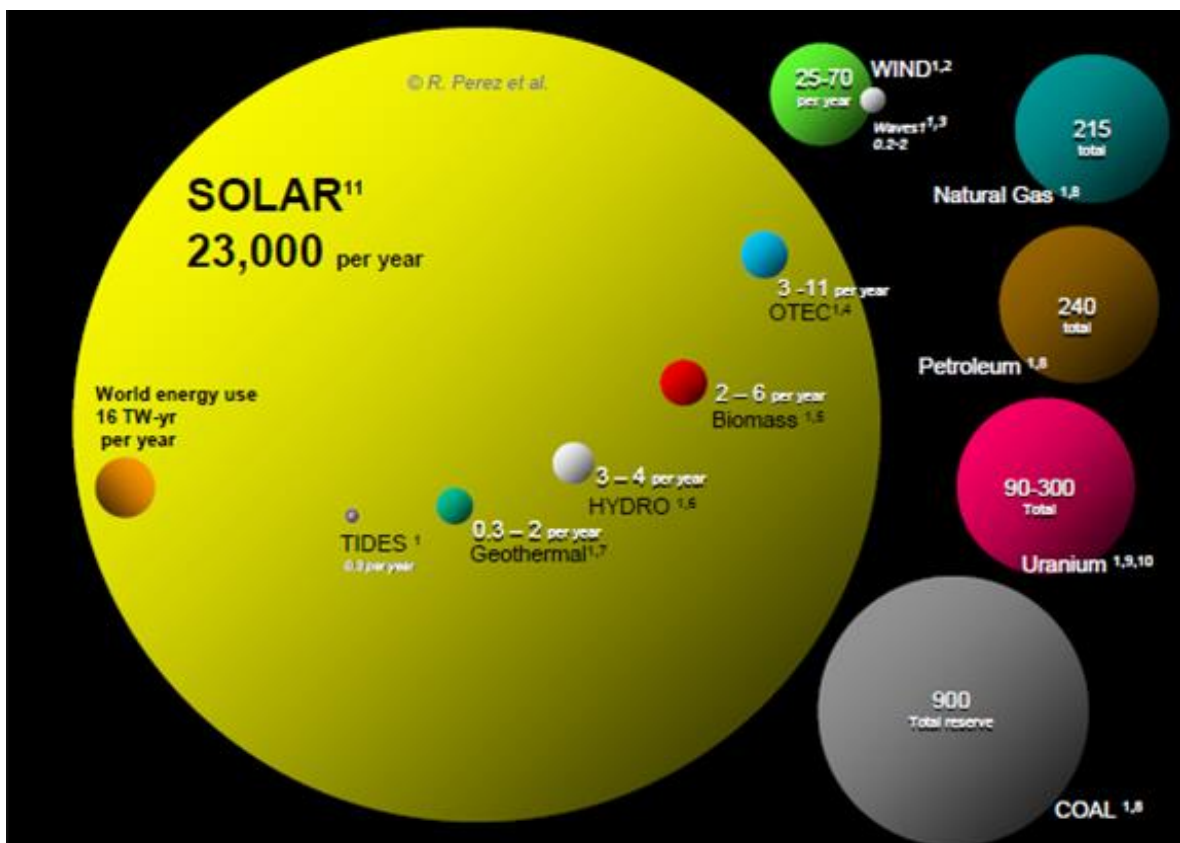


Figure 1.4 Comparison of energy potentials of renewable energy sources and various types of fossil fuels⁴⁾

Accordingly, solar energy has attracted considerable attention and has been extensively investigated. Additionally, since solar energy (sunlight) is converted into electricity directly, it is completely pollution-free. Therefore, it also has a positive effect on our society and the environment. For example, using a 25 KW solar energy system in place of fossil fuel energy for over 25 years is equivalent to the following: 1) eliminating 900 tons of carbon dioxide from the atmosphere, 2) preventing about 1.9 million km of car driving, and 3) planting about 3,000 trees.

1.2.2 Si and III-V solar cells

A solar cell is an electrical device that converts solar energy (sunlight) into electricity. Crystalline silicon (c-Si) solar cells are the most common and popular solar cells in the market because of their cost-effectiveness. However, the conversion efficiency of c-Si solar cells is limited by various indispensable losses ranging from thermalisation loss to transmission loss (Fig. 1.5(a)).

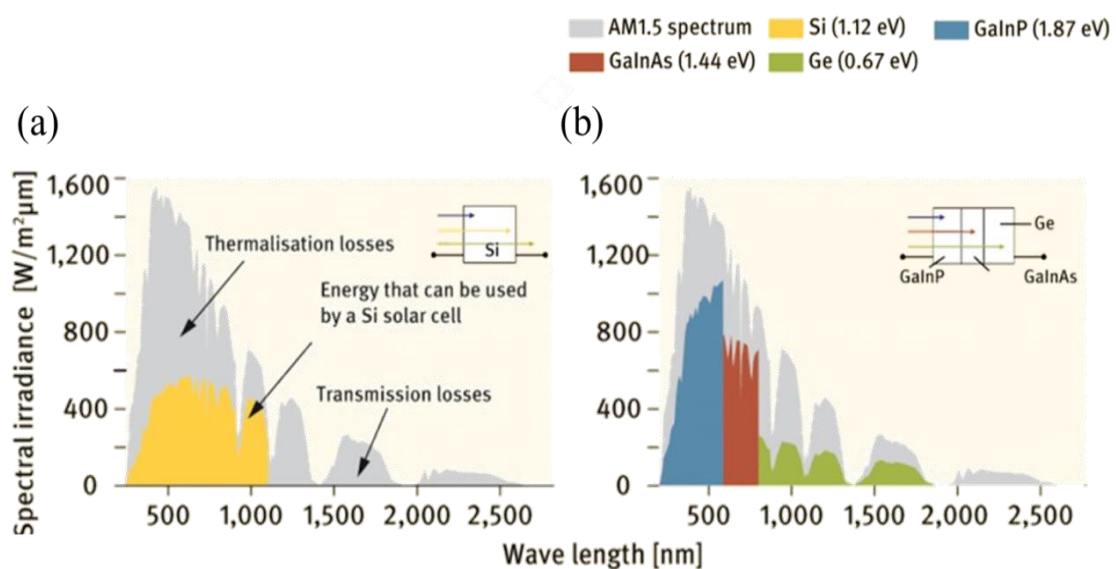


Figure 1.5 Solar spectrum with a graph that indicates the light absorbed in a (a) c-Si and (b) multi-junction solar cells⁵⁾

Therefore, c-Si solar cells are not highly efficient, with the efficiencies of standard industrial cells in the range of 15–20%, as measured under the standard 1 sun global spectrum (AM1.5G). Since the limited efficiency of a c-Si solar cell mainly originates from the single bandgap, which can absorb only a small part of the solar spectrum, multi-junction solar cells have been designed to obtain highly efficient photovoltaic energy conversion. By employing stacked p-n junctions with different bandgap energies, the solar spectrum can be more completely absorbed, as depicted in Fig. 1.5(b). Currently, the highest conversion efficiency reported using this approach is 37.9% (measured under the 1 sun and AM1.5G spectrum), which was obtained with a GaInP/GaAs/InGaAs triple-junction solar cell.⁶⁾ However, this multi-junction solar cell is very difficult to commercialize due to its complicated fabrication process and high cost; thus, it is generally used for space applications. The current efficiencies achieved by conventional single- (c-Si) and triple-junction (GaInP/GaAs/InGaAs) solar cells are close to the maximum theoretical limits; thus, recent improvements in these single- and triple-junction solar cells have been minor. Therefore, to greatly improve solar cell efficiency, new approaches are required.

1.3 InGaN for highly efficient solar cells

1.3.1 III-N (InGaN) material system: advantages for solar cell applications

The III-N material system, including InN, GaN, AlN, and their alloys, has been extensively used in light emitting diodes and laser diodes.⁷⁻⁹⁾ However, the newly discovered value of InN bandgap from 1.9 to 0.64 eV can enable the use of this material system in various new applications.¹⁰⁻¹¹⁾ In this regard, the $\text{In}_x\text{Ga}_{1-x}\text{N}$ material system is thought to be an excellent candidate for highly efficient solar cells.¹¹⁻¹²⁾ Due to the fundamental direct bandgap of the

III-N material system, particularly $\text{In}_x\text{Ga}_{1-x}\text{N}$ alloys, nearly the full solar spectrum can be covered by a single alloy as the indium (In) composition is changed (Fig. 1.6).

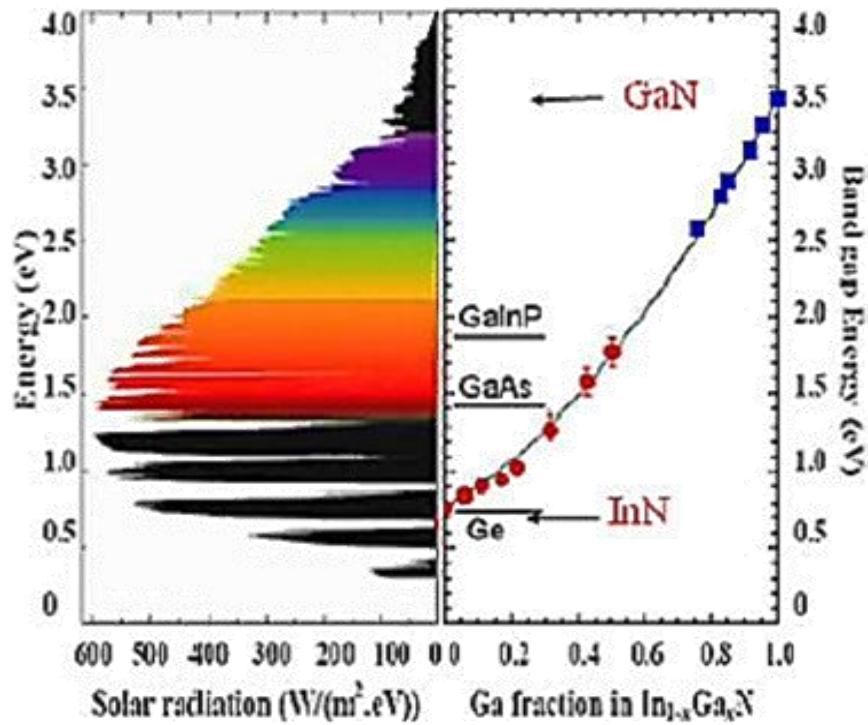


Figure 1.6 Variation in bandgap energies of $\text{In}_{1-x}\text{Ga}_x\text{N}$ alloys as a function of Ga fraction (air-mass-1.5 solar spectrum)¹²⁾

This adjustable bandgap property of the $\text{In}_x\text{Ga}_{1-x}\text{N}$ material system is also significantly beneficial for multi-junction solar cells. The detailed values of the bandgaps and the theoretical maximum efficiencies for tandem solar cells with 3–8 stacks under black-body radiation at 6000 K and 500 suns are listed in Table 1.1.¹³⁻¹⁴⁾

Table 1.1 Bandgap values and theoretical limits of tandem solar cells with 3–8 stacks ¹³⁻¹⁴⁾

No. of Stacks	Values of Bandgap (eV)								Theoretical limit η (%)
3	0.7	1.37	2						56
4	0.6	1.11	1.69	2.48					62
5	0.53	0.95	1.4	1.93	2.68				65
6	0.47	0.84	1.24	1.66	2.18	2.93			67.3
7	0.47	0.82	1.191	1.56	2	2.5	3.21		68.9
8	0.44	0.78	1.09	1.4	1.74	2.14	2.65	3.35	70.2

Table 1 shows that the ideal efficiency of the multi-junction solar cell increases as the number of stacked materials with different bandgap energies is increased. Moreover, all these efficiency values are considerably higher than those of conventional c-Si and GaInP/GaAs/InGaAs triple-junction solar cells, as shown in Fig. 1.5. To realize such high efficiency, one of the key factors is bandgap engineering. However, the number of materials that can be used to fabricate these multi-junction solar cells is fairly limited when we consider various factors such as the matching of thermal and lattice constants. Figure 1.7 shows the relation between bandgap energy and lattice parameter for the III-V material system, including the III-N system and conventional IV system.¹⁵⁾ As shown, $\text{In}_x\text{Ga}_{1-x}\text{N}$ alloy is one of the few materials that can provide a bandgap energy greater than 2.4 eV, which is essential to attain an efficiency (η) $\geq 50\%$.

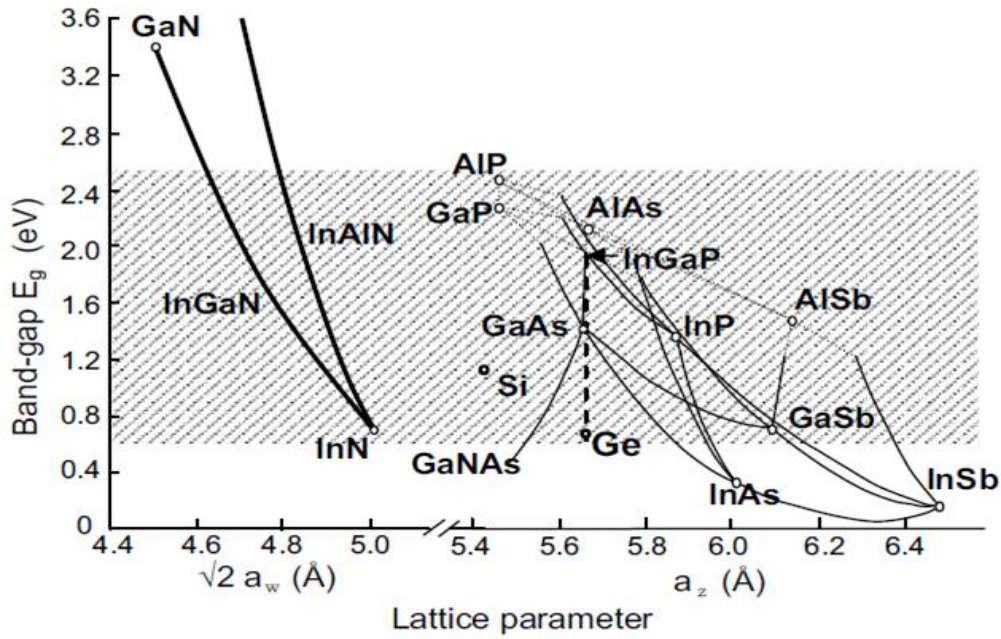


Figure 1.7 Relation between bandgap energy and lattice parameter for conventional I-V, III-V, and III-N material systems. Dashed area indicates the bandgap region of materials for tandem solar cell¹⁵⁾

The $\text{In}_x\text{Ga}_{1-x}\text{N}$ material system also exhibits several other beneficial properties such as high carrier mobility, high drift velocity, high thermal conductivity and high temperature resistance,¹⁶⁻¹⁷⁾ which will have positive impacts on solar cell operation under concentrated sunlight conditions. In particular, the higher resistance to high-energy (2 MeV) photon irradiation compared to conventional solar cell materials such as GaAs and GaInP offers great potential for radiation-hard solar cells for space applications.¹⁸⁾ For these reasons, $\text{In}_x\text{Ga}_{1-x}\text{N}$ is suitable for solar cells that can operate under harsh environmental conditions in which conventional Si-based solar cells may suffer from unstable operation. Furthermore, the high absorption coefficient of InGaN alloys ($\sim 10^5 \text{ cm}^{-1}$ at the band edge¹⁹⁻²¹⁾) can lead to the absorption of a large amount of incident sunlight in a very thin absorption layer. Due to these attractive physical properties, the InGaN material system is promising for highly efficient solar cells.

1.3.2 History of InGaN-based solar cells

In 2003, InGaN material system was firstly proposed to use for solar cell application by Lawrence Berkeley National Laboratory (LBNL).¹²⁾ Moreover, due to various advantages as described in previous section, InGaN material system has been predicted as one of the promising candidates for solar cell application. Initially, InGaN-based solar cells were demonstrated using Ga-rich material system because p-type doping for InN and In-rich InGaN has not yet been established,¹⁵⁾ and clear photovoltaic response was reported in 2007.^{17, 22, 23)} Since then, a lot of efforts have been conducted to develop high-efficiency solar cells from different viewpoints. Particularly, diverse solar cell structures has been investigated including $\text{In}_x\text{Ga}_{1-x}\text{N}$ p-i-n and p-n homojunction cells,^{22,-27)} $\text{In}_x\text{Ga}_{1-x}\text{N}/\text{GaN}$ p-i-n heterojunction cells,^{17,28-31)} $\text{In}_x\text{Ga}_{1-x}\text{N}/\text{Si}$ heterojunction cells,³²⁾ $\text{In}_x\text{Ga}_{1-x}\text{N}$ quantum well structures,³³⁻³⁶⁾ $\text{In}_x\text{Ga}_{1-x}\text{N}$ quantum dot structure.³⁷⁾ However, despite of these significant efforts, their conversion efficiencies and device performances are still poor mainly due to high band gap energy of InGaN layer caused by low In-content and also poor crystal quality of InGaN-based structures. Following section addresses important challenges for InGaN-based solar cells.

1.3.3 Challenges for InGaN-based solar cells

The main challenges related to InGaN-based solar cells can be divided into four categories: 1) strong polarization effect, 2) high defect density, 3) severe In-fluctuation effect, and 4) difficulty in p-type doping and contact. These challenges are discussed in detail in this section.

1) Strong polarization effect

The conventional growth direction of III-N is along the (0001) plane of the hexagonal

wurtzite structure. Due to the non-vanishing piezoelectric tensors and inversion asymmetry of the structure in the conventional c-direction, III-N heterostructures exhibit large spontaneous and piezoelectric polarization, inducing the formation of significant interface charges.³⁸⁻⁴¹⁾ For light-emitting diodes, the internal electric field induced by the interface charges is known to decrease the recombination efficiency by separating the electron and hole wave functions in the active layer region (Fig. 1.8), resulting in the degradation of device performance.⁴²⁾ Similarly, the internal electric field induced by piezoelectric polarization (i.e., piezoelectric fields) has also been reported to degrade solar cell performance because the piezoelectric fields at the GaN/InGaN heterointerfaces create drift currents in the direction opposite of that needed for efficient carrier collection.

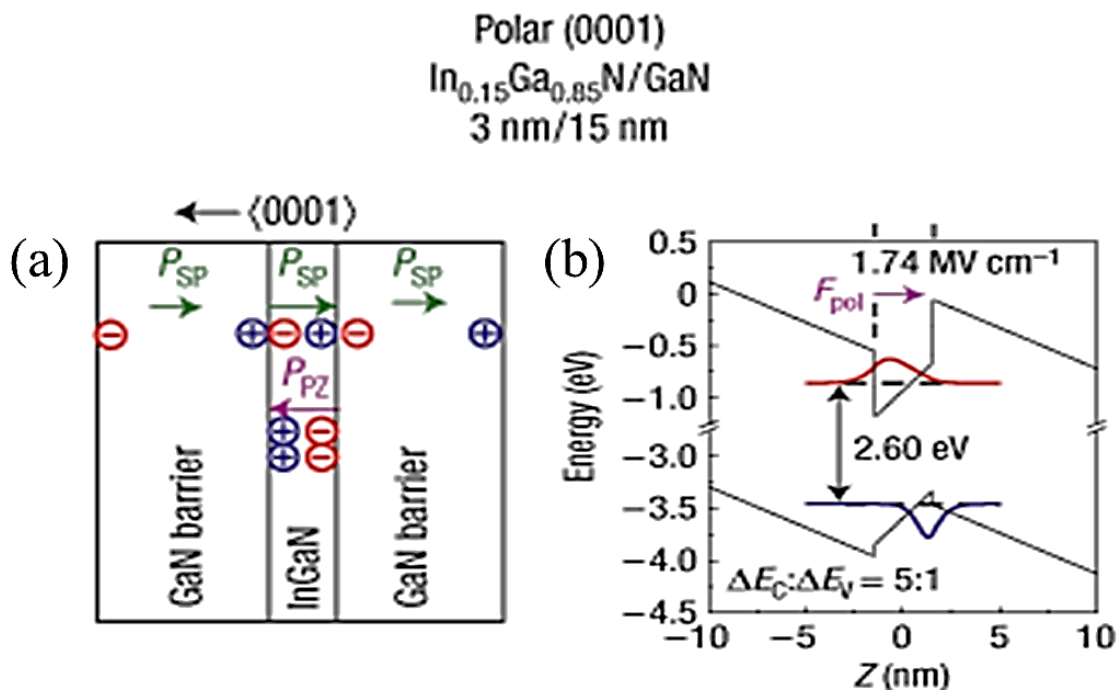


Figure 1.8 Schematic images of (a) polarization and (b) energy band profiles for strained $\text{In}_{0.15}\text{Ga}_{0.85}\text{N}/\text{GaN}$ quantum wells⁴³⁾

2) High defect density

Sapphire substrates are commonly used for the growth of wurtzite III-N due to the lack of a suitable substrate for lattice-matched epitaxy. However, an epitaxial film grown on sapphire substrates gives rise to high dislocation density because of the large lattice mismatch (-14% for GaN on sapphire and +29% for InN on sapphire) between III-N and the sapphire substrate. Additionally, thermal strain occurs during the cooling process due to the difference in thermal expansion coefficient between the epitaxial layer and the substrate; this large thermal stress produces threading dislocations in the epitaxial layer. For these reasons, GaN templates are generally applied to III-N epitaxial growth to remedy the high dislocation density; however, lattice mismatch between the $\text{In}_x\text{Ga}_{1-x}\text{N}$ epitaxial layer and GaN template is also increased by increasing the content of In. Therefore, when the thickness of the InGaN layer becomes much greater than the critical thickness, the number of misfit dislocations increases rapidly. These dislocations act as non-radiative recombination centers and may decrease the carrier lifetime; thus, dislocations are thought to be detrimental to solar cell performance as they limit short-current density.⁴⁴⁾

3) Severe In-fluctuation effect

The growth of high-quality InGaN with In-contents exceeding 20% is essential to develop highly efficient solar cells. However, when the thickness and In-content (x) of the $\text{In}_x\text{Ga}_{1-x}\text{N}$ layer are increased, In-rich clusters form easily in the $\text{In}_x\text{Ga}_{1-x}\text{N}$ layer, mainly due to the low miscibility of InN in GaN.⁴⁵⁾ In particular, In-fluctuation in the $\text{In}_x\text{Ga}_{1-x}\text{N}$ layer tends to be severe when $x > 0.15$.⁴⁶⁾ Although light absorption can be improved by In-fluctuation, which may act as an intermediate band or quantum dot,³⁷⁾ In-fluctuation also may act as recombination centers, resulting in a decrease in short-current density. Moreover, high In-content and fluctuation in InGaN/GaN multi-quantum well solar cells have been shown to

result in degraded fill factor and conversion efficiency.⁴⁷⁾ Due to these double-sided characteristics, In-fluctuation in the $\text{In}_x\text{Ga}_{1-x}\text{N}$ layer should be further studied to obtain highly efficient solar cells.

4) Difficulty in p-type doping

The p-type conduction is indispensable to realize optoelectronic devices including solar cells. However, obtaining p-type conductivity in InGaN alloys is difficult, partly because of the high background electron concentration ($\sim 10^{17} \text{ cm}^{-3}$), which is believed to originate from native defects such as oxygen and hydrogen impurities or nitrogen vacancies.⁴⁸⁻⁴⁹⁾ Additionally, relatively deep acceptor levels of the acceptor Mg in GaN ranging from 160 to 200 meV, causing a low activation efficiency, lead to low hole concentrations in Mg-doped III-N alloys at room temperature.⁵⁰⁻⁵³⁾ Therefore, these challenges need to be overcome in InGaN-based solar cells to take full advantage of their potential.

1.4 Research objectives and synopsis

Although various efforts have been extensively carried out to develop high-efficiency InGaN-based solar cells, device performances and efficiencies are still poor. Especially, as research of InGaN-based solar cells is still in its early stages, a lack of information for photovoltaic characteristics is one of the critical parts of the problems. Therefore, it is highly desirable to understand the effects that cause degradation of device performance in InGaN-based solar cells to overcome the challenges effectively. Among the main challenges as mentioned previously, the most of them occur when In-content is increased to grow thick-high quality InGaN materials having long wavelength. Thus, effects of polarization, defect density, and In-fluctuation which are closely associated with the In-content were numerically

and experimentally investigated in this study. Additionally, to clearly determine the photovoltaic behaviors, a single-junction solar cell structure was only considered in this study.

This thesis is composed of six chapters (Fig. 1.9). As already mentioned, Chapter 1 describes the basic information of solar energy and introduces InGaN-based solar cells. Chapter 2 introduces experimental approaches implemented in this study and typical solar cell parameters ranging from open circuit voltage to conversion efficiency. In Chapter 3, the effect of piezoelectric fields on carrier dynamics is numerically investigated to interpret photovoltaic characteristics in InGaN-based solar cells. To confirm the effect of piezoelectric fields experimentally, Chapter 4 handles the InGaN-based solar cell grown on semipolar (11-22) plane which can reduce the piezoelectric, and the photovoltaic properties of semipolar (11-22) InGaN-based solar cells are compared to those of c-plane InGaN-based solar cells. Chapter 5 discusses the InGaN-based solar cells that dislocation density was controlled by using the SiN_x insertion layer in order to understand the effects of dislocations on device performance independently. Finally, Chapter 6 summarizes this thesis and suggests future research directions.

Growth and Characterization of InGaN-Based Solar Cells

Objectives : build extensive knowledge to find the possibility and breakthrough of developing high-efficient solar cells

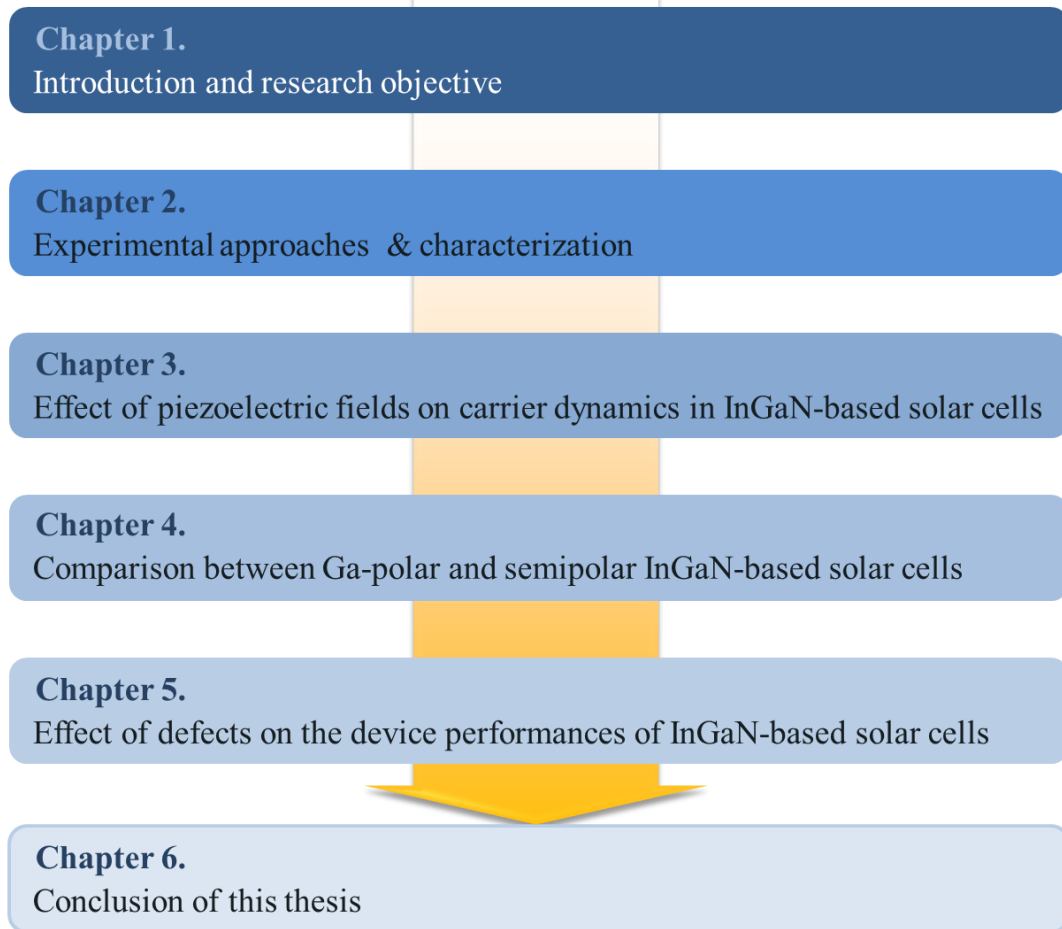


Figure 1.9 Organization of this thesis

1.5 References

- 1) BP p.l.c, BP Statistical Review of world Energy, London, United Kingdom, 2014.
- 2) O. Ellabban, H. Abu-Rub, F. Blaabjerg, Renewable and Sustainable Energy Reviews 39, 748 (2014).
- 3) <http://www.appliedscience.org.uk/contents/?article=6>
- 4) R. Perez, M. Perez, The IEA SHC Solar Update 50, 2 (2009).
- 5) <http://www.bine.info/en/newsoverview/news/vierfach-solarzelle-erreicht-rekord-wirkungsgrad/>
- 6) M. A. Green, K. Emery, Y. Hishikawa, W. Warta, E. D. Dunlop, Prog. Photovolt: Res. Appl. **22**, 1 (2014).
- 7) E. F. Schubert, Light Emitting Diodes, Cambridge University Press, New York, 2006.
- 8) S. Nakamura, G. Fasol, The Blue Laser Diode: The Complete Story, Springer, Berlin, 2000.
- 9) S. W. Feng, L. W. Tu, J. I. Chyi, H. C. Wang, Thin Solid Films **517**, 909 (2008).
- 10) A. G. Bhuiyan, A. Hashimoto, A. Yamamoto, J. Appl. Phys. **94**, 2779 (2003).
- 11) J. Wua, J. Appl. Phys. **106**, 011101 (2009).
- 12) J. Wu, W. Walukiewicz, K. M. Yu, W. Shan, J. W. Ager III, E. E. Haller, Hai Lu, W. J. Schaff, W. K. Metzger, and S. Kurtz, J. Appl. Phys. **94**, 6477 (2003).
- 13) W. Shockley, H. Queisser, J. Appl. Phys. **32**, 510 (1961).
- 14) C. Honsberg, O. Jani, A. Doolittle, E. Trybus, G. Namkoong, I. Ferguson, D. Nicol, and A. Payne, "InGaN – A New Solar Cell Material," Proceedings of the 19th European Photovoltaic

Science and Engineering Conference, Paris, France, June 7-11, 2004, p. 15-20.

15) A. Yamamoto, Md. R. Islam, T.-T. Kang, and A. Hashimoto, *Phys. Stat. Sol. (c)* **7**, 1309 (2010).

16) Y. Nanishi, Y. Saito, and T. Yamaguchi, *Jpn. J. Appl. Phys.* **42**, 2549 (2003).

17) O. Jani, I. Ferguson, C. Honsberg, S. Kurtz, *Appl. Phys. Lett.* **91**, 132117 (2007).

18) A. G. Bhuiyan, K. Sugita, A. Hashimoto, A. Yamamoto, *IEEE J. Photovolt.* **2**, 276 (2012).

19) J. F. Muth, J. H. Lee, I. K. Shmagin, R. M. Kolbas, J. Casey, B. P. Keller, U. K. Mishra, S. P. DenBaars, *Appl. Phys. Lett.* **71**, 2572 (1997).

20) R. Singh, D. Doppalapudi, T. D. Moustakas, L. T. Romano, *Appl. Phys. Lett.* **70**, 1089 (1997).

21) J. F. Muth, J. D. Brown, M. A. L. Johnson, Z. Yu, R. M. Kolbas, J. W. Cook, Jr., J. F. Schetzina, *MRS Internet J. Nitride Semicond. Res.* **4S1**, G5.2 (1999).

22) O. Jani, H. Yu, E. Trybus, B. Jampana, I. Ferguson, A. Doolittle, C. Honsberg, the 22nd Eur. Photovoltaic Solar Energy Conf., Milan, Italy, Sep. 3–7, 2007.

23) C. Yang, X. Wang, H. Xiao, J. Ran, C. Wang, G. Hu, X. Wang, X. Zhang, J. Li, J. Li, *Phys. Stat. Sol. (a)* **204**, 4288 (2007).

24) X. Chen, K. D. Matthews, D. Hao, W. J. Schaff, L. F. Eastman, *Phys. Stat. Sol. (a)* **205**, 1103 (2008).

25) X.-M. Cai, S.-W. Zeng, B.-P. Zhang, *Appl. Phys. Lett.* **95**, 173504 (2009).

26) B. R. Jampana, A. G. Melton, M. Jamil, N. N. Faleev, R. L. Opila, I. T. Ferguson, C. B.

Honsberg, IEEE Electron Device Lett. **31**, 32 (2010).

27) C. Boney, I. Hernandez, R. Pillai, D. Starikov, A. Bensaoula, M. Henini, M. Syperek, J. Misiewicz, R. Kudrawiec, Phys. Stat. Sol. (c) **8**, 2466 (2011).

28) X. Zheng, R.-H. Horng, D.-S. Wu, M.-T. Chu, W.-Y. Liao, M.-H. Wu, R.-M. Lin, Y.-C. Lu, Appl. Phys. Lett. **93**, 261108 (2008).

29) C.-L. Tsai, G.-S. Liua, G.-C. Fana, Y.-S. Leea, Solid-State Electron. **54**, 541 (2010).

30) Y. Kuwahara, T. Fujii, Y. Fujiyama, T. Sugiyama, M. Iwaya, T. Takeuchi, S. Kamiyama, I. Akasaki, and H. Amano, Appl. Phys. Express **3**, 111001 (2010).

31) E. Matioli, C. Neufeld, M. Iza, S. C. Cruz, A. A. Al-Heji, Xu Chen, R. M. Farrell, S. Keller, S. DenBaars, U. Mishra, S. Nakamura, J. Speck, C. Weisbuch, Appl. Phys. Lett. **98**, 021102 (2011).

32) L. A. Reichertz, I. Gherasoiu, K. M. Yu, V. M. Kao, W. Walukiewicz, J. W. Ager, Appl. Phys. Express **2**, 122202 (2009).

33) R. Dahal, B. Pantha, J. Li, Y.J. Lin, H. X. Jiang, Appl. Phys. Lett. **94**, 063505 (2009).

34) R. Dahal, J. Li, K. Aryal, J.Y. Lin, H. X. Jiang, Appl. Phys. Lett. **97**, 073115 (2010).

35) I. M. Pryce, D. D. Koleske, A. J. Fischer, H. A. Atwater, Appl. Phys. Lett. **96**, 153 (2010).

36) M. J. Jeng, Y. L. Lee, L. B. Chang, J. Phys. D Appl. Phys. **42**, 105101 (2009).

37) Y.-J. Lee, M.-H. Lee, C.-M. Cheng, C.-H. Yang, Appl. Phys. Lett. **98**, 263504 (2011).

38) F. Bernardini, V. Fiorentini, D. Vanderbilt, Phys. Rev. B **56**, R10024 (1997).

39) O. Ambacher, J. Smart, J. R. Shealy, N. G. Weimann, K. Chu, M. Murphy, W. J. Schaff, L.

- F. Eastman, R. Dimitrov, L. Wittmer, M. Stutzmann, W. Rieger, J. Hilsenbeck, *J. Appl. Phys.* **85**, 3222 (1999).
- 40) O. Ambacher, B. Foutz, J. Smart, J. R. Shealy, N. G. Weimann, K. Chu, M. Murphy, A. J. Sierakowski, W. J. Schaff, L. F. Eastman, R. Dimitrov, A. Mitchell, M. Stutzmann, *J. Appl. Phys.* **87**, 334 (2000).
- 41) V. Fiorentini, F. Bernardini, O. Ambacher, *Appl. Phys. Lett.* **80**, 1204 (2002).
- 42) V. Fiorentini, F. Bernardini, F. Della Sala, A. Di Carlo, P. Lugli, *Phys. Rev. B* **60**, 8849 (1999).
- 43) S. F. Chichibu, A. Uedono, T. Onuma, B. A. Haskell, A. Chakraborty, T. Koyama, P. T. Fini, S. Keller, S. P. Denbaars, J. S. Speck, U. K. Mishra, S. Nakamura, S. Yamaguchi, S. Kamiyama, H. Amano, I. Akasaki, J. Han, T. Sota, *Nature materials* **5**, 810 (2006).
- 44) J. J. Wierer, Jr., A. J. Fischer, D. D. Koleske, *Appl. Phys. Lett.* **96**, 051107 (2010).
- 45) I. Ho, G. B. Stringfellow, *Appl. Phys. Lett.* **69**, 2701 (1996).
- 46) Y.-S. Lin, K.-J. Ma, C. Hsu, S.-W. Feng, Y.-C. Cheng, C.-C. Liao, C. C. Yang, C.-C. Chou, C.-M. Lee, J.-I. Chyi, *Appl. Phys. Lett.* **77**, 2988 (2000).
- 47) K. Y. Lai, G. J. Lin, Y.-L. Lai, Y. F. Chen, J. H. He, *Appl. Phys. Lett.* **96**, 081103 (2010).
- 48) H. P. Maruska, J. J. Tietjen, *Appl. Phys. Lett.* **15**, 327 (1969).
- 49) P. Perlin, T. Suski, H. Teisseyre, M. Leszczynski, I. Grzegory, J. Jun, S. Porowski, P. Bogusławski, J. Bernholc, J. C. Chervin, A. Polian, T. D. Moustakas, *Phys. Rev. Lett.* **75**, 296 (1995).
- 50) T. Tanaka, A. Watanabe, H. Amano, Y. Kobayashi, I. Akasaki, *Appl. Phys. Lett.* **65**, 593

(1994).

51) W. Götz, N. M. Jonson, J. Walker, D. P. Bour, R. A. Street, Appl. Phys. Lett. **68**, 667

(1996).

52) W. Kim, A. Salvador, A. E. Botchkarev, O. Aktas, S. N. Mahammad, H. Morkoç, Appl.

Phys. Lett. **69**, 559 (1996).

53) W. Kim, A. E. Botchkarev, A. Salvador, G. Popovici, H. Tang, H. Morkoç, Appl. Phys.

Lett. **82**, 219 (1997).

Chapter 2

Experimental approaches & characterization

2.1 Illumination source

2.1.1 Solar radiation

Since a solar cell converts solar radiation into electricity, the device performance significantly depends on solar radiation conditions. However, solar irradiation (i.e., the solar spectrum) reaching the surface of the Earth changes considerably with location, atmospheric conditions (e.g., cloud cover and ozone layer conditions), and the distance between the sun and Earth. Thus, the defined standard solar spectra are needed to compare the performances of solar cells from the different research laboratories and manufacturers. Detailed information on the various standard solar spectra is given in Table 2.1, and schematic images of corresponded conditions are indicated in Fig. 2.1.

Table 2.1 Different specifications of standard solar radiations

Solar condition	Standard	Power density (Wm^{-2})	Conditions
AM 0	ASTM E 490	1,353	Just outside the Earth's atmosphere (for space application)
AM 1	CIE Publication, Table 2	1,000	Sun overhead, sea level, horizontal surface
AM 1.5 D	ASTM G 173-03	768.3	Tilted surface at 37°, zenith 48°, facing due south, albedo 0.3, turbidity 0.29, 20°C ambient temperature *D: Direct radiation *G: Global radiation
AM 1.5 G		963.8	
AM 1.5 G	CEI/IEC 904-3	1,000	

* ASTM: American Society for Testing and Materials

*CIE: Committee Internationale d'Eclairage

*CEI(commission Electrotechnique interationale)/ IEC(International Electrotechnical Commission)

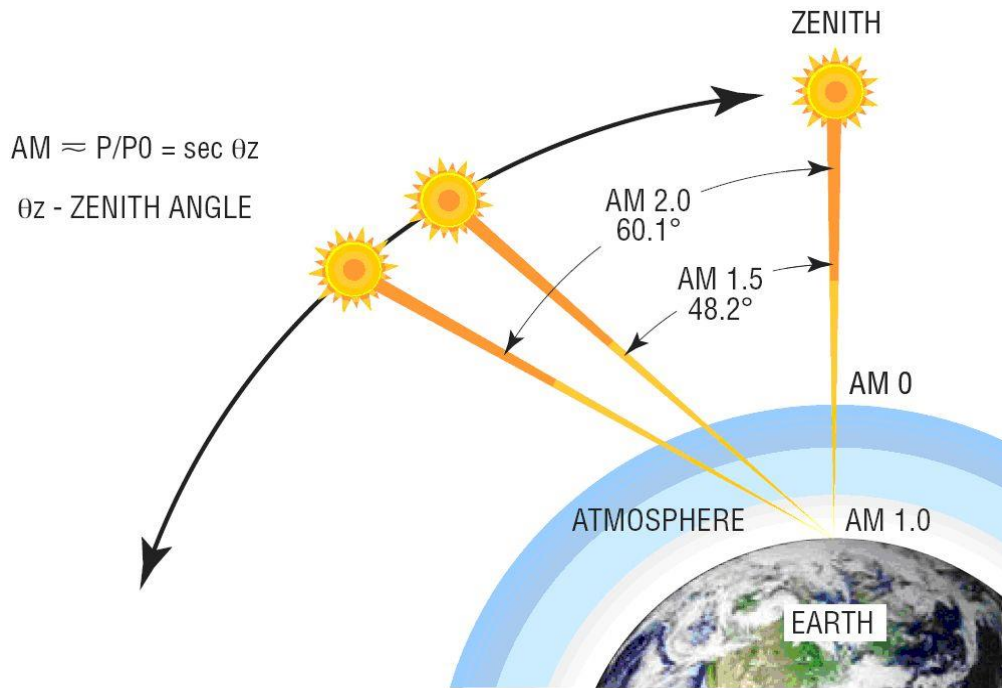


Figure 2.1 The path length (in units of air mass) changes with the zenith angle¹⁾

Among these standard solar spectra, the most widely used are AM (air mass) 0, 1.5D, and 1.5G. The corresponding reference solar spectral irradiances, ASTM G-173-03, are plotted in Fig. 2.2.

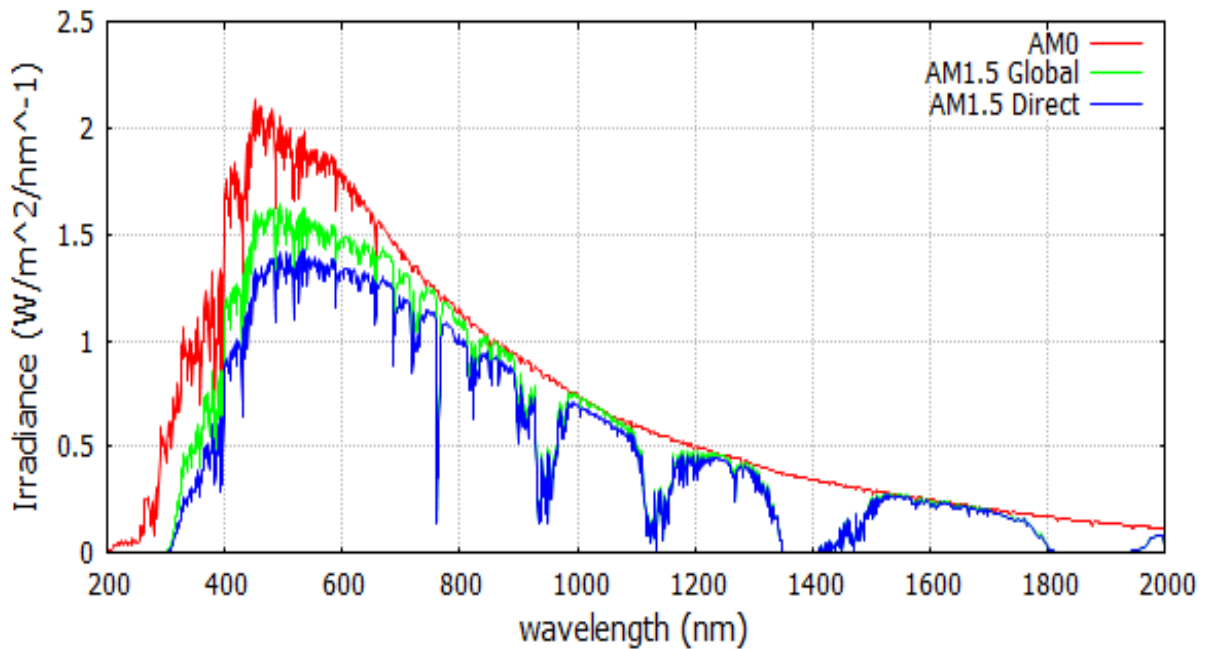


Figure 2.2 Standard solar spectra for space and terrestrial use (AM 0, AM 1.5G, AM 1.5D)²⁾

The AM 0 condition is used for space applications, and AM 1.5D and 1.5G conditions are used for terrestrial applications. Since the AM 1.5D spectrum is defined for solar concentrator work, whereas the AM 1.5G spectrum is defined for flat plate modules, the AM 1.5G condition was applied in this study.

2.1.2 Solar simulator

Since solar radiation can vary with daily atmospheric conditions, a stable light source that closely matches the conditions (e.g., intensity and spectrum) of standard solar radiation is required to evaluate the solar cell performance. Thus, an artificial light source that simulates solar radiation is commonly used to evaluate the solar cell. An ideal illumination source satisfies the following criteria:³⁾

- 1) A spatial non-uniformity of less than 1%
- 2) A variation in total irradiance with time of less than 1%
- 3) Filtered for a given reference spectrum to have a spectral mismatch error of less than 1%
- 4) These requirements are essential in obtaining an accuracy of better than 2%

For these reasons, a xenon lamp solar simulator (HAL-320/Asahi spectra Co., Ltd.) with spectral match <1.25%, irradiance inhomogeneity <2%, and temporal instability <2% in the short term was used in this study. An AM filter was also installed to approximate the AM 1.5G spectrum. The difference between the spectral irradiance of the AM 1.5G reference solar radiation spectrum and the solar simulator is shown in Fig. 2.3.

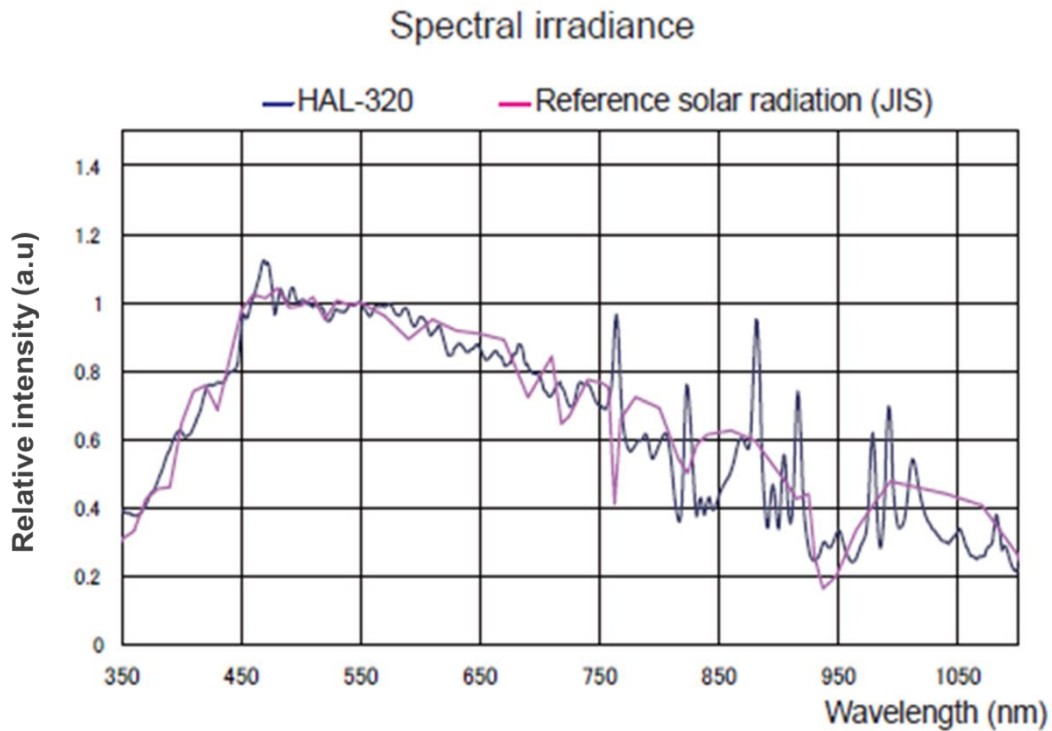


Figure 2.3 Comparison of spectral irradiance of the standard AM 1.5G spectrum and solar simulator⁴⁾

2.2 Solar cell parameters

In general, solar cell performance can be quantified by four parameters: 1) short-current density, 2) open-circuit voltage, 3) fill factor, and 4) conversion efficiency.

1) Short-current density (J_{sc} , A/cm^2). The short-circuit current, I_{sc} (A), which is the maximum current from a solar cell, can be measured when the voltage across the solar cell is zero (see Fig. 2.4). However, short-current density is more commonly referenced rather than the short-circuit current to eliminate the dependence on the solar cell area. Short-current density is affected by several factors including diffusion length, surface passivation, and generation rate.

2) Open-circuit voltage (V_{oc} , V). The maximum voltage from a solar cell is defined as the open-circuit voltage occurring when the net current through the device is zero. The open-circuit voltage typically depends on the short-current density and the bandgap energy of the

material. While the short-current density decreases with increasing bandgap, the open-circuit voltage increases.

3) Fill factor (FF, %). FF is an important parameter to evaluate the quality of the solar cell and is determined as the ratio of the maximum power (P_{MP}) from the solar cell to the product of open-circuit voltage and short-current density. Therefore, the fill factor can be expressed as the area of the largest rectangle that will fit in the I–V curve, as indicated in Fig. 2.4 (where V_{MP} and I_{MP} are the voltage and current at the maximum power point). In this regard, two major factors that affect the fill factor are the characteristic resistance defined as the output resistance of the solar cell at its maximum power point and parasitic resistances (i.e., series resistance and shunt resistance).

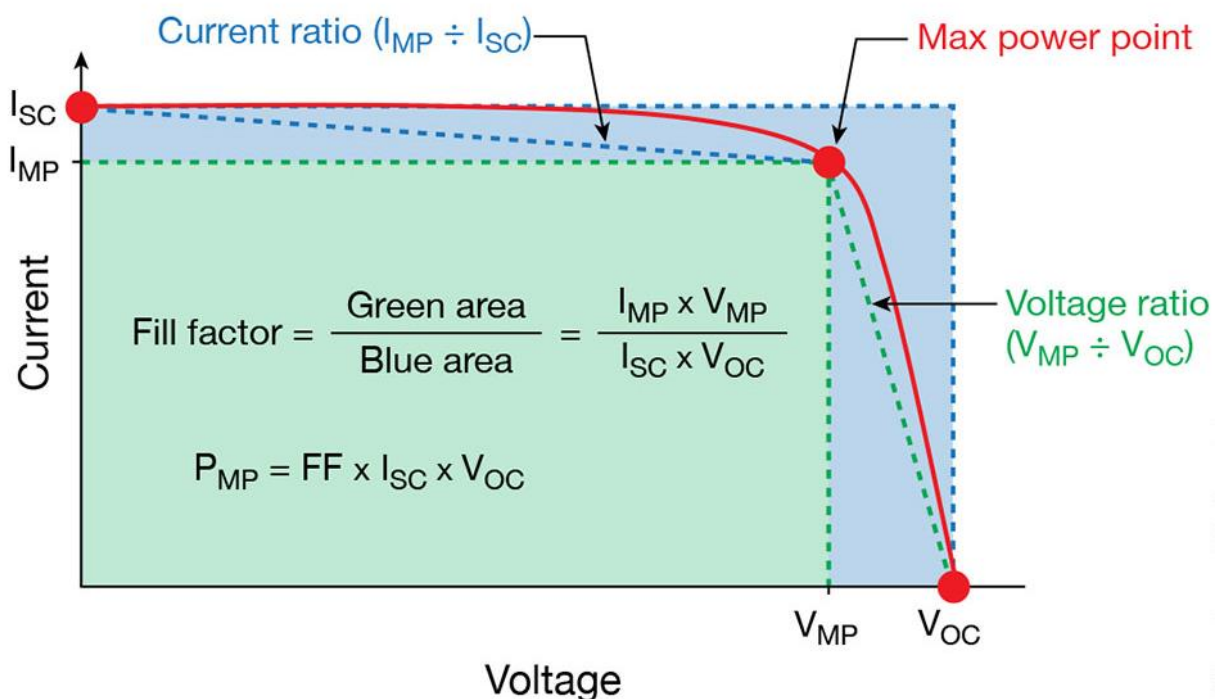


Figure 2.4 I–V curve indicating the open-circuit voltage, short-circuit current, and fill factor⁵⁾

4) Conversion efficiency (CE, %). Conversion efficiency is the most widely used parameter to compare the device performances of solar cells. Since the conversion efficiency of a solar cell is calculated by the fraction of incident power converted to electricity, the abovementioned parameters are synthetically considered to estimate the conversion efficiency. Moreover, the measurement conditions of conversion efficiency should be carefully controlled to compare the performances of two solar cells because the efficiency varies significantly with the intensity of the incident solar radiation and solar cell temperature.

2.3 References

- 1) M. Pagliaro, G. Palmisano, R. Ciriminna, Flexible Solar Cells, John Wiley & Sons, New York, 2008, p.37.
- 2) <http://rredc.nrel.gov/solar/spectra/am1.5/ASTMG173/ASTMG173.html>
- 3) K. Emery, D. Myers, S. Rummel, “Solar Simulation - Problems and Solutions,” 20th IEEE PV Specialists Conference, 1988, p. 1087.
- 4) <http://asahi-spectra.com/opticalinstrument/hal320.html>
- 5) <http://solarprofessional.com/articles/operations-maintenance/interpreting-i-v-curve-deviations/page/0/6>

Chapter 3

Effect of piezoelectric fields on carrier dynamics in InGaN-based solar cells

3.1 Background

In recent years, the InGaN material system has shown promise for high-efficiency photovoltaic (PV) systems because InGaN alloys have direct bandgaps that cover nearly the entire solar spectrum by changing the indium (In) composition.¹⁻²⁾ An earlier theoretical calculation indicated that InGaN alloys with In-contents of approximately 40% can be used as active material systems to obtain highly efficient solar cells (SCs) with conversion efficiency (CE) greater than 50%.³⁾ Additionally, various PV characteristics such as high carrier mobility, high radiation resistance, and high absorption coefficient make this material system an attractive candidate for SC applications.⁴⁻⁵⁾ Based on these merits, one of the key requirements to realize a highly efficient SC is to grow a thick, high-quality InGaN layer with high In-contents. However, in InGaN-based light-emitting diodes (LEDs) with similar structures to those of SCs, several factors such as high defect density, severe In-fluctuation, and the existence of P_{pz} degrade the device performance. In particular, P_{pz} is a critical factor that hinders the growth of InGaN layers with high In-contents because P_{pz} becomes stronger in the active region as the In-content increases. Since the strong P_{pz} in general c-plane LEDs decreases the recombination efficiency by spatially separating the electron and hole wave functions in the active layer region,⁶⁾ many researchers have extensively investigated methods to suppress P_{pz} in order to improve the recombination efficiency. As for LEDs, it is first important to determine the phenomena that degrade SC device performance, in order to overcome the problem. However, for InGaN-based SCs, no report has explained the

correlation between P_{pz} and carrier dynamics in detail, even though the mechanisms of SCs and LEDs are completely different. Therefore, in this study, we numerically investigated the effects of P_{pz} on carrier dynamics in InGaN-based p-i-n SCs.

3.2 Simulation models and material parameters

The simulation software SCSim was employed to characterize the electro-optical properties of a simple p-GaN/i-In_xGa_{1-x}N/n-GaN SC structure under the AM1.5G, 1.5 sun illumination conditions. A detailed description of the simulation procedure is described in appendix section. For numerical analysis, a 2D drift-diffusion model was implemented by calculating the light absorption, carrier generation rate, electron and hole transport statistics, and electric potential derived from the Poisson equation. In particular, the total polarization induced by spontaneous and piezoelectric polarization was also considered in the numerical model and calculated using the method suggested in ref. 7. In this process, the degree of P_{pz} was controlled by modifying the content of In along with the strain relaxation constants, denoted by “ ξ ” in the simulation. The ξ value was used to determine the strained lattice constants of an arbitrary In_xGa_{1-x}N compound layer, which can be expressed by the following equations:

$$a_R = (1 - \xi) \cdot a_S + \xi \cdot a_E(z) \quad (1)$$

$$c_R = (1 - \xi) \cdot c_S + \xi \cdot c_E(z) \quad (2)$$

where a_S and c_S are the lattice constants of the underlying layer, and a_E and c_E are those of the free-standing compound layer, which vary along the z -axis (vertical to epitaxial layer) in accordance with the material composition and the Vegard law, respectively. Therefore, by increasing ξ , the piezoelectric polarization is proportionally reduced, while the spontaneous

polarization remains unchanged; thus, the piezoelectric polarization can be numerically eliminated when $\xi = 0$. Other relevant binary material parameters used in this study are listed in Table 3.1.

Table 3.1 Material parameters of GaN and InN used in simulations

	GaN	InN
a (nm)	0.3188 ⁸⁾	0.3540 ⁹⁾
c (nm)	0.5186 ⁹⁾	0.5705 ⁹⁾
C₁₁ (GPa)	374 ¹⁰⁾	223 ¹⁰⁾
C₁₂ (GPa)	140 ¹¹⁾	115 ¹⁰⁾
C₁₃ (GPa)	106 ¹¹⁾	94 ⁹⁾
C₃₃ (GPa)	395 ¹²⁾	200 ⁹⁾
C₄₄ (GPa)	101 ¹⁰⁾	46 ¹³⁾
e₃₃ (C/m²)	0.65 ¹⁴⁾	0.43 ¹⁴⁾
e₃₁ (C/m²)	-0.33 ¹⁴⁾	-0.22 ¹⁴⁾
e₁₅ (C/m²)	-0.33 ¹⁴⁾	-0.22 ¹⁴⁾
P_{sp} (C/m²)	-0.029 ¹⁵⁾	-0.032 ¹⁵⁾

For reliability of this simulation study, the configuration and structural properties of p-i-n SC structure was cited from an experimental study published by Y. Kuwahara et al.¹⁶⁾ Moreover, only the SC structure grown on a c-plane, a free-standing GaN substrate with a dislocation density of $1 \times 10^7 \text{ cm}^{-2}$, was considered to focus on the effects of P_{pz} . The p-i-n structure consisted of a 2000-nm-thick Si-doped n-GaN layer with a doping density of $4.5 \times 10^{18} \text{ cm}^{-3}$, a 250-nm-thick undoped $\text{In}_{0.1}\text{Ga}_{0.9}\text{N}$ absorption layer, and a 100-nm-thick Mg-doped p-GaN layer with doping density of $3.6 \times 10^{18} \text{ cm}^{-3}$ (Fig. 3.1). The device is a rectangle with dimensions of $350 \times 350 \mu\text{m}^2$, which is similar to the shapes of conventional GaN-based LEDs.

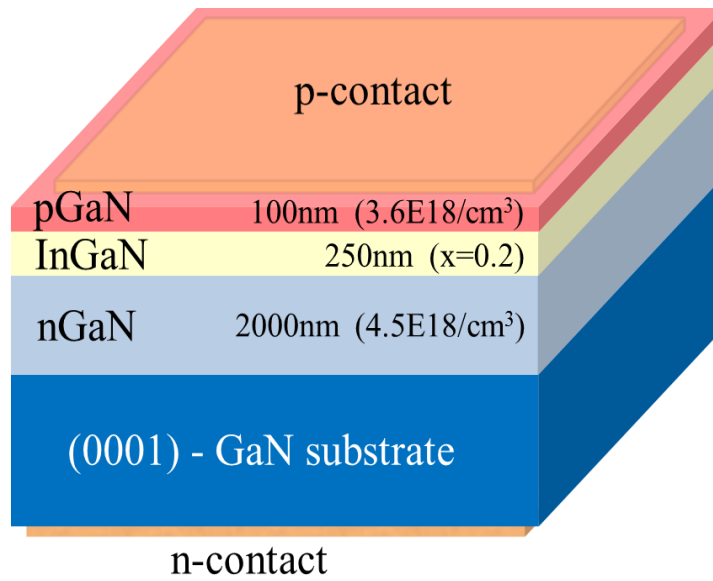


Figure 3.1 Schematic view of an InGaN SC structure

3.3 Results and discussion

3.3.1 Confirming the simulation reliability

First, the experimentally grown p-i-n InGaN SC structure mentioned above was simulated to confirm the reliability of the numerical model by comparing the experimental results with the simulated results. Figure 3.2 shows the representative experimental and theoretical device performances and I–V characteristics. As shown in the inset table in Fig. 3.2, the simulated open-circuit voltage (V_{oc}), short-current density (J_{sc}), conversion efficiency (CE), and fill factor (FF) are significantly similar to the experimental results. Furthermore, the simulated and experimental I–V curves exhibit nearly identical staircase-like shapes (slight deviation of I-V curves between experimental and simulated results is probably shown because some of the characteristics of InGaN layer, such as In-fluctuation and several types of defects, cannot be applied to simulation). These results show that our simulation model is reliable.

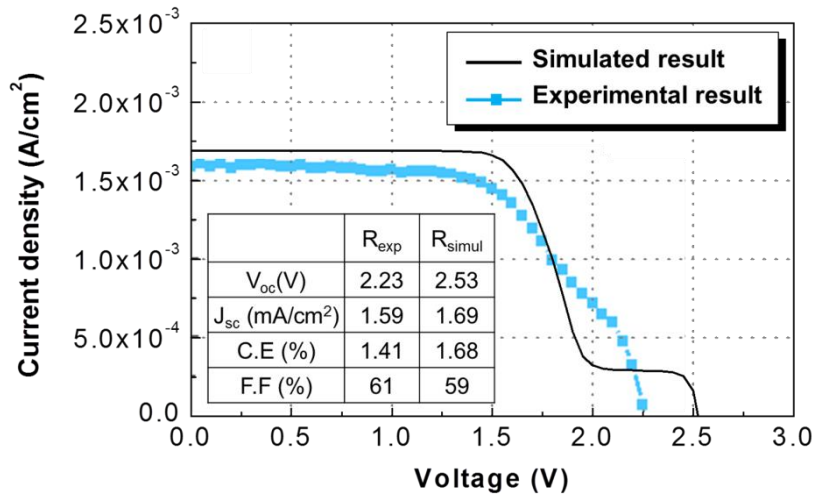


Figure 3.2 Comparison of the simulated and experimental I–V characteristics of $In_{0.1}Ga_{0.9}N$ SC structures

3.3.2 Effect of piezoelectric fields on device performance

The same p-i-n InGa_N SC structure was again simulated with a different strain relaxation constant ($\xi = 1$) to eliminate P_{pz} in the structure, allowing us to observe the effects of P_{pz} on carrier dynamics. Figure 3.3 shows the simulated I–V curves and device performances for p-i-n InGa_N SC structures with and without P_{pz} .

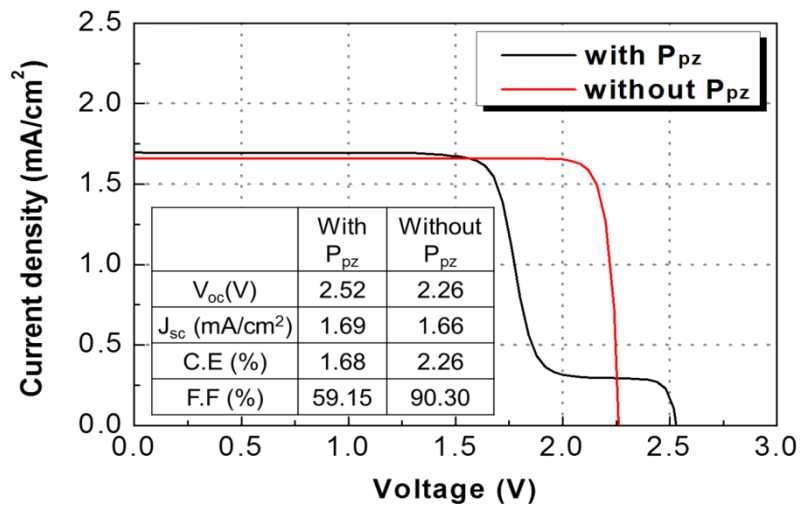


Figure 3.3 Comparison of the I–V characteristics of $In_{0.1}Ga_{0.9}N$ SC structures with and without piezoelectric fields (P_{pz})

A comparison of the two cases revealed three noticeable differences: compared to the structure without P_{pz} , the structure with P_{pz} exhibited an increased V_{oc} , slightly increased J_{sc} , and a staircase-like shape of the I–V curve. To explain these changes, the band diagram, recombination rate (radiative + non-radiative recombinations), and carrier concentration plots for the structures with and without P_{pz} were calculated under the zero-bias voltage condition (Fig. 3.4).

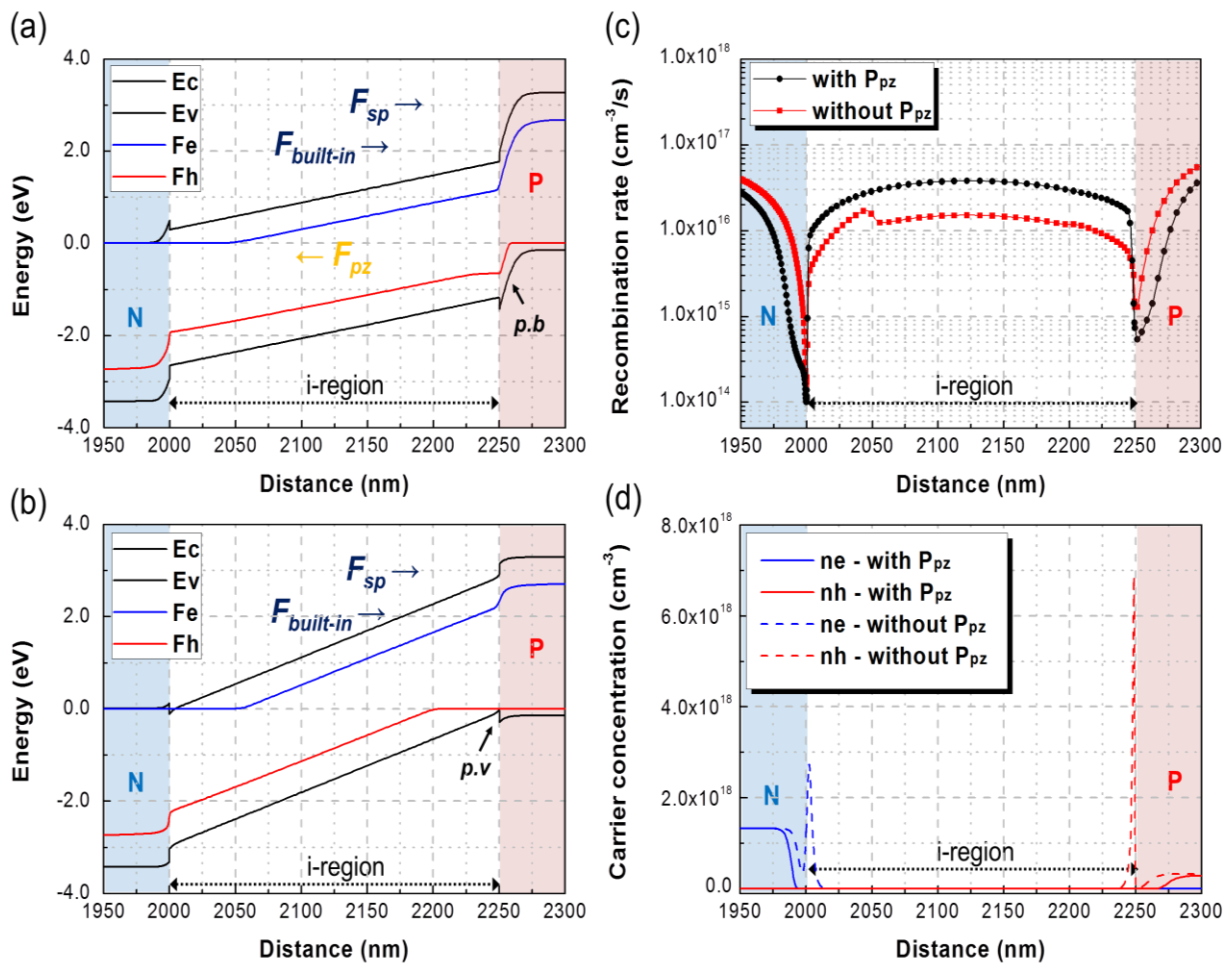


Figure 3.4 Characteristics of the $In_{0.1}Ga_{0.9}N$ SC structure with and without P_{pz} at 0 V: a–b) band diagrams under different P_{pz} conditions, c) recombination rates, and d) carrier concentration plots

3.3.3 Determination of V_{oc}

The band diagrams in Fig. 3.4 indicate that the energy band in the i-region for the structure with P_{pz} (see Fig. 3.4(a)) is reversely tilted in some degree compared to that for the structure without P_{pz} (see Fig. 3.4(b)) due to existence of P_{pz} in the direction opposite to that of the built-in fields. As a result, the inclination angle of the energy band in the i-region was fairly reduced for the structure with P_{pz} , and corresponding potential barriers were formed at each side of the InGaN/GaN interface region. These predominant potential barriers are likely associated with drift and diffusion forces and have important effects on V_{oc} because it is determined by the particular level of bias voltage at which the drift force and diffusion force become equal. As shown in Fig. 3.4(a), due to the formation of large potential barriers in the interface region, carriers affected by diffusion force may need more energy to cross the barriers, even the drift force is negligibly reduced by increasing the bias voltage. Therefore, the drift force and diffusion force in the structure with P_{pz} become the same at higher levels of bias voltage compared to the structure without P_{pz} ; thus, V_{oc} increased in the structure with P_{pz} .

3.3.4 Examination of J_{sc}

For J_{sc} , it is worthwhile to confirm the recombination rate and accumulated carrier concentration in the i-region because these factors dominantly hinder the carrier collection in the epitaxial field. The recombination rate and carrier concentration under zero-bias voltage, at which the J_{sc} value is decided, are plotted in Figs. 3.4(c) and (d), respectively. The structure with P_{pz} exhibited a higher recombination rate in the i-region than the structure without P_{pz} (maximum recombination rates in the i-region for the structure with and without P_{pz} were 3.79×10^{16} and 1.71×10^{16} cm^{-3}/s , respectively). This can be attributed to the

reduced angle of the energy band in the i-region for the structure with P_{pz} (see Fig. 3.4(a)), which promotes the recombination of photogenerated carriers in this region by suppressing the drift force. However, the obtained spatial carrier distributions imply a contrary behavior. Figure 3.4(b) shows that the heights of the potential barriers were significantly decreased in the InGaN/GaN interface regions by eliminating P_{pz} , which seems like potential valleys are formed at the interface regions. Moreover, the minimum states of conduction and valence band are in contact with the electron and hole quasi static Fermi level, respectively. Because of these energy band shapes, a great number of carriers in the structure without P_{pz} are accumulated at both the n- and p-sides of the InGaN/GaN interface regions (Fig 3.4(d)), whereas the number of accumulated carriers in the same regions for the structure with P_{pz} is almost negligible in comparison; the maximum accumulated electron and hole concentrations for the structure with P_{pz} were $5.16 \times 10^8 \text{ cm}^{-3}$ and $2.26 \times 10^{11} \text{ cm}^{-3}$, while those for the structure without P_{pz} were $2.73 \times 10^{18} \text{ cm}^{-3}$ and $6.88 \times 10^{18} \text{ cm}^{-3}$, respectively. As J_{sc} is determined by the joint effects of recombination and spatial carrier distribution, the structure with P_{pz} exhibits a slightly increased J_{sc} value in comparison with the structure without P_{pz} because the accumulated carrier concentration in the i-region for the structure without P_{pz} was much larger than the recombination rate in the i-region for the structure with P_{pz} .

3.3.5 Staircase-like I–V feature

To explain the staircase-like feature in the I–V curves, Figs. 3.5(a) and 3.5(b) show the I–V characteristics and recombination rate plots in the i-region for the structure with P_{pz} , respectively.

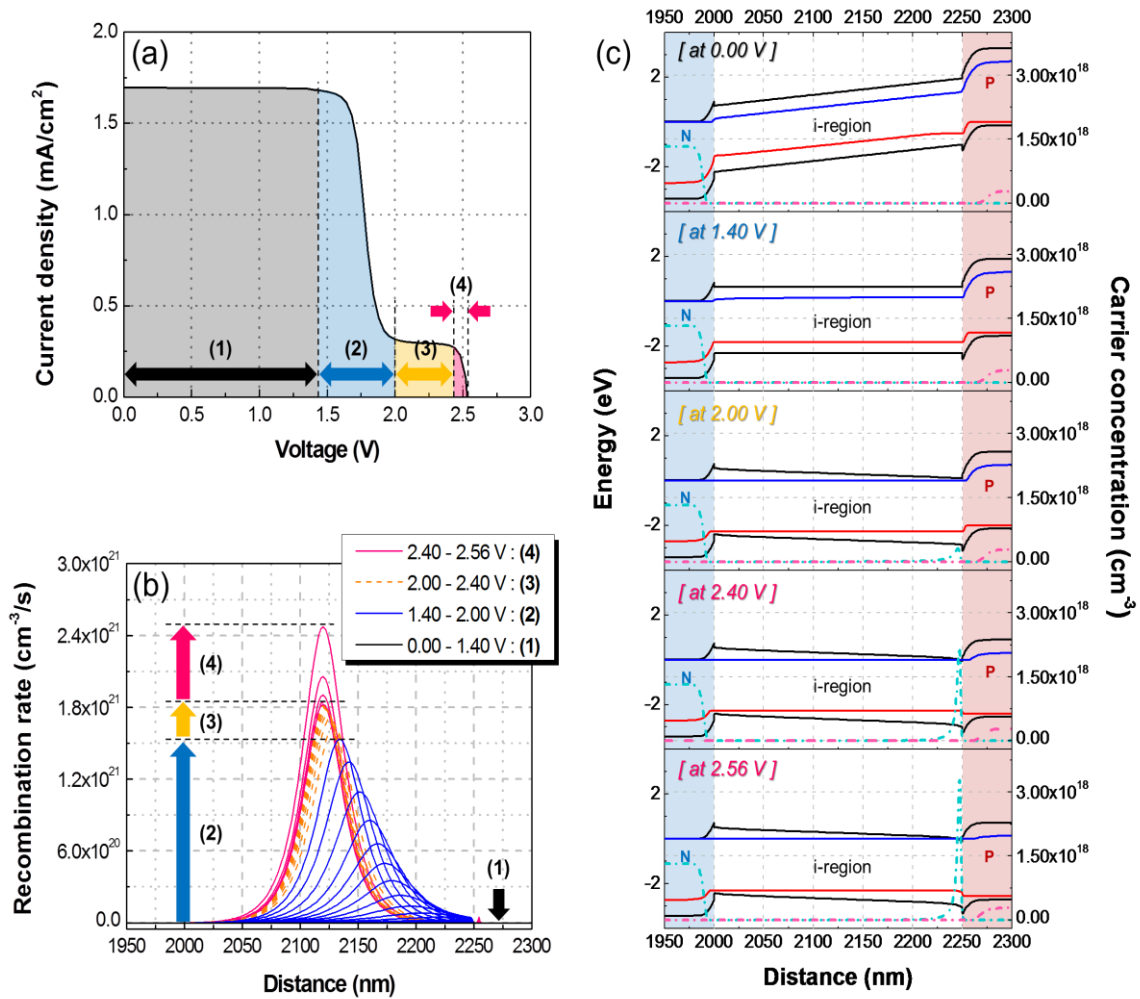


Figure 3.5 a) I–V curves and b) recombination rates for the $\text{In}_{0.1}\text{Ga}_{0.9}\text{N}$ SC structure with P_{pz} for different applied bias voltages of 0–1.40 V (1), 1.4–2.0 V (2), 2.0–2.40 V (3), and 2.40–2.56 V (4) and the corresponding band diagrams with c) carrier concentrations at specific applied bias voltages (solid and dotted lines indicate energy band and carrier concentration, respectively)

By comparing these two figures, we can find some correlation in the case of 0–1.4 V range (labeled as (1) in Fig. 3.5) and 2.0–2.4 V range (labeled as (3) in Fig. 3.5) at which current density shows almost the constant in the I–V curve, the recombination rate in i-region is rarely increased while the recombination rate in i-region is increased rapidly at 1.4 – 2.0 V range (labeled as (2) in Fig. 3.5) and 2.4 – 2.54 V range (labeled as (4) in Fig. 3.5) at which the current density is significantly decreased by increasing the bias voltage. These results indicate that the variation in current density in the I–V curve is significantly related to the recombination behavior. To further understand this behavior, the corresponding band diagrams with carrier concentration plots are presented in Fig. 3.5(c). For simplicity, only representative results obtained at 0, 1.4, 2.0, 2.4, and 2.54 V are presented in Fig. 3.5(c) (the bold solid lines are the band diagrams, and the dash-dot lines are the carrier concentrations). The different results for the different bias voltage ranges can be explained as follows. (i) In the range 0–1.4 V, the p-side energy band gradually decreased with increasing bias voltage (Fig. 3.5(c)), but carriers effectively escaped from the i-region due to strong remaining drift force of the built-in fields. Therefore, the amounts of recombination and accumulated carrier concentration were negligible in this range of bias voltage, and the current density in the I–V curve was almost constant in this range. (ii) In the range 1.4–2.0 V, the energy band in the i-region was completely flattened, even though the bias voltage increased. Since the carriers could recombine more easily in the flat region, the recombination rate in the i-region rapidly increased with the bias voltage. Thus, the current density in the I–V curve abruptly decreased in this range of bias voltage. (iii) In the range 2.0–2.4 V, the current density in the I–V curve remained steady due to the suppression of the recombination rate in the i-region. The limited recombination rate was likely due to the potential valleys that formed at each of the n- and p-sides of the InGaN/GaN interface regions, particularly the p-side. These potential valleys further flattened the energy band and separated the electron and hole wave functions in the i-

region, which is also observed in conventional InGaN/GaN LEDs. As a result, carriers began to accumulate in the potential valleys rather than recombine in the i-region with increasing bias voltage, resulting in slightly reduced (almost constant) current density in the I–V curve. Such behavior is also supported by the results of Neufeld et al.,¹⁷⁾ who reported that the current constant region in the I–V curve under high bias voltage became shorter and finally disappeared with increasing doping density in the n- and p-side InGaN/GaN interface regions, suppressing carrier storage by decreasing the potential height. (iv) In the range 2.4–2.54 V, the recombination rate increased considerably because the potential valleys were filled with carriers with increasing bias voltage. Moreover, as most of the built-in field was displaced by the applied bias voltage, the diffusion force became stronger with increasing bias voltage. As a result, the current density in the I–V curve gradually decreased in this range of bias voltage and became zero at 2.54 V, the voltage at which the diffusion force became larger than the drift force. Based on this mechanism, we can confirm that the staircase-like feature is observed due to the shape of the energy band in the i-region, showing the reduced angle of the energy band with high height of the potential barrier, which is affected by P_{pz} having a direction opposite to that of the built-in fields, and this feature also denotes that current loss is arisen in the structure.

3.3.6 Photovoltaic behavior as a function of In-content

Until now, only the p-i-n $\text{In}_x\text{Ga}_{1-x}\text{N}$ structure with an In-content (x) of 0.1 was considered. However, to develop highly efficient $\text{In}_x\text{Ga}_{1-x}\text{N}$ SCs, the In-content of the $\text{In}_x\text{Ga}_{1-x}\text{N}$ layer

needs to be increased further to absorb a broad range of incident solar radiation. Thus, the SC structure was simulated again with different In-contents in the i-layer. Figure 3.6 and Table 3.2 show the I–V characteristics and device performances of the structures with different In-contents, respectively.

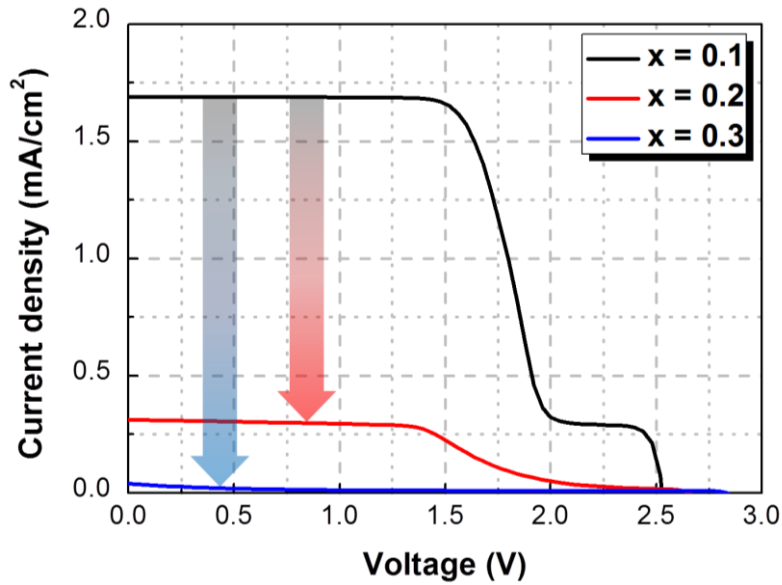


Figure 3.6 I–V characteristics of InGaN SC structures with different In-contents

Table 3.2 Simulated device performances of InGaN SC structures with different In-contents.

	In-content		
	0.1	0.2	0.3
V_{oc} (V)	2.52	2.65	2.84
J_{sc} (mA/cm²)	1.69	0.31	0.04
CE (%)	1.68	0.26	0.02
FF (%)	59.15	46.20	23.45

The results show that V_{oc} gradually increased with increasing In-content, whereas J_{sc} significantly decreased, even though the carrier generation rate (Fig. 3.7) increased by three to seven times with increasing In-content (the integrated carrier generation rates in the i-region for the structures with In-contents of 0.1, 0.2, and 0.3 were 8.58×10^{22} , 2.67×10^{23} , and $5.67 \times 10^{23} \text{ cm}^{-3}\cdot\text{s}$, respectively).

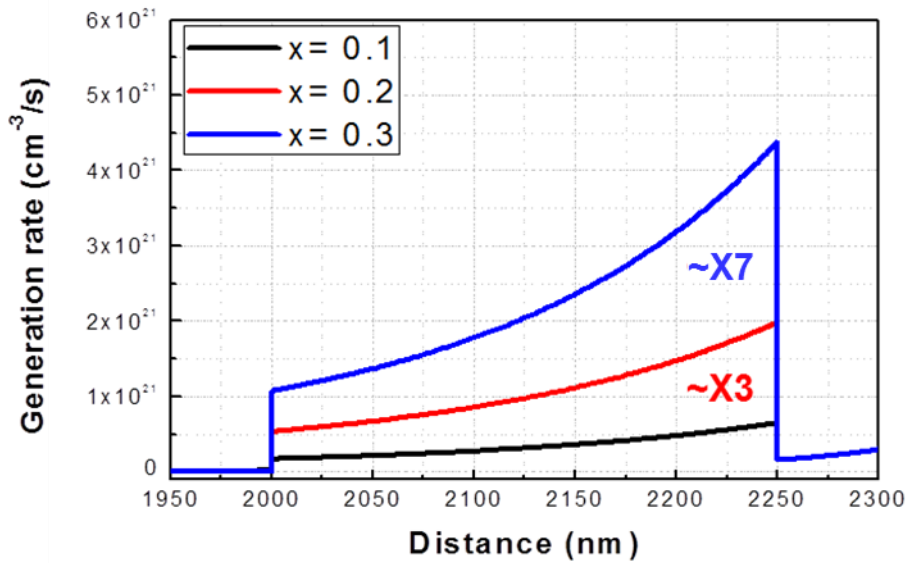


Figure 3.7 Generation rates of InGaN SC structures with different In-contents

These results can be explained by Fig. 3.8, which shows the band diagrams, recombination rates, and carrier concentration plots for the structures with different In-contents at zero-bias voltage. As shown in Fig. 3.8(a), the height of the potential barrier at both interface regions increased as the P_{pz} in the i-region became stronger due to increasing In-content; as discussed above, these increased potential barrier heights increased the V_{oc} . In contrast, J_{sc} decreased dramatically with increasing In-content because the recombination rate in the i-region (Fig. 3.5(b)) significantly increased from 3.79×10^{16} to $9.72 \times 10^{21} \text{ cm}^{-3}\cdot\text{s}^{-1}$ as the In-contents increased from 0.1 to 0.3. As expected, this trend in recombination is somewhat associated

with the shape of the energy band in the i-region. Since the energy bands in the i-region at In-contents of 0.2 and 0.3 were already tilted reversely, even at zero-bias voltage, in contrast to the In-content = 0.1 case, the recombination was promoted over carrier escape. Furthermore, Fig. 3.5(c) shows that carriers were significantly accumulated in both sides of the interface region with increasing In-content because the potential valleys deepened due to the increasing P_{pz} in the direction opposite to that of the built-in fields. Based on these results, the values of CE and FF decreased with increasing In-content, resulting in high current loss.

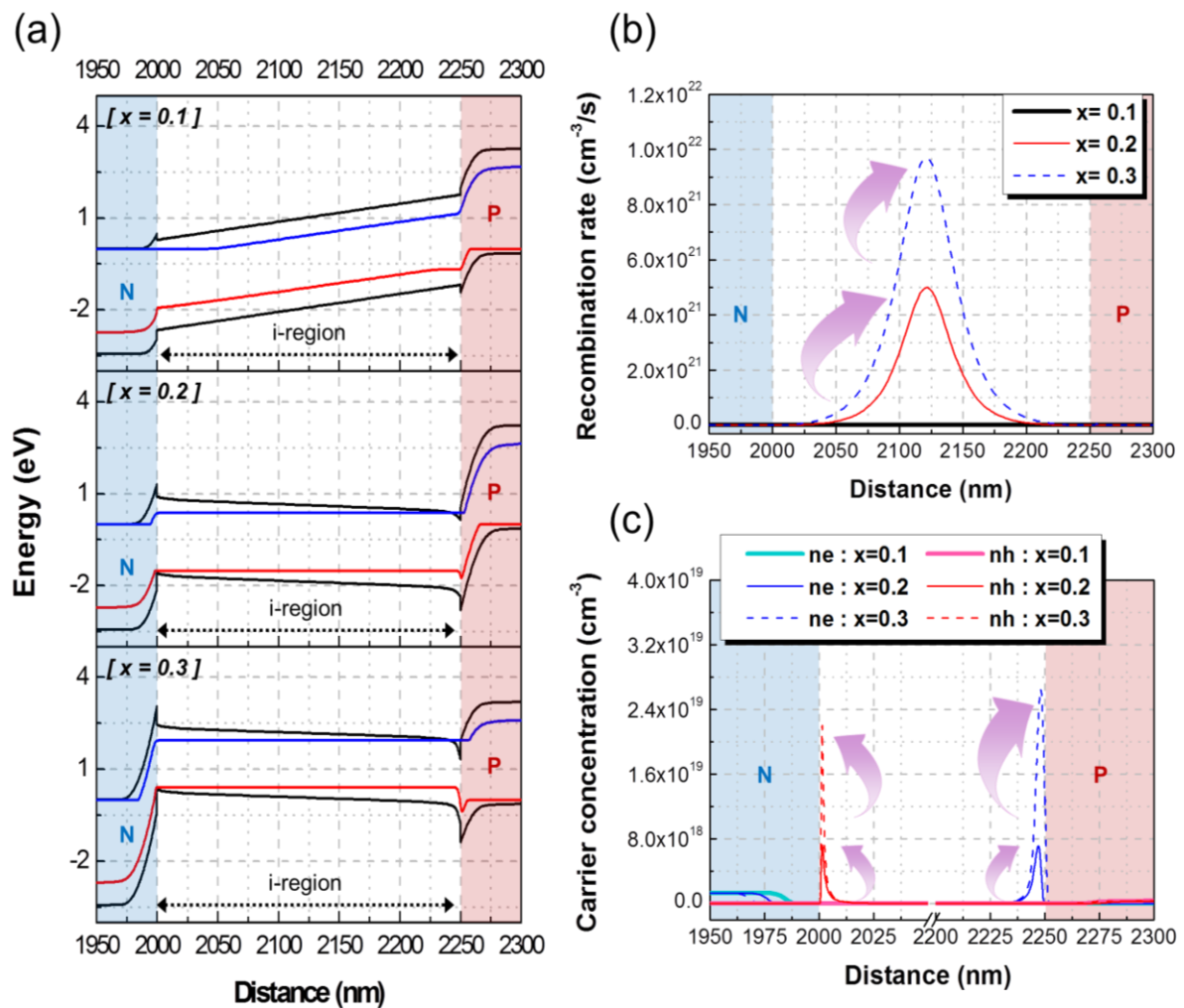


Figure 3.8 a) Band diagrams, b) recombination rates, and c) carrier concentration plots for the InGaN SC structures with different In-contents at zero-bias voltage

3.3.7 Various methods to control P_{pz}

Generally, for LED applications, various methods such as high doping (n- and p-type Doping concentrations were 4.5×10^{19} and $3.6 \times 10^{19} \text{ cm}^{-3}$, respectively), growth of N-polar (000-1) planes, growth of nonpolar plane, and growth of semipolar plane are used to eliminate the harmful effects of P_{pz} . Thus, we applied these methods to our simulated SC structure to confirm their applicability to SCs. Figure 3.9 indicates the simulated results of I-V curves. From these results, we can observe that all methods effectively removed P_{pz} effect, even as the In-content increased.

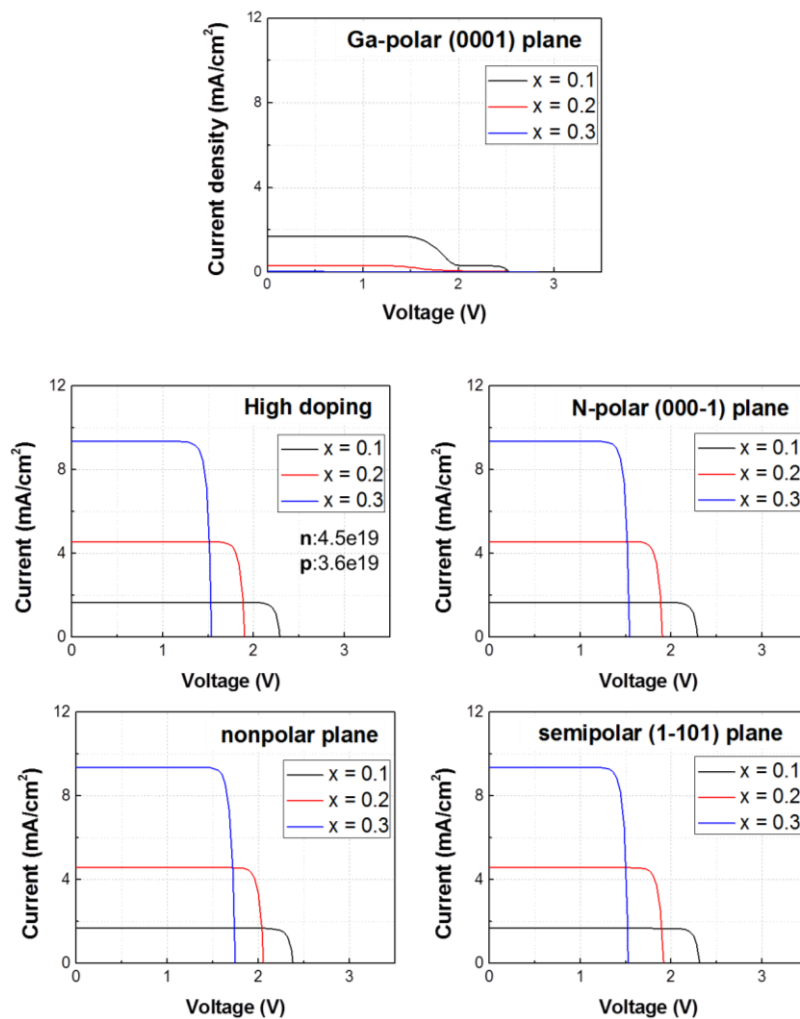


Figure 3.9 I-V curves of InGaN SC structures with different P_{pz} -eliminating techniques as functions of In-content

3.4 Summary

The effects of piezoelectric fields on the carrier dynamics of InGaN-based solar cell structures were investigated. The main findings are listed as follows.

- By changing the strain relaxation constant, we confirmed that the piezoelectric fields in the InGaN layer altered the shape of the energy band in the i-region.
- As the angle of the energy band in the i-region was reduced by the piezoelectric field, significant current loss occurred in the p-i-n $\text{In}_{0.1}\text{Ga}_{0.9}\text{N}$ solar cell structure.
- The current loss was reflected by a staircase-like feature in the I–V curve, which was highly related to the recombination process.
- Despite this current loss, the V_{oc} and J_{sc} properties were slightly improved in the structure with piezoelectric fields.
- The harmful current loss induced by the piezoelectric fields was amplified as the In-content in the InGaN layer increased.
- The current loss was not shown in simulated SCs structure by applying the various methods such as high doping, growth of N-polar (000-1) planes, growth of nonpolar plane, and growth of semipolar plane.

In conclusion, solutions that can eliminate piezoelectric fields are required to realize high-efficiency solar cells, and various methods generally used for LEDs application to control the P_{pz} have also great potential for SCs application.

3.5 References

- 1) J. Wu, W. Walukiewicz, K. M. Yu, J. W. Ager, III, E. E. Haller, H. Lu, W. J. Schaff, Y. Saito, Y. Nanishi, *Appl. Phys. Lett.* **80**, 3967 (2002)
- 2) I. Vurgaftman, J. R. Meyer, *J. Appl. Phys.* **94**, 3675 (2003).
- 3) A. De Vos, *Endoreversible Thermodynamics of Solar Energy Conversion*, Oxford University Press, Oxford, 1992, p. 90.
- 4) Y. Nanishi, Y. Saito, T. Yamaguchi, *Jpn. J. Appl. Phys.* **42**, 2549 (2003).
- 5) O. Jani, I. Ferguson, C. Honsberg, S. Kurtz, *Appl. Phys. Lett.* **91**, 132117 (2007).
- 6) V. Fiorentini, F. Bernardini, F. Della Sala, A. Di Carlo, P. Lugli, *Phys. Rev. B* **60**, 8849 (1999).
- 7) A. E. Romanov, T. J. Baker, S. Nakamura, and J. S. Speck, *J. Appl. Phys.* **100**, 023522 (2006).
- 8) M. Leszczynski, T. Suski, H. Teisseyre, P. Perlin, I. Grzegory, J. Jun, S. Porowski, T.D. Moustakas, *J. Appl. Phys.* **76**, 4909 (1994).
- 9) I. Akasaki, H. Amano, *Jpn. J. Appl. Phys.* **36**, 5393 (1997).
- 10) O. Ambacher, *J. Phys. D.* **31**, 2653 (1998).
- 11) K. Shimada, T. Sota, K. Suzuki, *J. Appl. Phys.* **84**, 4951 (1998).
- 12) F. M. Morales, D. Gonzalez, J. G. Lozano, R. Garcia, S. Hauguth-Frank, V. Lebedev, V. Cimalla, O. Ambacher, *Acta Mater.* **57**, 5681 (2009).
- 13) M. van Schilfhaarde, A. Sher, A.-B. Chen, *J. Cryst. Growth* **178**, 8 (1997).

- 14) S. Nakamura, S. Pearton, G. Fasol, *The Blue Laser Diode*, Springer, Berlin, 2013, p.45
- 15) F. Bernardini, V. Fiorentini, D. Vanderbilt, *Phys. Rev. B* **56**, R10024 (1997).
- 16) Y. Kuwahara, T. Fujii, Y. Fujiyama, T. Sugiyama, M. Iwaya, T. Takeuchi, S. Kamiyama, I. Akasaki, H. Amano, *Appl. Phys. Express* **3**, 111001 (2010).
- 17) C. F. Neufeld, S. C. Cruz, R. M. Farrell, M. Iza, J. R. Lang, S. Keller, S. Nakamura, S. P. DenBaars, J. S. Speck, U. K. Mishra, *Appl. Phys. Lett.* **98**, 243507(2011).

Chapter 4

Comparison between Ga-polar and semipolar InGaN-based solar cells

4.1 Background

III-Nitrides have been extensively utilized in LED and laser diode (LD) applications.¹⁻³⁾ More recently, III-nitrides and InGaN alloys, in particular, have attracted significant attention in photovoltaic applications due to their favorable physical properties, such as direct bandgaps that nearly cover the entire solar spectrum by changing the In-content,⁴⁻⁵⁾ high absorption coefficients,⁶⁾ and high radiation resistance.^{4, 7)} Moreover, a numerical simulation predicted that a highly efficient SC with CE of over 50% could be obtained using an InGaN layer with an In-content of about 40% as an active material system.⁸⁾ However, the reported InGaN-based SCs still show poor device performance because of the difficulty in growing a thick InGaN layer with high crystalline quality and high In-content. One of the important challenges causing such difficulty is the P_{pz} effect. In Chapter 3, we already confirmed that P_{pz} in the p-i-n InGaN/GaN heterostructural SC led to significant current loss, as indicated by the pink region in Fig. 3.3.

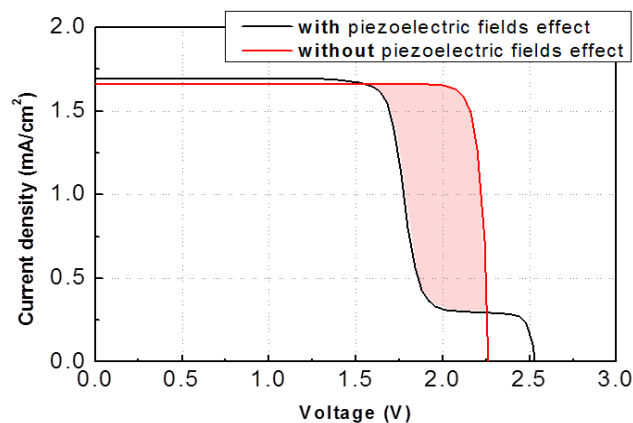
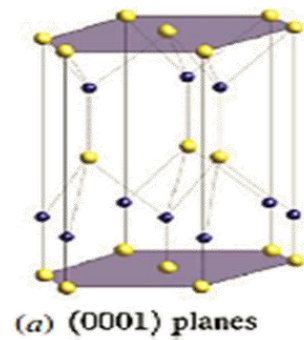


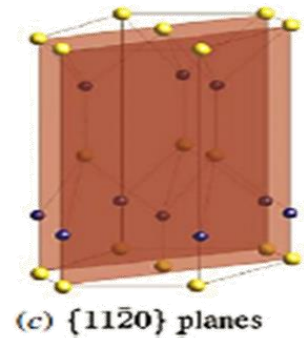
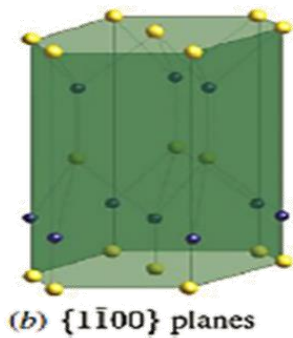
Figure 4.1 Effect of piezoelectric fields on the I-V curve of an InGaN/GaN SC (the same with figure 3.3). The pink region represents current loss

Moreover, since this harmful effect of P_{pz} became more dominant with increasing In-content, the P_{pz} in the InGaN/GaN heterostructure should be controlled to obtain a highly efficient SC. The most widely used method to control the P_{pz} is to grow InGaN/GaN heterostructures on nonpolar or semipolar planes. Representative nonpolar and semipolar planes are depicted in Fig. 4.2.

Ga-polar Plane



Nonpolar Plane



Semipolar Plane

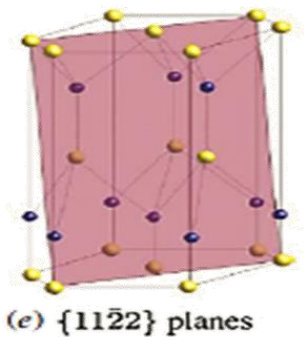
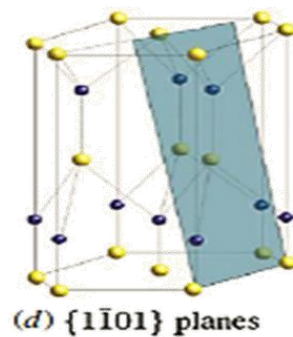


Figure 4.2 Schematic images of a) basic GaN wurtzite structure, b-c) nonpolar planes d-e) semipolar planes⁹⁾

Since the polarization discontinuity changes with the angle from the c-axis and In-content (Fig. 4.3), growth on the nonpolar or semipolar planes can eliminate or reduce the P_{pz} effect. Growth on a semipolar plane is especially advantageous because semipolar planes have been theoretically and experimentally shown to tolerate more indium incorporation compared to c-planes.¹¹⁾ Therefore, InGaN-based SC structure was grown on semipolar (11-22) planes to reduce the P_{pz} , and the properties of this SC structures were compared to those of the conventional (0001) SC structure to confirm the effect of P_{pz} experimentally.

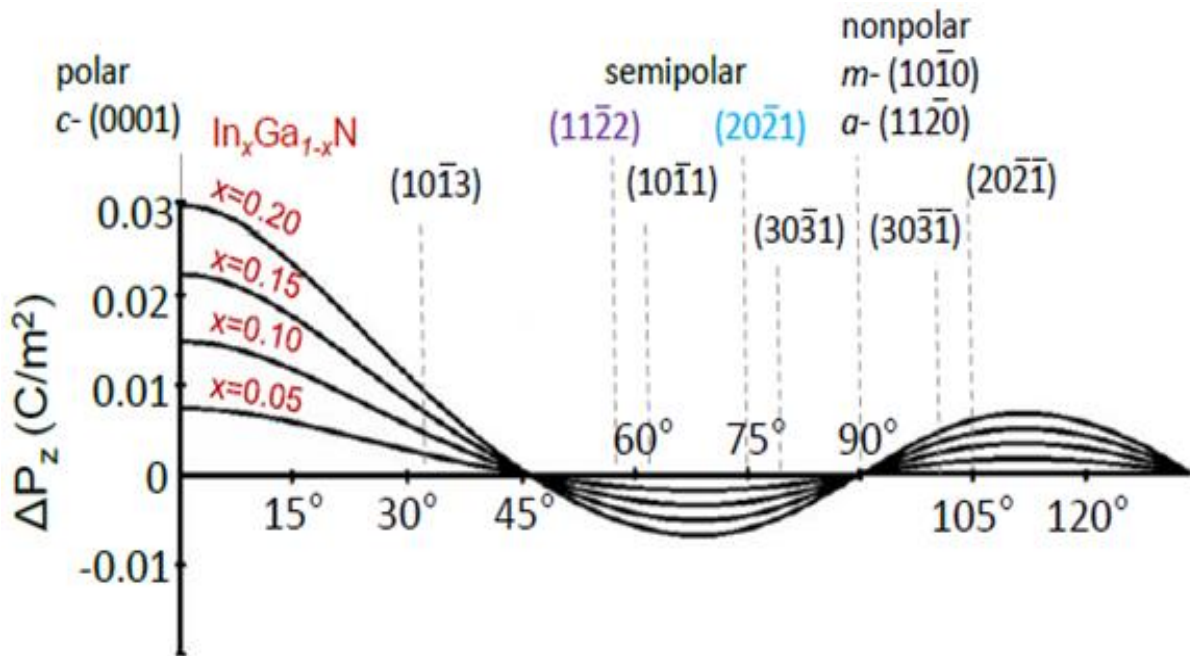


Figure 4.3 Different polarizations at the layer–template interface of the total polarization on the plane orientation for InGaN layers on GaN¹⁰⁾

4.2 Experimental details

Polar (0001) and semipolar (11-22) InGaN/GaN multi-quantum well (MQW) structures were grown by metal-organic chemical vapor deposition (MOCVD) using trimethylgallium, trimethylindium, and ammonia as precursors (Since the growth of semipolar plane structures

has not yet been established in the InGaN-based SC application, general semipolar LED structure was used in this study). The polar and semipolar films were grown on planar c-plane and m-plane sapphire substrates, respectively. The InGaN/GaN MQW structure consisted of a 3- μm -thick undoped GaN layer grown on top of the substrate, a 3- μm -thick Si-doped n-type GaN layer with an electron concentration of $5 \times 10^{18} \text{ cm}^{-3}$ at room temperature, five periods of InGaN/GaN MQWs with a 6-nm GaN barrier and 2.3-nm $\text{In}_{0.24}\text{Ga}_{0.76}\text{N}$ wells, and a 130-nm-thick Mg-doped p-type GaN layer grown on top of the last barrier with a hole concentration of $3 \times 10^{17} \text{ cm}^{-3}$ at room temperature. Before developing the mesa device, the structural properties of the fully grown polar and semipolar InGaN/GaN MQW structures were characterized by optical microscopy (OM), atomic force microscopy (AFM), and scanning electron microscopy (SEM). To examine the optical properties, fluorescence microscopy (FLM) and various photoluminescence (PL) methods (excitation power density-dependent PL, temperature-dependent PL, and μ -PL mapping) were employed. For the PL measurements, a 325-nm He-Cd laser was used as the PL excitation source, and two reflecting microscope objective lenses ($\times 5$ and $\times 39$) were used to simultaneously control the beam spot size and collect the signal. The resolutions of the PL measurements obtained using the $5\times$ and $39\times$ objective lenses were 20 and 1 μm , respectively. After characterization, the grown structures were processed into $350 \times 350 \mu\text{m}^2$ mesas by conventional photolithography and inductively coupled plasma etching with Cl_2 gas. Subsequently, Ti/Al/Ti/Au (30/100/20/150 nm) of n-contact material was deposited by e-beam evaporation, and ITO (150 nm) of p-contact material was formed by sputtering. A schematic image of the fabricated device structure is presented in Fig. 4.4.

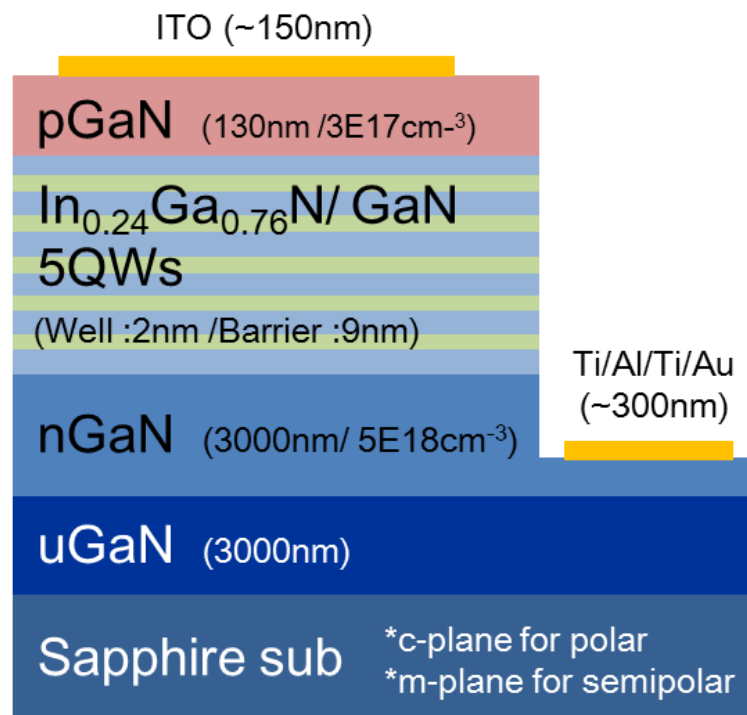


Figure 4.4 Schematic of the InGaN/GaN MQW structures for SCs: c-plane and m-plane sapphire substrates were used for polar and semipolar growth

The device performance and electrical properties were evaluated by electroluminescence (EL) and I–V measurements using an Agilent source meter system. For the I–V measurements, an HAL-320 Solar Simulator with a Xe lamp and AM1.5 filter was used as an illumination source.

4.3 Results and discussion

4.3.1 Photovoltaic performances of polar and semipolar InGaN/GaN MQW SCs

I–V measurements were used to determine the photovoltaic performances of the fabricated polar and semipolar InGaN/GaN MQW SCs. Figure 4.5 shows the I–V curves of the polar and semipolar SCs taken under dark and illuminated conditions, and the detailed device performances are listed in Table 4.1.

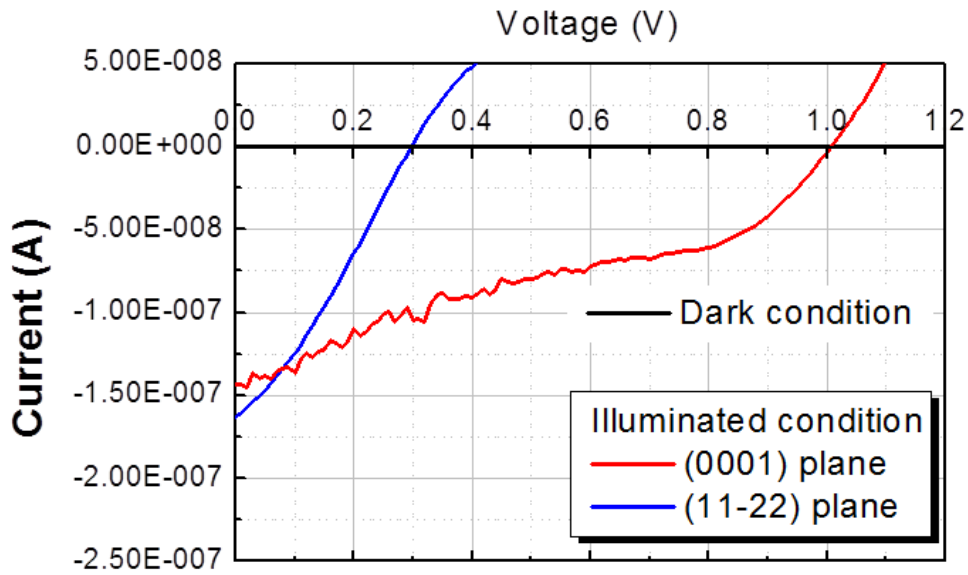


Figure 4.5 I–V curves of polar and semipolar InGaN/GaN MQW SCs measured under dark and illuminated conditions

Table 4.1 Performances of polar and semipolar InGaN/GaN MQWs SCs

	Polar (0001) plane	Semipolar (11-22) plane
V_{oc} (V)	1.0	0.3
J_{sc} (mA/cm²)	0.126	0.133
CE (%)	0.053	0.012
FF (%)	26.5	29.7

The results show that only the J_{sc} and FF values of the semipolar SC were improved compared to the polar SC. Unexpectedly, the values of V_{oc} and CE for the semipolar SC were worse than those for the polar SC. These results differ from those of the simulation described in Chapter 3. To understand these behaviors, the basic optical properties of the polar and semipolar InGaN/GaN MQW structures were determined using PL measurements.

4.3.2 Optical properties of polar and semipolar InGaN/GaN MQW structures

Figure 4.5 shows the PL spectra of polar and semipolar InGaN/GaN MQW structures measured at room temperature. The EL spectra of the devices are also indicated in the inset. As can be seen in this figure, dominant MQW peak is observed in the spectra of both polar and semipolar samples. However, the wavelengths of the MQW peaks differ considerably between the two samples, even though the InGaN/GaN absorption layers were grown to have the same In-content and thickness. Interestingly, the EL spectra of both samples exhibit the same MQW peak wavelength (500 nm). Although the exact reason for this behavior is unclear, it is likely due to different carrier injection mechanisms between PL and EL and/or different injection carrier densities; however, the EL spectra indicate that both samples have the same bandgap energy corresponding to an In-content of 0.24. Moreover, the PL intensity of the semipolar sample was about 2.8 times higher than that of the polar sample.

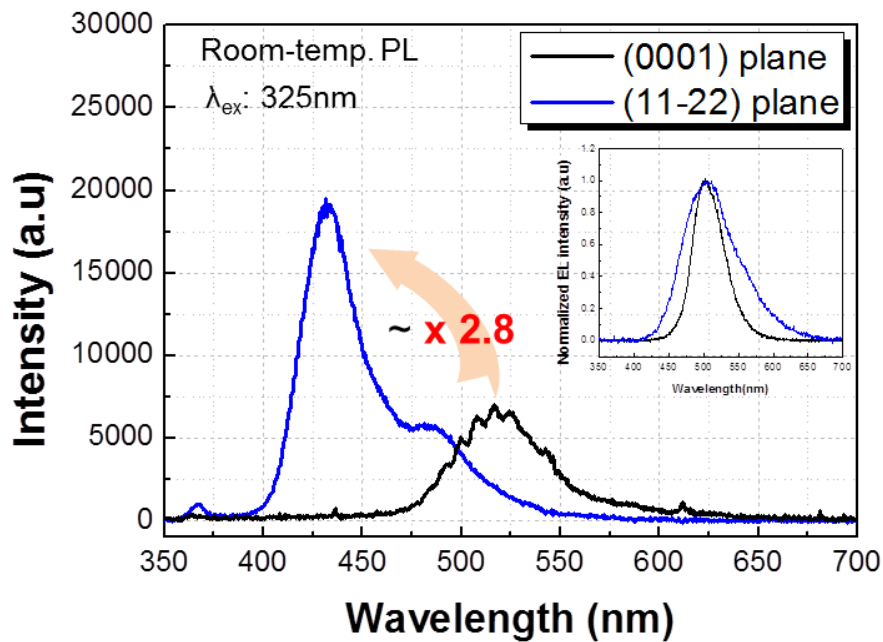


Figure 4.6 PL spectra of polar and semipolar InGaN/GaN MQW structures and the corresponding EL spectra (inset figure)

In such a case, reduced quantum-confined Stark effect (QCSE), decreased dislocation density, and rough surface morphology can lead to increases in PL intensity.

4.3.3 Estimation of crystal quality

Among these characteristics, dislocation density is the most well-known factor that decreases PL intensity. Thus, the crystal qualities of the polar and semipolar InGaN/GaN MQW structures were estimated by low-temperature (10 K) PL measurements. Figure 4.7 shows the PL spectra of the polar and semipolar samples taken at an excitation power density of 60.89 kW/cm².

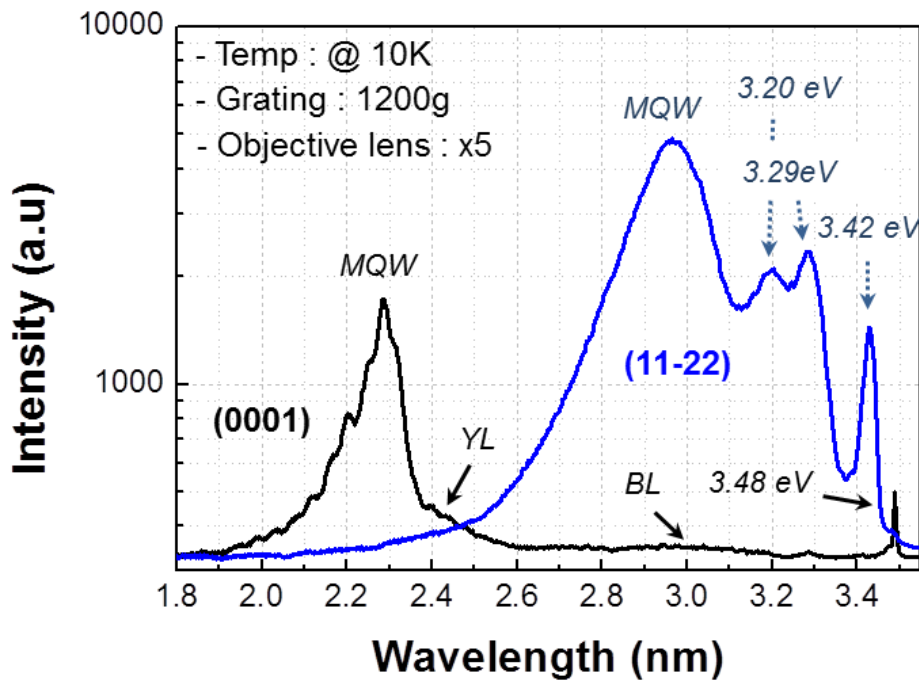


Figure 4.7 Low-temperature PL spectra of polar and semipolar InGaN/GaN MQW structures measured at 10 K

As for the room-temperature PL spectra, it is also indicated that the MQW peak intensity for the semipolar sample was much higher than that for the polar sample. However, the emission shapes of the polar and semipolar samples were significantly different. Although the MQW peaks were clearly observed for both samples, the PL spectrum of the semipolar sample showed several defect-related emissions, unlike the polar sample. The emissions at 3.42 and 3.29 eV in the spectrum of the semipolar sample are attributed to basal stacking faults¹²⁻¹³⁾ and partial dislocation,¹²⁾ respectively, which are typically formed in semipolar III-N epitaxial films. Thus, the PL spectra indicate that more defects states existed in the semipolar sample than in the polar sample. To verify this result, the internal quantum efficiencies (IQEs) of the polar and semipolar InGaN/GaN MQW structures were determined using temperature-dependent PL measurements taken at an excitation power density of 60.89 kW/cm² with temperature varying from 10 to 300 K.

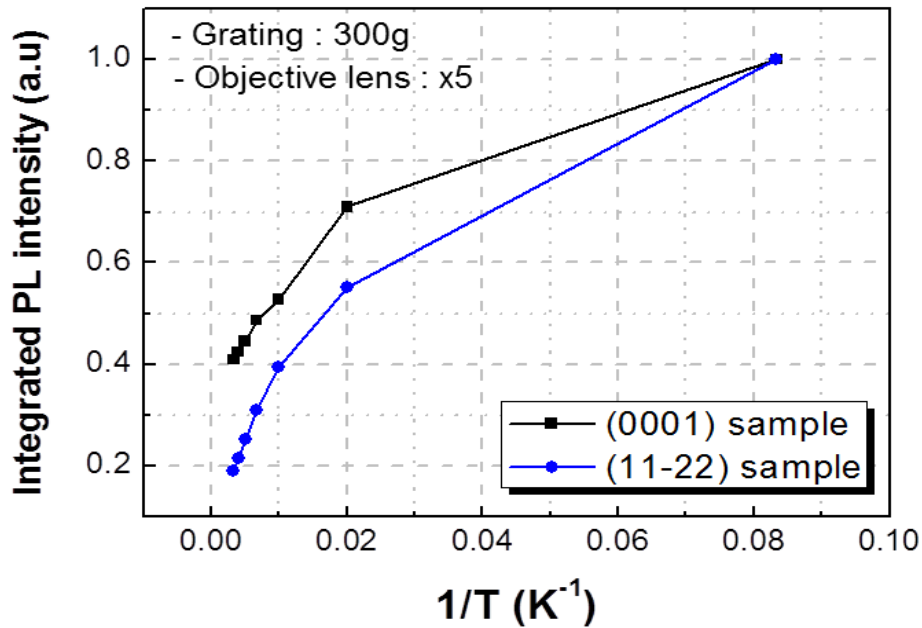


Figure 4.8 Normalized integrated PL intensities of MQWs for the polar and semipolar InGaN/GaN MQW structures as functions of temperature (10 to 300 K)

By assuming that the non-radiative recombination rate becomes zero at low temperature (10 K), the IQE values can be estimated by dividing the integrated PL intensity measured at 10 K by that measured at 300 K. Figure 4.8 shows that the IQE values estimated for the polar and semipolar samples are approximately 40% and 19%, respectively. Thus, the IQE values confirm that the semipolar sample may contain a much higher defect density than the polar sample.

4.3.4 Examination of QCSE

The results indicating a higher defect density in the semipolar sample are quite contrary to the room-temperature PL results showing increased PL intensity for the semipolar sample. To resolve this discrepancy, another factor that affects PL intensity, QCSE, was examined

through PL measurements by changing the excitation power density from 0.49 to 60.89 kW/cm². To minimize the In-fluctuation effect, ×39 objective lens was used.

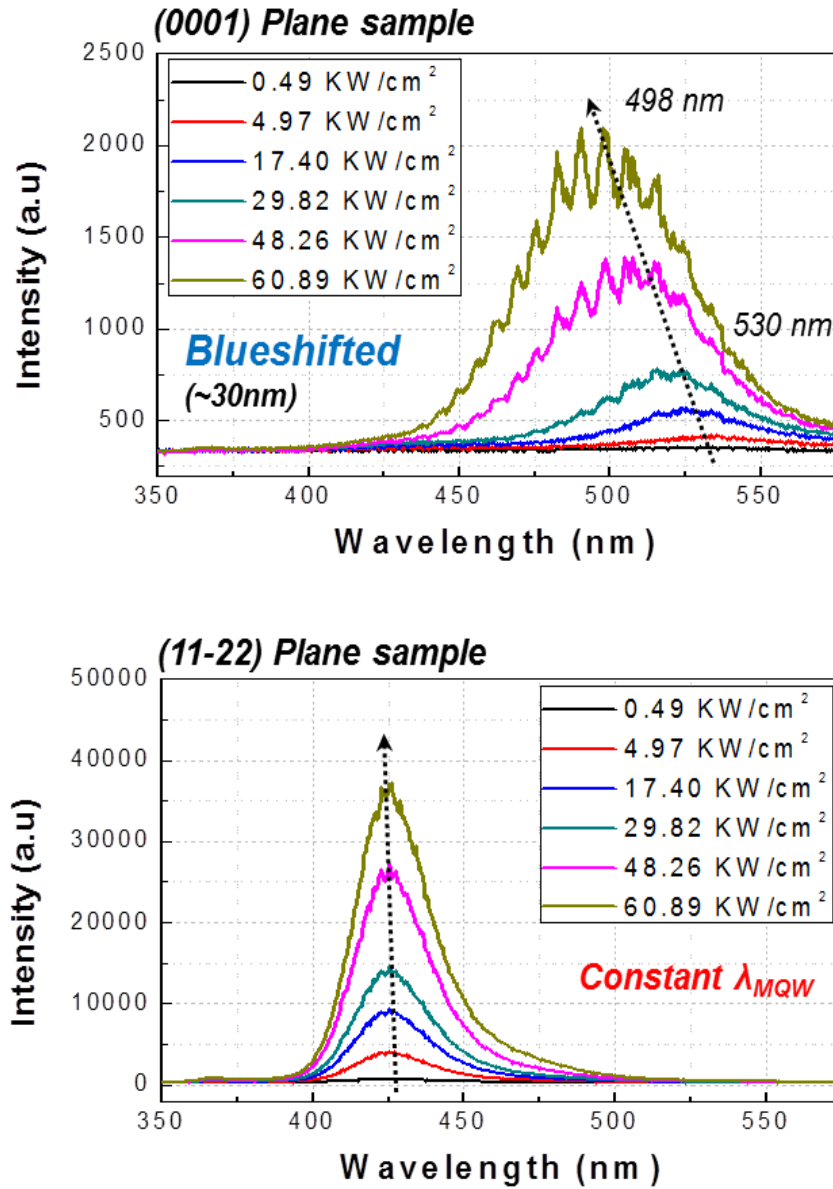


Figure 4.9 PL spectra of the polar and semipolar InGaN/GaN MQW structures as functions of excitation power density (0.49 to 60.89 kW/cm²)

As indicated in this figure, the MQW peak wavelength of the polar sample was blue-shifted from 530 to 498 nm by increasing the excitation power density. This blue-shifted wavelength

is commonly observed because the tilted energy band caused by the P_{pz} effect is screened by increasing the carrier density with an increase in excitation power density.¹⁴⁾ Thus, a large blue-shift of approximately 30 nm for the polar sample indicates that a strong QSCE existed in the polar sample. Unlike the polar sample, the MQW peak wavelength of the semipolar sample remained almost constant with increasing excitation power density. These results suggest that the QCSE in the InGaN/GaN MQW structure was effectively reduced by semipolar plane growth. This reduced QCSE effect in the semipolar sample can explain enhanced PL intensity.

4.3.5 Evaluation of surface morphology

In addition to QCSE, surface roughness also has significant impacts on optical properties. Thus, the surface morphologies of the polar and semipolar InGaN/GaN MQW structures were evaluated by AFM and SEM measurements (Fig. 4.10). The results show that the surface morphologies of the samples had significantly different surface morphology. The surface of the semipolar sample exhibited a high density of arrowhead-like features, while the polar sample showed a mirror-like surface. Since the surfaces of semipolar (11-22) GaN-based films are generally dominated by arrowhead-like features consisting of vicinal facets related to the (10-11) plane,¹⁵⁾ the semipolar sample exhibited a rougher surface than the polar sample. Correspondingly, the root-mean-squared roughness values for the polar and semipolar samples were 0.475 and 21.47 nm, respectively, over typical $5\ \mu\text{m} \times 5\ \mu\text{m}$ areas.

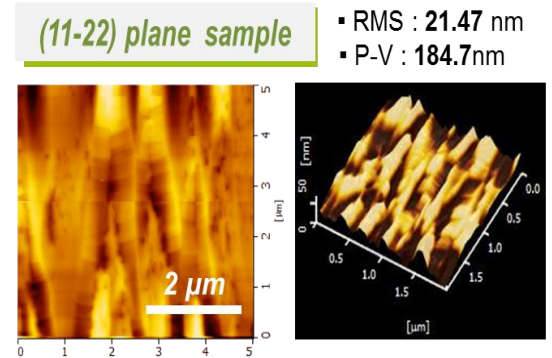
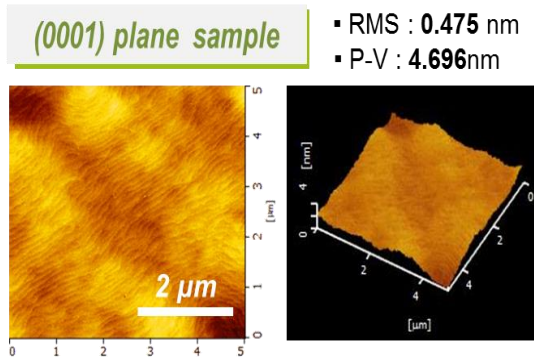
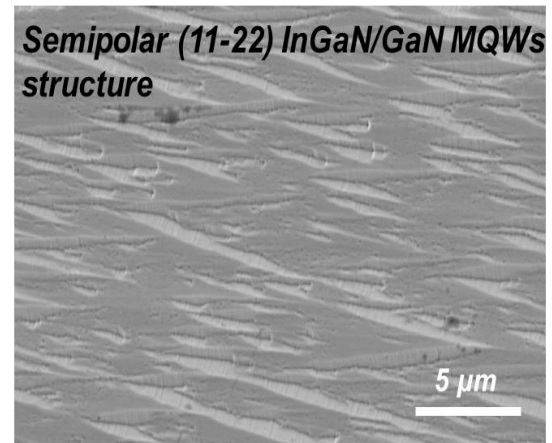
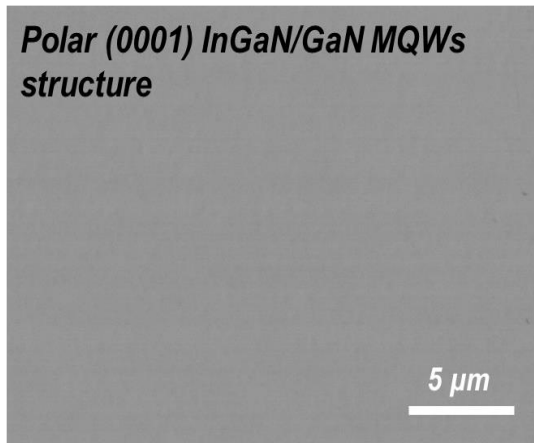


Figure 4.10 SEM and AFM images of polar and semipolar InGaN/GaN MQW structures

4.3.6 Determination of In-fluctuation

The rough surface morphology of the semipolar sample may lead to In-fluctuation, which can degrade device performance. Thus, micro-PL mapping images of the PL wavelength, intensity, and full width at half maximum (FWHM) for the polar and semipolar InGaN/GaN MQW structures are shown in Fig. 4.11.

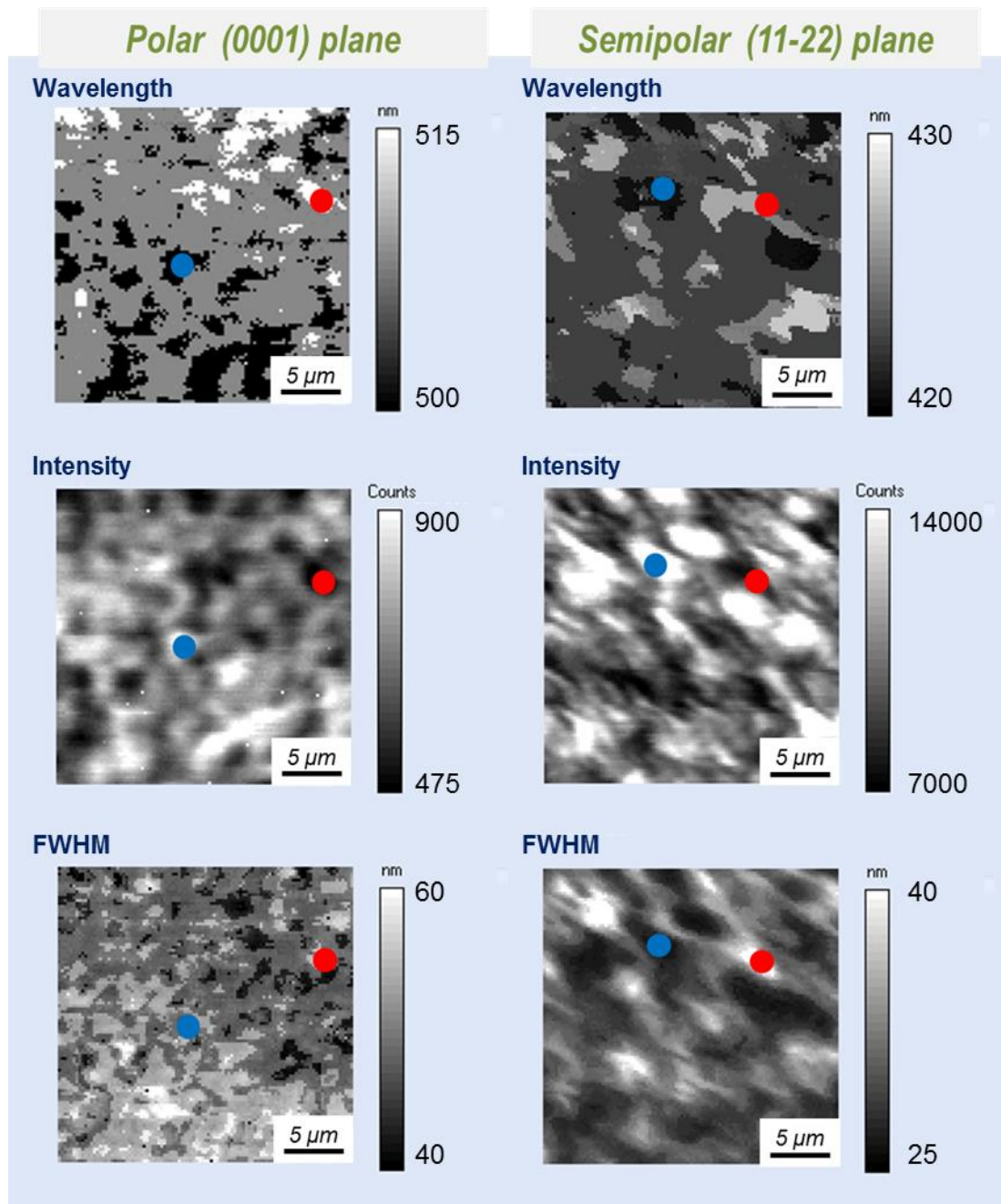
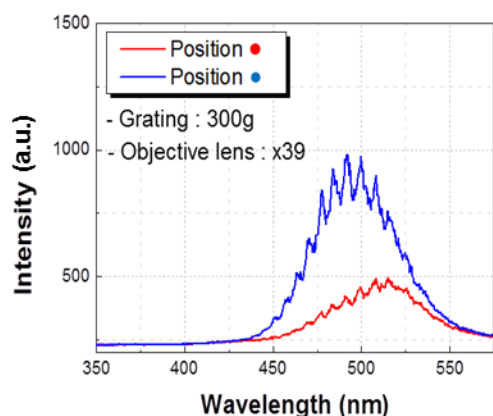


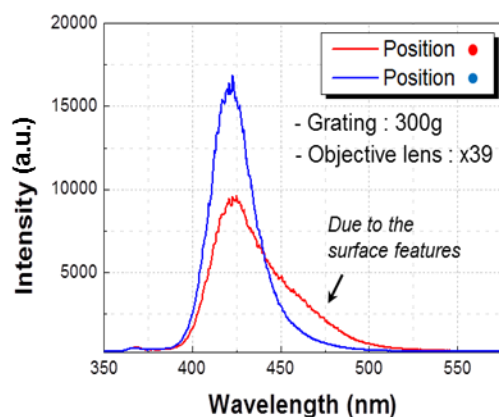
Figure 4.11 Micro-PL mapping images of the PL wavelength, intensity, and FWHM for polar and semipolar InGaN/GaN MQW structures

Even though the polar sample had a mirror-like surface morphology, a high density of some dotted shapes was observed in the measured area. The semipolar sample also exhibited some arrowhead-like features, as seen in the SEM and AFM images. To further study these characteristics, point spectra (Fig. 4.12) were collected at the positions indicated by the blue and red dots in Fig. 4.11. The detailed PL properties are also listed in the tables in Fig. 4.12.



(0001) plane sample

	Position (blue)	Position (red)
Wavelength (nm)	492	515
Intensity (a.u.)	1000	500
FWHM (nm)	45	60



(11-22) plane sample

	Position (blue)	Position (red)
Wavelength (nm)	422	425
Intensity (a.u.)	17000	9700
FWHM (nm)	45	60

Figure 4.12 Point spectra collected at the positions indicated by the red and blue dots in Fig. 4.11. The detailed properties of the PL spectra are listed in the tables

The regions indicated by the red dots were In-rich regions, whereas the positions indicated by blue dots were regions with poor In-content. The PL spectra collected at the blue dot positions showed short wavelengths and high intensities with narrow FWHM values, whereas

those taken at the red dot positions exhibited long wavelengths and low intensities with wide FWHM values. These results suggest that both samples exhibited severe In-fluctuation. Since the surface of the semipolar sample was rough and exhibited specific features, the accumulated shapes (arrowhead-like shapes) of In in the semipolar sample were also significantly affected by the surface morphology. However, comparing the results of the polar and semipolar samples indicates that the difference in wavelength between the blue and red positions is larger for the polar sample than for the semipolar sample. Thus, In-fluctuation may have been more severe in the polar sample.

4.3.7 Correlation between various characteristics and photovoltaic performance

The previously confirmed characteristics of the structures are listed in Table 4.2. The characteristics that negatively affected the photovoltaic performance are indicated in red.

Table 4.2 Various characteristics of polar and semipolar InGaN/GaN MQW structures

	Polar (0001) plane sample	Semipolar (11-22) plane sample
Defect density	High defect density	Higher defect density
QCSE	Strong	Almost negligible
Surface roughness	Mirror-like (RSM: 0.475 nm) : high reflectivity	Rough (RMS: 21.47 nm) : low reflectivity
In-fluctuation	More severe	severe

As shown in the table, the semipolar sample contained a higher dislocation density than the polar sample. A high defect density generally causes V_{oc} and J_{sc} to decrease; however, the J_{sc} value for the semipolar sample was slightly higher than that for the polar sample. This is

probably due to the negligible QCSE and low reflectivity caused by the rough surface morphology of the semipolar sample. Since we already observed that a strong QCSE decreased the value of FF in Chapter 3, the increased FF value observed for the semipolar sample might have been caused by a reduction in QCSE. However, since the variety of characteristics such as different surface morphology, In-fluctuation and defect density were involved, effect of P_{pz} on photovoltaic behavior couldn't be confirmed separately.

4.4 Summary

To prevent the harmful effects of P_{pz} , an InGaN/GaN NQW SC was grown on a semipolar (11-22) plane, and the fabricated device was compared with a conventional polar (0001) plane device. The major findings are listed as follows.

- Growing the InGaN solar cell on a semipolar (11-22) plane resulted in better optical properties compared to the sample grown on a polar plane.

- 1) QCSE was almost negligible in the (11-22) sample, unlike in the (0001) sample.

- 2) Due to the arrowhead-like surface features, the (11-22) sample had a rough surface morphology, while the (0001) sample showed a mirror-like surface, resulting in high reflectivity.

- 3) In-fluctuation was observed in both samples, although the effect was weaker in the semipolar sample.

- The defect density was higher in the semipolar sample than in the polar sample.

As a result, a high defect density might cause V_{oc} and J_{sc} to decrease. However, the J_{sc} value for the semipolar sample was slightly higher than that for the polar sample probably due to the negligible QCSE and low reflectivity caused by the rough surface morphology of the semipolar sample. Moreover, the increased FF value observed for the semipolar sample might have been caused by a reduction in QCSE.

In conclusion, growth on the semipolar (11-22) plane is a promising technique for solar applications due to the resulting good In-incorporation, low reflectivity, and reduced QCSE effect when it is possible to overcome the problem of high defect density.

4.5 References

- 1) E. F. Schubert, *Light Emitting Diodes*, Cambridge University Press, New York, 2006.
- 2) S. Nakamura, G. Fasol, *The Blue Laser Diode: The Complete Story*, Springer, Berlin, 2000.
- 3) S. W. Feng, L. W. Tu, J. I. Chyi, H. C. Wang, *Thin Solid Films* **517**, 909 (2008)
- 4) J. Wu, W. Walukiewicz, K. M. Yu, J. W. Ager, E. E. Haller, H. Lu, W. J. Schaff, Y. Saito, Y. Nanishi, *Appl. Phys. Lett.* **80**, 3967 (2002).
- 5) I. Vurgaftman, J. R. Meyer, *J. Appl. Phys.* **94**, 3675 (2003).
- 6) A. David, M. J. Grundmann, *Appl. Phys. Lett.* **97**, 033501 (2010).
- 7) J. Q. Wu, *J. Appl. Phys.* **106**, 011101 (2009)
- 8) A. De Vos, *Endoreversible Thermodynamics of Solar Energy Conversion*, Oxford University Press, Oxford, 1992, p. 90.
- 9) F. Scholz, *Semicond. Sci. Technol.* **27**, 024002 (2012).
- 10) A. E. Romanov, T. J. Baker, S. Nakamura, J. S. Speck, *J. Appl. Phys.* **100**, 23522 (2006).
- 11) J. E. Northrup, *Appl. Phys. Lett.* **95**, 133107 (2009).
- 12) R. Liu, A. Bell, F. A. Ponce, C. Q. Chen, J. W. Yang, M. A. Khan, *Appl. Phys. Lett.* **86**, 021908 (2005).
- 13) J. Mei, S. Srinivasan, R. Liu, F. A. Ponce, Y. Narukawa, T. Mukai, *Appl. Phys. Lett.* **88**, 141912 (2006).
- 14) H. Yu, L. K. Lee, T. Jung, P. C. Ku, *Appl. Phys. Lett.* **90**, 141906 (2007).

15) M. J. Kappers, J. L. Hollander, C. McAleese, C. F. Johnston, R. F. Broom, J. S. Barnard, M. E. Vickers, C. J. Humphreys, *J. Cryst. Growth* **300**, 155 (2007).

Chapter 5

Effect of defects on the device performances of InGaN-based solar cells

5.1 Background

III-Nitrides have been extensively utilized in LED and LD applications.¹⁻³⁾ More recently, III-nitrides and InGaN alloys, in particular, have attracted significant attention in photovoltaic applications due to their favorable physical properties, such as direct bandgaps that nearly cover the entire solar spectrum by changing the In-content,⁴⁻⁵⁾ high absorption coefficients,⁶⁾ and high radiation resistance.^{4, 7)} Moreover, a numerical simulation predicted that a highly efficient SC with CE over 50% can be obtained using an InGaN layer with an In-content of about 40% as an active material system.⁸⁾ However, the reported InGaN-based SCs still show poor device performance because of the difficulty in growing a thick InGaN layer with high crystalline quality and In-content. This difficulty is related to various problems including high defect density, existence of P_{pz} , and severe In-fluctuation effect in InGaN-based SCs. Among these problems, dislocation density is known as a critical factor that negatively impacts the performance of GaN-based p-n junction devices.⁹⁾ Therefore, many researchers have developed strategies to reduce the dislocation density in epitaxial layers. Along with developing techniques to reduce dislocations, it is also important to understand the phenomena caused by dislocations. However, to date, no reports have described the specific effects of dislocation density on the photovoltaic behaviors of InGaN-based SCs. Therefore, we applied a SiN_x insertion layer, which is commonly used to reduce dislocation density in LED applications,¹⁰⁻¹¹⁾ to the InGaN-based SC structure. The photovoltaic behaviors of the resulting device were then characterized experimentally and theoretically.

5.2 Experimental details

5.2.1 Basic properties of the prepared GaN templates

To reduce dislocation density, a 3- μm -thick GaN template was first grown on a c-plane sapphire substrate using a SiN_x insertion layer deposited on the buffer layer (see Fig. 5.1). For comparison, a GaN template grown without the SiN_x insertion layer was also prepared. These two structures were labeled as SiN_x -type and planar-type. The dislocation densities of both GaN templates were evaluated by symmetric (002) and asymmetric (102) reflection x-ray diffraction (XRD) ω -scan rocking curve measurements. The FWHM values of the (002) rocking curves for the planar- and SiN_x -type GaN templates were 306 and 248 arcsec, respectively. Similarly, the FWHM value of the (102) rocking curve for the SiN_x -type GaN template (408 arcsec) decreased compared to that of the planar-type GaN template (662 arcsec). Since the x-ray ω -scan curves on the symmetric (002) and asymmetric (102) planes of GaN are known to be sensitive to screw- and edge-type dislocations, respectively, the reduced FWHM values suggested that the overall dislocation density in the SiN_x -type GaN template decreased relative to the planar-type GaN template. Furthermore, from these results, the dislocation densities for the planar- and SiN_x -type GaN templates were estimated to be 1.97×10^9 and $8.05 \times 10^8 \text{ cm}^{-2}$, respectively.

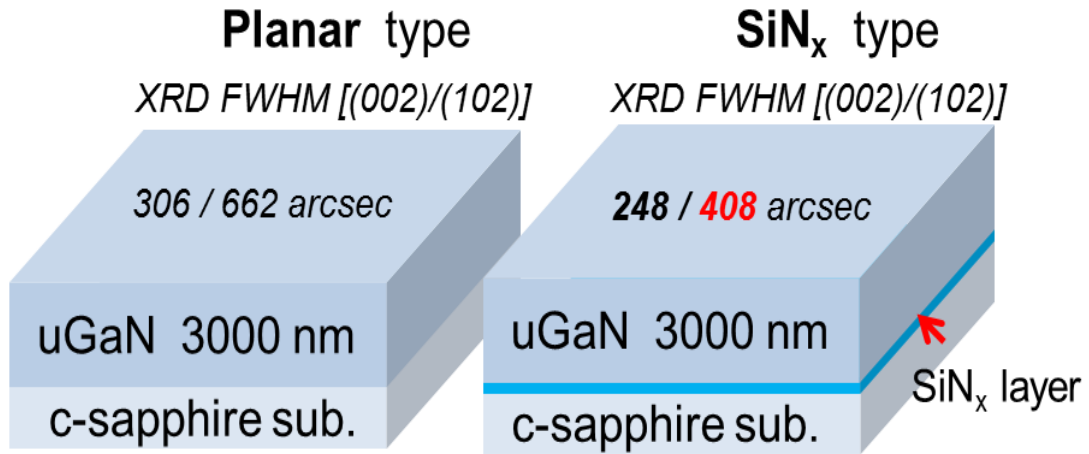


Figure 5.1 Prepared GaN templates with different dislocation densities; a SiN_x insertion layer was deposited on the buffer layer to reduce dislocation density

5.2.2 Basic properties of p-i-n InGaN/GaN heterostructures

The p-i-n InGaN/GaN heterostructure shown in Fig. 5.2 was simultaneously grown on the two different GaN templates. The p-i-n structure consisted of a 3- μm -thick Si-doped n-type GaN layer with an electron concentration of $5 \times 10^{18} \text{ cm}^{-3}$ at room temperature; a 20-nm-thick intrinsic In_{0.09}Ga_{0.91}N absorption layer with an In-content of 0.09, as determined from the XRD (002) ω -2 θ scanning curve profile; and a 130-nm-thick Mg-doped p-type GaN layer with a hole concentration of $3 \times 10^{17} \text{ cm}^{-3}$ at room temperature (To mainly focus on the effect of dislocations, relatively thin InGaN absorption layer with low In-content was used to minimize other effects such as P_{pz} and In-fluctuation). The surface morphologies of the fully grown structures were also characterized by AFM. As shown in Fig. 5.3, both heterostructures showed smooth surfaces and similar roughness; the RMS roughness values of the planar- and SiN_x-type structures were 0.35 and 0.39 nm, respectively, over typical $2 \mu\text{m} \times 2 \mu\text{m}$ areas. All structures were grown by MOCVD using trimethylgallium, ammonia,

and trimethylindium as the sources of Ga, N, and In sources, respectively. Following the MOCVD growth, p-i-n heterostructures were fabricated on $350 \times 350 \mu\text{m}^2$ mesa devices formed by conventional photolithography and inductively coupled plasma etching techniques. Contacts to n-type were formed by the electron beam evaporation of Ti/Al/Ti/Au (30/100/20/150 nm), and a 150-nm layer of indium tin oxide was deposited to form the p-type contacts by sputtering.

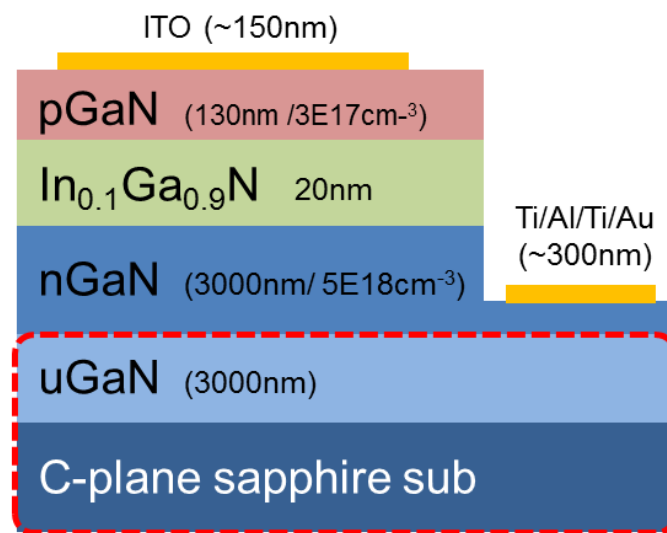


Figure 5.2 Schematic image of a p-i-n InGaN/GaN heterostructure SC

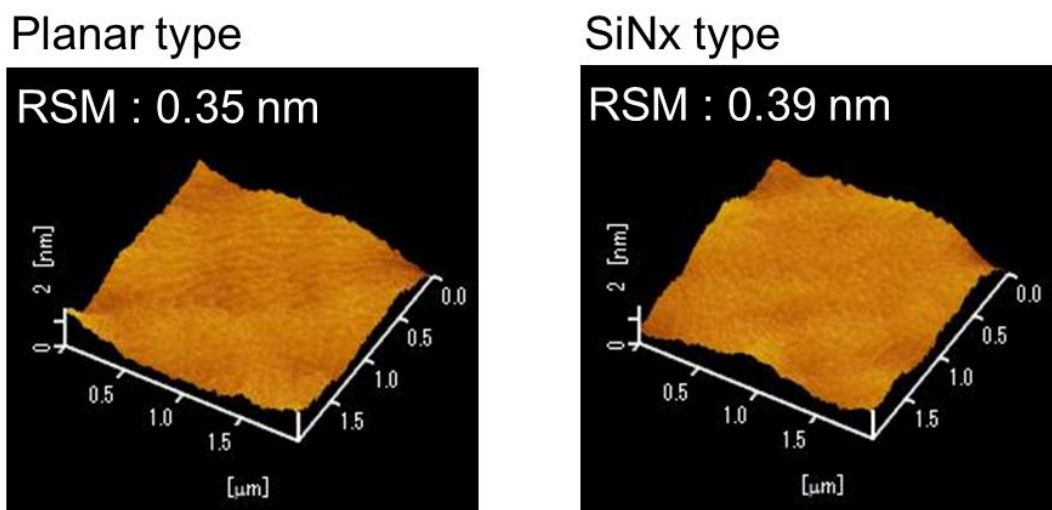


Figure 5.3 AFM images of the p-i-n InGaN/GaN heterostructures grown on planar- and SiN_x-type GaN templates

5.2.3 Characterization

For the p-i-n structures, both planar- and SiN_x-type samples were characterized by AFM (NanoNavi IIs) and XRD (PANalytical X'-pert PRO MRD diffractometer). Photoluminescence (PL) measurements were taken at various temperatures ranging from 11 K to room temperature by changing the excitation power density from 37.2 to 372.4 W/cm². A 325-nm He-Cd laser was used as the PL excitation source, and a reflecting microscope with a ×5 objective lens was used to control the beam spot size and collect the signal. The recombination rates and band diagrams were simulated using SCSim software. For the mesa device, the current density versus voltage (J–V) measurement was performed using an Agilent source meter system. An HAL-320 Solar Simulator with a Xe lamp and an AM1.5 filter was used as the illumination source.

5.3 Results and discussion

5.3.1 Optical properties of planar- and SiN_x-type p-i-n InGaN/GaN heterostructures

Figure 5.4 shows the room-temperature PL spectra of the planar- and SiN_x-type p-i-n InGaN/GaN heterostructures collected at an excitation power density of 112 W/cm². As illustrated in Fig. 5.4, dominant InGaN emissions were observed at around 407 nm in the spectra of both samples along with weak near-band edge emissions located at 363 nm attributed to the top of the p-type GaN layers. Therefore, both samples had the same bandgap energy of 3.05 eV (407 nm), which matched well with the previous XRD (002) ω -2 θ results for an In-content of 0.09 in the InGaN layer. Unlike the emission wavelength, the intensity of the InGaN emission was almost two times higher for the SiN_x-type sample than for the planar-type sample.

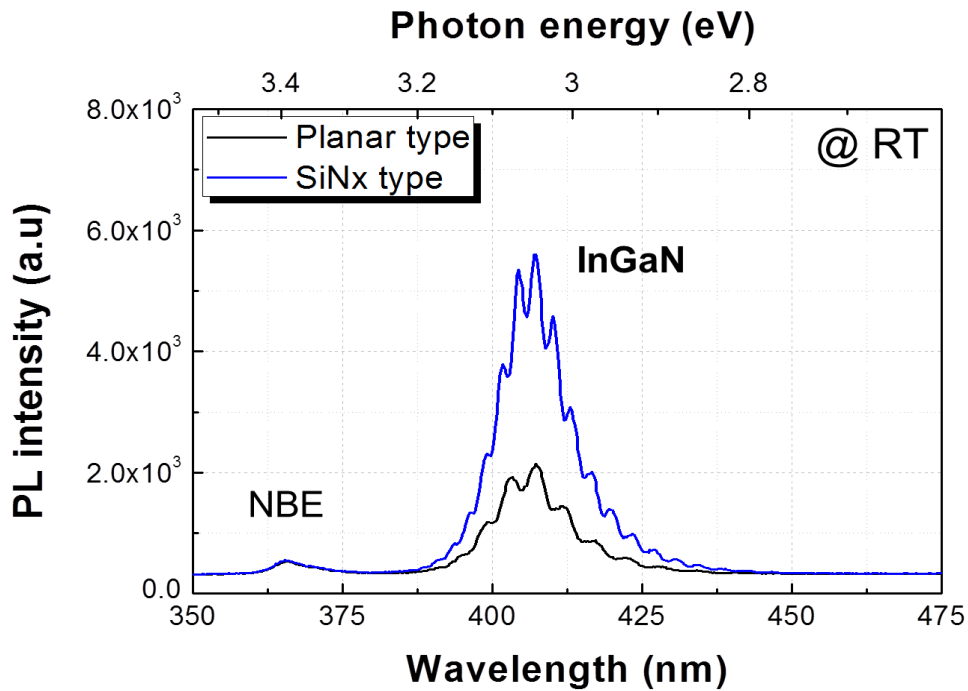


Figure 5.4 Room-temperature PL spectra of planar- and SiN_x-type p-i-n InGaN/GaN heterostructures

An increase in PL intensity may be related to several factors, such as a reduction in QCSE, rough surface morphology, and a reduction in the number of non-radiative centers (NRCs). The AFM images already confirmed that the surface roughness was nearly the same in both samples (see Fig. 5.3). Moreover, excitation power-dependent PL spectra shown in Fig. 5.5 indicate that QCSE was not observed in both samples because the wavelength of InGaN emission did not change as the excitation power density increased from 37.2 to 372.4 W/cm². Since fully strained InGaN layers were also characterized by reciprocal space mapping (RSM) in both samples, this behavior is probably due to the weak internal electric fields caused by relatively low In-content. These results suggest that the observed increase in the intensity of InGaN emission for the SiN_x-type sample was significantly associated with the reduction in the number of NRCs as a result of the decreasing dislocation density.

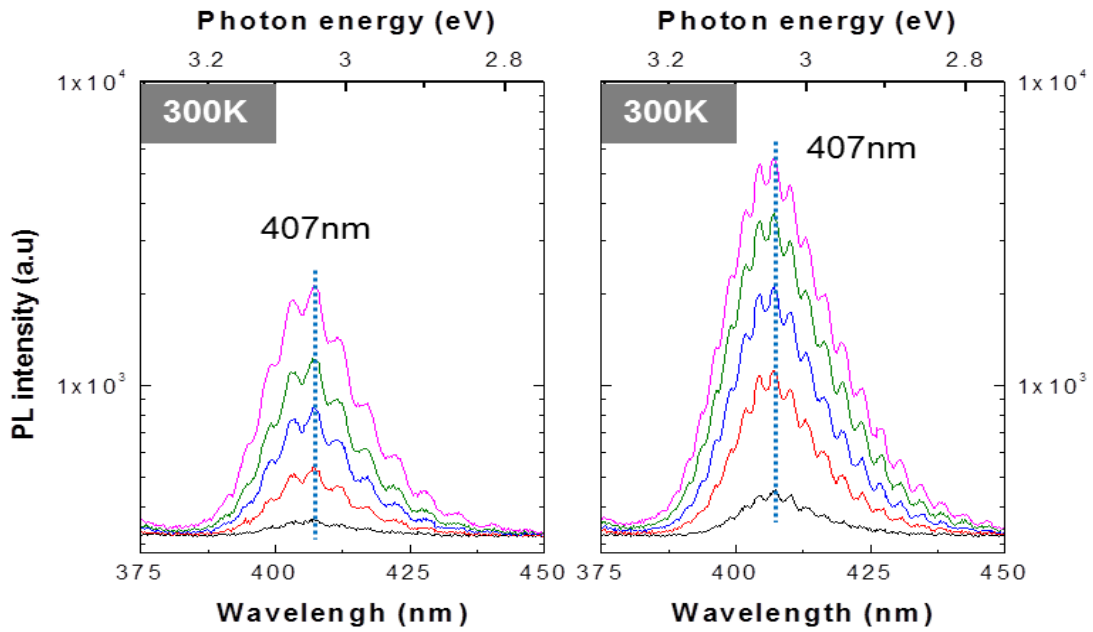


Figure 5.5 PL spectra of planar- and SiN_x-type p-i-n InGaN/GaN heterostructures as functions of excitation power density (37.2–372.4 W/cm²)

The plots of integrated PL intensity of the InGaN emission as a function of excitation power density also supported this suggestion. As indicated in Fig. 5.6, the integrated PL intensity gap between the planar- and SiN_x-type samples increased with the excitation power density.

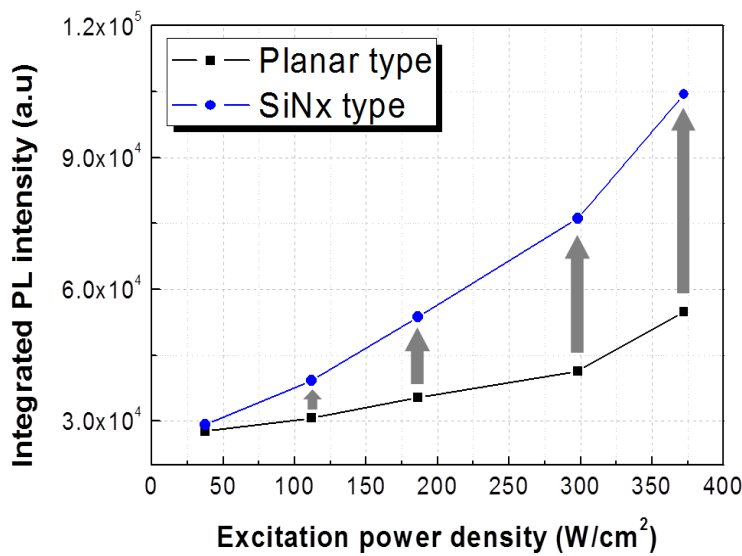


Figure 5.6 Integrated PL intensity of planar- and SiN_x-type p-i-n InGaN/GaN heterostructures with varying excitation power density (37.2–372.4 W/cm²)

Compensating NRCs with photogenerated carriers is known to increase the possibility of radiative recombination. Thus, the greater intensity of integrated InGaN emission in the SiN_x-type sample was likely caused by the greater compensation of NRCs by photogenerated carriers in the SiN_x-type sample compared to the planar-type sample. Thus, compared to the planar-type sample, the SiN_x-type sample exhibited enhanced optical properties due to the decreased number of NRCs. Accordingly, the FWHM values of the InGaN emissions for the planar- and SiN_x-type samples were 12.6 and 10.8 nm, respectively.

5.3.2 Evaluation of the In-fluctuation effect

To characterize the p-i-n heterostructures in more detail, PL measurements were performed by varying the temperature from 11 to 300 K at different excitation power densities. Representative results obtained at excitation power densities of 112 and 298 W/cm² are shown in Figs. 5.7 and 5.8, respectively.

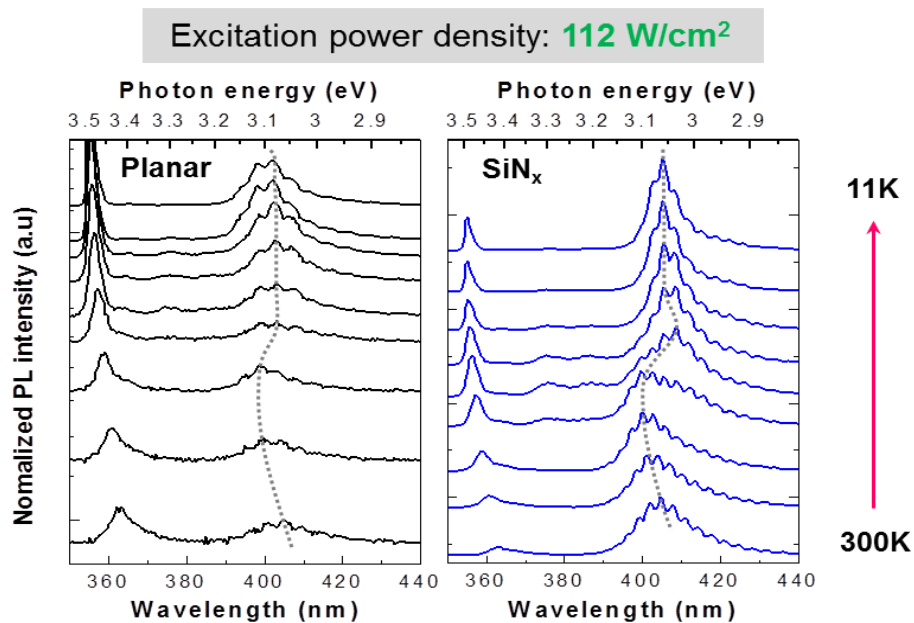


Figure 5.7 PL spectra of planar- and SiN_x-type p-i-n InGaN/GaN heterostructures as functions of temperature (11–300 K) at an excitation power density of 112 W/cm²

In Fig 5.7, the wavelengths of InGaN emissions exhibited s-shaped temperature-dependent shifts for both samples. These shifts are commonly attributed to energy band fluctuation caused by QCSE and/or the In-fluctuation effect.¹²⁾ However, since QCSE was negligible in both samples (Fig. 5.5), the observed s-shaped emission shifts in this study were attributed to In-fluctuation effects. Noticeable point in this statement is that such emission shift was not indicated in the results of excitation power density-dependent PL spectra taken under room-temperature condition (see Fig. 5.5), although the energy band fluctuated under the In-localization effect. This result can be explained by examining the shape of InGaN emission as a function of temperature, particularly for the SiN_x-type sample (Fig. 5.7). With decreasing temperature, an additional emission that was not observed at room temperature began to emerge in the lower-energy side (~3.04 eV) of the main InGaN emission (~3.10 eV). However, when the intensity of the extra emission reached a certain level, its intensity stopped increasing, and it merged with the InGaN emission with further decreases in temperature. These results indicated that the extra emission originated from the defect-related states. Since In has been reported to be more localized at positions with dislocations,¹³⁾ the longer wavelength of the extra emission compared to that of the InGaN emission can also be explained. The shift in emission was not observed at room temperature by increasing the excitation power density because the localized states were connected with NRCs. Interestingly, the strengths of the In-fluctuation effect in the planar- and SiN_x-type samples were different. The s-shaped emission shift related to the In-fluctuation effect was not observed in the planar-type sample when the excitation power density exceeded 298 W/cm² (compare Figs. 5.7 and 5.8). This means that the In-fluctuation effect was stronger in the SiN_x-type sample than in the planar-type sample.

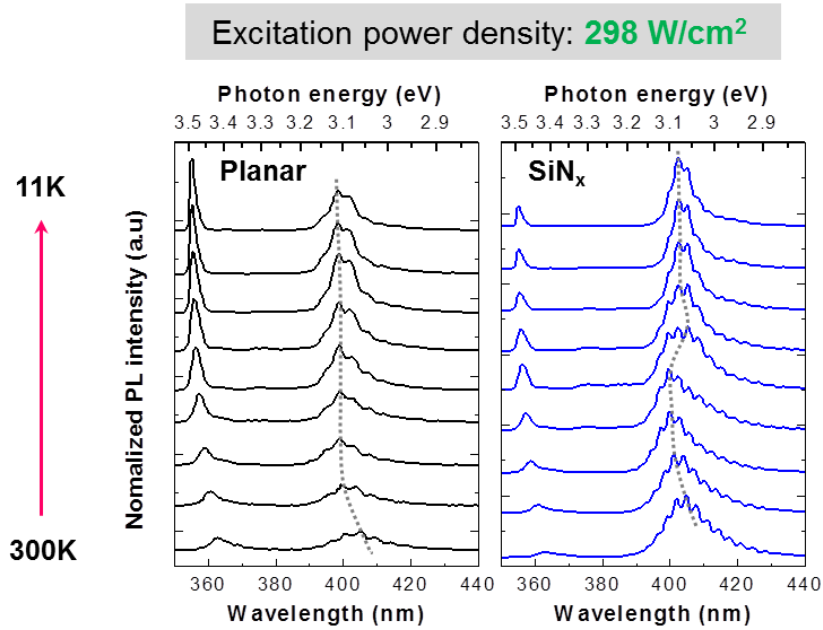


Figure 5.8 PL spectra of p-i-n InGaN/GaN heterostructure for planar and SiN_x-type as a function of temperature ranging from 11 to 300 K at excitation power density of 298 W/cm²

5.3.3 Determination of photovoltaic performances

To evaluate the photovoltaic properties, Fig. 5.9 shows the J–V curve measured under 1.5AM and 1 sun illumination conditions. The detailed device performances are also listed in Table 5.1.

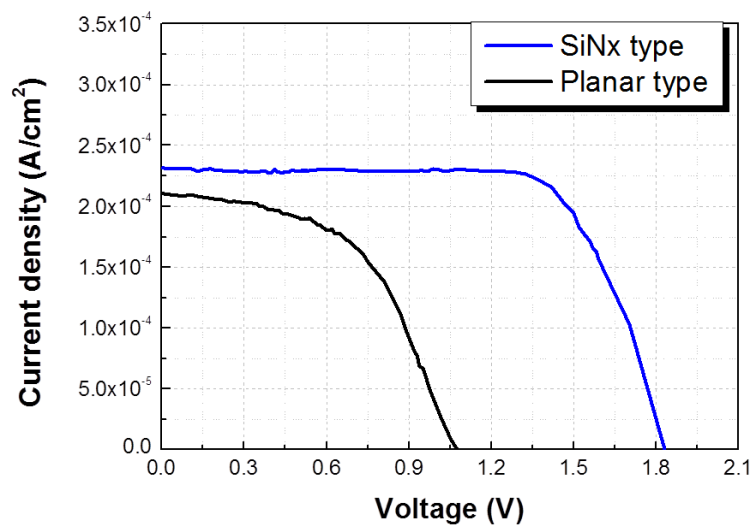


Figure 5.9 J-V curve of p-i-n InGaN/GaN SCs for planar and SiN_x-type

Table 5.1 SC performances of planar- and SiN_x-type p-i-n InGaN/GaN SCs

	Planar-type	SiN_x-type
V_{oc} (V)	1.08	1.82
J_{sc} (mA/cm²)	0.21	0.23
CE (%)	0.12	0.32
FF (%)	52.71	74.80

The results indicated that the overall photovoltaic properties of the SiN_x-type sample were superior to those of the planar-type sample. The increased J_{sc} of the SiN_x-type device might be primarily due to the reduction in dislocation density because both samples exhibited similar surface reflectivities and QCSEs, which are also known to affect J_{sc}. In this situation, reduced dislocation density, i.e., reduction in the number of NRCs, can lead to an increase in the carrier lifetime;¹⁴⁾ hence, the photogenerated current was readily collected by suppressing the recombination process. This recombination behavior was partly confirmed by the simulated recombination rates at zero-bias voltage for the planar- and SiN_x-type devices. As shown in Fig. 5.10, the rate of Shockley-Read-Hall recombination, originating due to the non-radiative recombination through defect states, is lower in SiN_x-type device than in the planar-type device due to lower dislocation density. This resulted in an improvement in the J_{sc} of the SiN_x-type device.

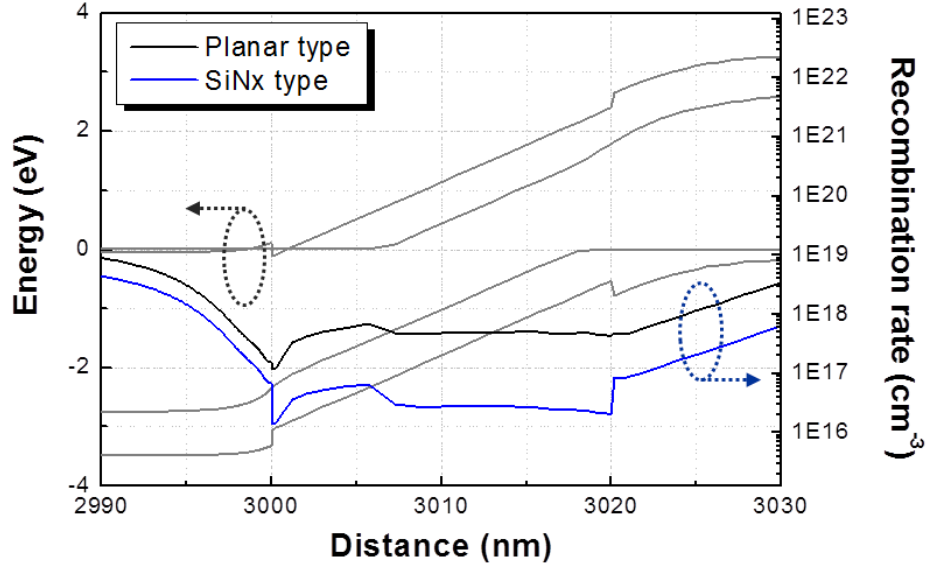


Figure 5.10 SRH recombination rate of p-i-n InGaN/GaN SCs for planar and SiN_x-type with band diagram

However, contrary to the J_{sc} properties, the difference in the V_{oc} between the planar- (1.08 V) and SiN_x-type devices (1.82 V) was unexpectedly larger, although both devices had the same bandgap energy of the InGaN layer. To explain this result, an ideal single-diode model that can describe the theoretical operation of most SCs was considered as follows:¹⁵⁾

$$J = J_{sc} - J_0 \left\{ \exp \left[\frac{q(V + JR_s)}{kT} \right] - 1 \right\} - \frac{V + JR_s}{R_{sh}} \quad (1)$$

where J is the output current density of the SC, J_0 is the saturation current density, q is electron charge, V is terminal voltage, k is Boltzmann's constant, T is absolute temperature, R_s is series resistance, and R_{sh} is shunt resistance. Thus, V_{oc} can be extracted from Eq. (1) by considering the V_{oc} measuring conditions (i.e., $J = 0$, negligible R_s) and written as

$$V_{oc} = \frac{kT}{q} \ln \left[\frac{J_{sc} - \left(\frac{V_{oc}}{R_{sh}} \right)}{J_0} \right] \quad (2)$$

Equation (2) indicates that V_{oc} increases with increasing J_{sc} as well as with decreasing J_0 and increasing R_{sh} . Thus, the values of R_{sh} and J_0 for both devices were examined (J_{sc} was already investigated). Figure 5.11 shows the leakage current measured under a reverse voltage of -5 V. Due to the decreased dislocation density, the leakage current of the SiN_x-type device (2.59×10^{-6} A) was lower than that of the planar-type device (1.35×10^{-5} A). This behavior occurred because the dislocations provided alternate current paths for the photogenerated current.¹⁶⁾

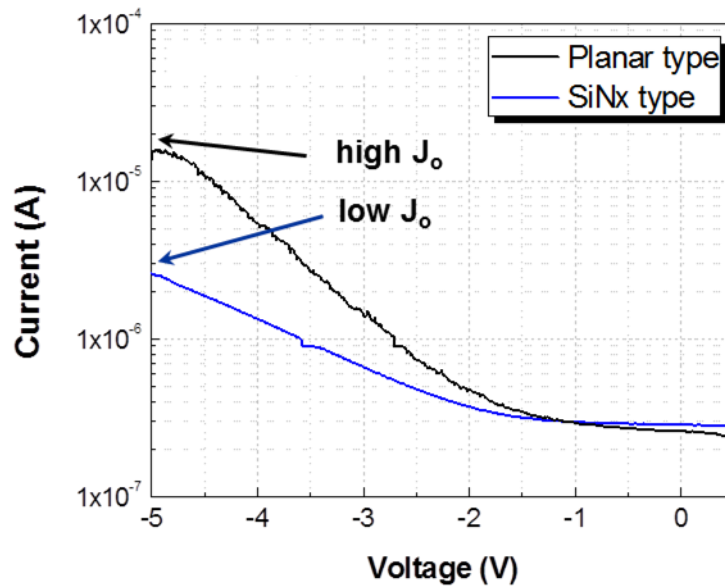


Figure 5.11 Leakage currents measured under a reverse bias voltage of -5 V for planar- and SiN_x-type devices

Thus, the R_{sh} value for the SiN_x-type device might be larger than that in the planar-type device due to a decrease in alternate current paths. The R_{sh} values for the planar- and SiN_x-type devices were determined to be 3.91×10^4 and $1.21 \times 10^5 \Omega\text{cm}^2$, respectively. All these factors contributed to a significantly larger V_{oc} in the SiN_x-type device compared to the planar-type sample. As for the V_{oc} properties, the difference in FF between the two devices

was also large (75% for the SiN_x-type device vs. 53% for the planar-type device); however, the In-fluctuation effect, which can decrease the FF value,¹⁷⁾ was stronger in the SiN_x-type device. This behavior could be explained by the V_{oc} properties because the maximum theoretical FF is expressed as¹⁸⁾

$$FF = \frac{V_{oc} - \ln(V_{oc} + 0.72)}{V_{oc} + 1} \quad (4)$$

As shown in Eq. (4), the value of V_{oc} is the critical factor in determining FF when other resistive effects on power loss are not considered. Thus, the increased FF of the SiN_x-type device was attributed to its elevated V_{oc}. Furthermore, a large difference in R_{sh} was observed for the two devices. When considering the power loss affected by R_{sh}, the relation between FF and R_{sh} can be written as

$$FF' = FF_0 \left(1 - \frac{1}{r_{sh}}\right) \quad \because \left(r_{sh} = \frac{R_{SH}}{R_{ch}}\right), \quad (5)$$

where FF' is the fill factor changed by R_{sh}, FF₀ is the fill factor unaffected by R_{sh}, r_{sh} is the normalized R_{sh}, and R_{ch} is characteristic resistance. Therefore, the increased value of R_{sh} for the SiN_x-type device also influenced the relative increase in FF.

5.4 Summary

The effects of dislocations on the performances of InGaN-based solar cells were investigated. The primary findings are summarized below.

- The solar cell structure was designed to focus on the effects of defects, and the as-grown samples confirmed its conditions.

- 1) GaN templates with lower dislocation densities were prepared by including a SiN_x insertion layer.

- 2) QCSE was almost negligible in both samples due to the low In-content.

- 3) Due to the relatively thick InGaN layer, In-fluctuation effect was observed in both samples.

- Higher dislocation density has the following effects:

- 1) Decreased short-current density due to increased non-radiative recombination

- 2) Increased reverse saturation current and shunt resistance

- 3) Decreased open-circuit voltage and fill factor

5.5 References

- 1) E. F. Schubert, *Light Emitting Diodes*, Cambridge University Press, New York, 2006.
- 2) S. Nakamura, G. Fasol, *The Blue Laser Diode: The Complete Story*, Springer, Berlin, 2000.
- 3) S. W. Feng, L. W. Tu, J. I. Chyi, H. C. Wang, *Thin Solid Films* **517**, 909 (2008).
- 4) J. Wu, W. Walukiewicz, K. M. Yu, J. W. Ager, E. E. Haller, H. Lu, W. J. Schaff, Y. Saito, Y. Nanishi, *Appl. Phys. Lett.* **80**, 3967 (2002).
- 5) I. Vurgaftman, J. R. Meyer, *J. Appl. Phys.* **94**, 3675 (2003).
- 6) A. David, M. J. Grundmann, *Appl. Phys. Lett.* **97**, 033501 (2010).
- 7) J. Q. Wu, *J. Appl. Phys.* **106**, 011101 (2009).
- 8) A. De Vos, *Endoreversible Thermodynamics of Solar Energy Conversion*, Oxford University Press, Oxford, 1992, p. 90.
- 9) P. Kozodoy, J. P. Ibbetson, H. Marchand, P. T. Fini, S. Keller, J. S. Speck, S. P. DenBaars, U. K. Mishra, *Appl. Phys. Lett.* **73**, 975 (1998).
- 10) M. J. Kappers, R. Datta, R. A. Oliver, F. D. G. Rayment, M. E. Vickers, C. J. Humphreys, *J. Cryst. Growth* **300**, 70–74 (2007).
- 11) R. C. Tu, C. C. Chuo, S. M. Pan, Y. M. Fan, C. E. Tsai, T. C. Wang, C. J. Tun, G. C. Chi, B. C. Lee, C. P. Lee, *Appl. Phys. Lett.* **83**, 3608 (2003).
- 12) Y. Cho, G. H. Gainer, A. J. Fischer, J. J. Song, S. Keller, U. K. Mishra, S. P. DenBaars, *Appl. Phys. Lett.* **73**, 1730 (1998).
- 13) T. Sugahara, M. Hao, T. Wang, D. Nakagawa, Y. Naoi, K. Nishino, S. Sakai, *Jpn. J. Appl.*

Phys. **37**, L1195 (1998).

14) J. J. Wierer, Jr., A. J. Fischer, D. D. Koleske, Appl. Phys. Lett. **96**, 051107 (2010).

15) W. De Soto, S. A. Klein, W. A. Beckman, Solar Energy **80**, 78 (2006).

16) J. S. Speck, S. J. Rosner, Physica B **273**, 24 (1999).

17) K. Y. Lai, G. J. Lin, Y. -L. Lai, Y. F. Chen, J. H. He, Appl. Phys. Lett. **96**, 081103 (2010).

18) M. A. Green, Solid-St. Electron. **24**, 788 (1981).

Chapter 6

Conclusion of this thesis

In this thesis, the effect of piezoelectric fields on carrier dynamics in InGaN-based SCs was first investigated. By changing the strain relaxation constants, we confirmed that a reduction in the angle of the energy band in the i-region due to the existence of P_{pz} led to significant current loss in the p-i-n $\text{In}_{0.1}\text{Ga}_{0.9}\text{N}$ SC structure, although the V_{oc} and J_{sc} were slightly improved. The current loss presented as a staircase-like feature in the I–V curve, and this feature was strongly correlated with the recombination process. Since the recombination rate was significantly affected by the shape of the energy band in the i-region caused by piezoelectric fields in the InGaN layer region, the amount of current loss can be supposed by the staircase-like feature. The current loss resulting from the piezoelectric fields became more dominant with increasing In-content in the InGaN layer. Thus, solutions that can eliminate the piezoelectric fields are needed to produce highly efficient SCs.

The optical and structural properties of semipolar (11-22) InGaN/GaN MQW SCs were investigated in comparison to those of the conventional (0001) polar structure. Under AM 1.5G and 1 sun illuminated conditions, the semipolar sample exhibited lower V_{oc} , higher J_{sc} , and increased FF compared to the polar sample (Fig. 1). Since V_{oc} , J_{sc} , and FF are strongly associated with properties such as defect density, surface roughness, P_{pz} , and the In-fluctuation effect, various structural properties were investigated. In low-temperature PL spectra, since defect-related emissions were highly emitted in the semipolar sample unlike the polar sample case, it could be confirmed that the semipolar sample contained higher defect density than the polar sample, which led to the lower V_{oc} value. The temperature-dependent

PL spectra also revealed that the semipolar sample had a higher defect density than the polar sample; the estimated IQE values for the semipolar and polar samples were approximately 19% and 40%, respectively. Moreover, in the AFM images, the semipolar sample showed a rough surface due to the formation of arrowhead-like features that typically form on the surface of the (11-22) GaN-based layer, while the polar sample revealed a relatively smooth surface. As the increased surface roughness of the p-type layer gave rise to enhanced light coupling, the semipolar sample showed a higher J_{sc} value. In the power-dependent PL spectra, the semipolar sample exhibited an almost constant peak wavelength with increasing excitation power density, whereas the peak wavelength of the polar sample showed a blue-shift of approximately 30 nm; this suggests that the P_{pz} effect was almost negligible in the semipolar sample. This reduced P_{pz} effect also might have increased the value of J_{sc} . In-fluctuation was observed in both samples by micro-PL mapping, although the effect was stronger in the polar sample. Therefore, the value of FF was increased in the semipolar sample.

Based on the above results, the P_{pz} effect on carrier dynamics in InGaN-based SC structures was investigated. By changing the strain relaxation constants, we confirmed that the reduced angle of the energy band in the i-region due to P_{pz} led to significant current loss in the p-i-n $In_{0.1}Ga_{0.9}N$ SC structure, although V_{oc} and J_{sc} were slightly improved. The current loss manifested as a staircase-like feature in the I-V curve, and this feature was strongly correlated with the recombination process. Since the recombination rate was significantly affected by the shape of the energy band in the i-region caused by piezoelectric fields in the InGaN layer region, the amount of current loss can be supposed by the staircase-like feature. This current loss caused by piezoelectric fields became more dominant with increasing In-content in the InGaN layer; thus, solutions that can eliminate the piezoelectric fields are needed to develop highly efficient SCs.

Appendix

[Numerical models for simulation]

1. Introduction

SCSim used in this study, especially in Chapter 3, is a software tool for design of heterostructures and modeling characteristics of SCs. For numerical analysis, mixed finite-elements method is employed in the program to calculate the nonlinear carrier transport equations coupled with the Poisson equation for the electric potential in a complex heterostructures of SCs. As a result, 2D simulation of carrier generation rate, band diagram, carrier recombination rate, electron and hole transport statistics, vertical and horizontal electric field distribution, voltage-current and power-current characteristics can be modeled by this software. Based on these calculations, various solar cell parameters such as V_{oc} , J_{sc} , FF and CE can also be estimated.

In this regard, basic physical models implemented in this simulation are described in this section.

2. Physical models

2.1 Light absorption

- Coordinate system: Since the software works with 2D geometry, the coordinate system is clarified as following:

- 1) Z-axis: it is oriented along the growth direction from bottom to top of the SC

structure

2) X-axis: it is oriented in horizontal direction of the SC structure

▪ Basic assumption

1) The direction of incident light is assumed to be normal to the surface of the SC structure.

2) Intensity distribution of incident light is also assumed to be uniform at fixed value of z coordinate within the setting area.

▪ Numerical model (Non-coherent light absorption model)

When we denote the total number of layers as N (In such a case, $N+1$ boundaries enumerated from top heterostructure to backside surfaces were formed), light intensities inside heterostructure layers are calculated as following:

$$I_j(z, E) = \frac{\{I_j^{(+)} \exp[\alpha_j(z - z_j)] + I_j^{(-)} \exp[-\alpha_j(z - z_j)]\}}{n_j} \quad (1)$$

where α_j is the absorption coefficient of the j -th layer, n_j is the refraction coefficient of the j -th layer, z_j is the j -th layer upper boundary coordinate, $I_j^{(+)}$ and $I_j^{(-)}$ are the sense of Poynting vectors at $z = z_j$ for the waves propagating against and along the z -axis, respectively, and E is the power.

By neglecting reflection at the inner layer boundaries (because the difference between refraction coefficients of the layers is generally not too large in commonly used solar cell heterostructures), magnitudes $I_j^{(+)}$ can be computed using the following relationship (when

the incident light has a power of 1 W/cm²).

$$I_1^{(+)} = \frac{1 - R_0}{1 - R_0 R_N E^2} \quad (2)$$

$$I_{j+1}^{(+)} = I_j^{(+)} \exp(-\alpha_j d_j) \quad (3)$$

$$E = \exp\left(-\sum_{j=1}^N \alpha_j d_j\right) \quad (4)$$

where R_0 and R_N are the reflection coefficients at the top (input) and bottom (backside) surfaces of the heterostructures, d_j is the thickness of the j -th layer.

Moreover, magnitudes can be further derived as following:

$$I_N^{(-)} = R_N I_N^{(+)} \exp(-2\alpha_N d_N) \quad (5)$$

$$I_{j-1}^{(-)} = I_j^{(-)} \exp(-\alpha_j d_j) \quad (6)$$

Therefore, when the transmission coefficient of the heterostructure is written as

$$T = (1 - R_N) E I_1^{(+)} \quad (7)$$

fraction of light absorbed in the heterostructure can be calculated by following equation.

$$A(E) = 1 - R(E) - T(E) = (1 - E)(1 + R_N E) I_1^{(+)} \quad (8)$$

2.2 Strain and polarization effect

Epitaxial layer of an arbitrary $\text{Al}_x\text{In}_y\text{Ga}_{1-x-y}\text{N}$ compound grown on the underlying layer with the lattice constant a_s and c_s are considered in this simulation. The lattice constants of the free-standing compound, a_E and c_E , are varied along the z -axis in accordance with the material composition and the Vegard's law as shown below.

$$a_E = a_{InN} \cdot y + a_{AlN} \cdot x + a_{GaN} \cdot (1 - x - y) \quad (9)$$

$$c_E = c_{InN} \cdot y + c_{AlN} \cdot x + c_{GaN} \cdot (1 - x - y) \quad (10)$$

where a_{AlN} , a_{GaN} , and a_{InN} are the lattice constants of the respective binary compound, x and y are the molar fractions of aluminum (Al) and indium (In) in $Al_xIn_yGa_{1-x-y}N$. Based on these relationships, the actual strained lattice constants of the layers are automatically computed as following:

$$a_R(z) = (1 - \xi) \cdot a_s + \xi \cdot a_E(z) \quad (11)$$

$$c_R(z) = (1 - \xi) \cdot c_s + \xi \cdot c_E(z) \quad (12)$$

where a_s is the actual lattice constant at the end of the underlying layer and ξ is the user-defined degree of the strain relaxation in the layer ($0 \leq \xi \leq 1$). When $\xi = 0$, the lattice constant in the layer is the same with the lattice constant at the end of the underlying layer. These lattice constants are used to calculate the lattice mismatch along x and y axis as described below:

$$\eta_x = \frac{(a_R - a_E)}{a_E} \quad (13)$$

$$\eta_y = \frac{a_R c_R}{\sqrt{(a_E c_R \cos \theta)^2 + (a_R c_E \sin \theta)^2}} - 1 \quad (14)$$

where θ is incline angle between the normal to the epitaxial layers (z -axis) and the hexagonal crystal axis.

To analyze the piezoelectric polarization, strain tensors generally having 4 non-zero components are used as defined below:

$$\varepsilon_{xx} = \eta_x \quad (15)$$

$$\varepsilon_{yy} = \eta_y \quad (16)$$

$$\varepsilon_{zz} = \frac{(B_{41}\eta_x + B_{42}\eta_y)A_{32} - (B_{31}\eta_x + B_{32}\eta_y)A_{42}}{A_{31}A_{42} - A_{32}A_{41}} \quad (17)$$

$$\varepsilon_{yz} = \frac{(B_{31}\eta_x + B_{32}\eta_y)A_{41} - (B_{41}\eta_x + B_{42}\eta_y)A_{31}}{A_{31}A_{42} - A_{32}A_{41}} \quad (18)$$

where

$$A_{31} = C_{11} \sin^4 \theta + (C_{13}/2 + C_{44}) \sin^2 2\theta + C_{33} \cos^4 \theta \quad (19)$$

$$A_{32} = [C_{11} \sin^2 \theta + (C_{13} + 2C_{44}) \cos 2\theta - C_{33} \cos^2 \theta] \sin 2\theta \quad (20)$$

$$A_{41} = \frac{1}{2} [(C_{11} - C_{33}) \sin^2 \theta + 2C_{44} \cos 2\theta + (C_{13} - C_{33}) \cos^2 \theta] \sin 2\theta \quad (21)$$

$$A_{42} = \left(\frac{C_{11} + C_{33}}{2} - C_{13} \right) \sin^2 2\theta + 2C_{44} \cos^2 2\theta \quad (22)$$

$$B_{31} = C_{12} \sin^2 \theta + C_{13} \cos^2 \theta \quad (23)$$

$$B_{32} = C_{13} (\sin^4 \theta + \cos^4 \theta) + \left(\frac{C_{11} + C_{33}}{4} - C_{44} \right) \sin^2 2\theta \quad (24)$$

$$B_{41} = \frac{C_{12} - C_{13}}{2} \sin 2\theta \quad (25)$$

$$B_{42} = \frac{1}{2} [C_{11} \cos^2 \theta - (C_{13} + 2C_{44}) \cos 2\theta - C_{33} \sin^2 \theta] \sin 2\theta \quad (26)$$

and C_{ij} are components of the elastic stiffness tensor given in the Voigt notation. By using these relations, z component of the total electric polarization can be computed as follows.

$$\begin{aligned} p_z^{tot} = & p^{spont} \cos \theta + \varepsilon_{xx} e_{31} \cos \theta + \varepsilon_{yy} \left[e_{31} \cos^3 \theta + \frac{e_{33} - e_{15}}{2} \sin \theta \sin 2\theta \right] \\ & + \varepsilon_{zz} \left[e_{33} \cos^3 \theta + \frac{e_{31} + e_{15}}{2} \sin \theta \sin 2\theta \right] + \varepsilon_{yz} [(e_{31} - e_{33}) \cos \theta \sin 2\theta + e_{15} \sin \theta \cos 2\theta] \end{aligned} \quad (27)$$

tensor.

2.3 Electron, hole and impurity statistics

Based on the parabolic dispersion law in the conductive zone, the respective electron concentration, n , is calculated as follow:

$$n = N_c \cdot \mathbf{F}_{\frac{1}{2}} \left(\frac{F_n - E_c + q\phi}{kT} \right) \quad (28)$$

where F_n is electron Fermi level, E_c is conduction band bottom, q is the electron charge, k is the Boltzmann constant, and T is temperature. Furthermore, Fermi integral of the ν -th order ($F_\nu(\xi)$) and the effective density of states in the conduction band (N_c) are also can be expressed as below:

$$F_\nu(\xi) = \frac{1}{\Gamma(\nu + 1)} \int_0^\infty \frac{x^\nu dx}{1 + \exp(x - \xi)} \quad (29)$$

$$N_c = 2 \left(\frac{m_n^{av} kT}{2\pi \hbar^2} \right)^{\frac{3}{2}} \quad (30)$$

where \hbar is the Plank constant, m_n^{av} is the averaged electron effective mass. Particularly, averaged electron mass as described below is used for calculation due to the conduction band anisotropy.

$$m_n^{av} = (m_n^a \sqrt{m_n^c})^{\frac{2}{3}} \quad (31)$$

Here, m_n^a and m_n^c are the effective masses along the a- and c-axes, respectively.

By considering the energy dispersion relationships $E_h(\vec{k})$ in each valence subband, hole concentration can also be calculated by using the equations as indicated below:

$$p_i = N [m_{h,i} F_{1/2}(\xi_i) + b_{h,i} F_0(\xi_i) + \gamma_{h,i} F_{3/2}(\xi_i)] \quad (32)$$

$$\xi_i = \frac{E_{v,i} - F_p - q\phi}{kT} \quad (33)$$

$$N = 2 \left(\frac{m_0 k T}{2\pi \hbar^2} \right)^{\frac{3}{2}} \quad (34)$$

Here, index i is corresponded to a number of subband, and parameters $m_{h,i}$, $b_{h,i}$, $\gamma_{h,i}$ are automatically defined using numerical results. As a result, a sum of p_i represents the total hole concentration in the simulation.

In addition, concentrations of ionized donors and acceptors, N_D^+ and N_A^- , are defined as following:

$$N_D^+ = \frac{N_D}{1 + g_D \exp\left(\frac{F_n - E_c + E_D + q\varphi}{kT}\right)} \quad (35)$$

$$N_A^- = \frac{N_A}{1 + g_A \exp\left(\frac{E_V + E_A - F_p - q\varphi}{kT}\right)} \quad (36)$$

where N_D are N_A the total impurity concentrations of donors and acceptors, g_D and g_A are the degeneracy factors, E_D and E_A are the activation energies of electrons and holes, and φ is electric potential.

2.4 Electric potential

By assuming that crystal hexagonal axis, c-axis, is oriented along the growth direction, 2D distribution of the electric potential (φ) can be derived from Poisson equation, as indicated below:

$$\varepsilon_{11}^* \frac{\partial^2 \varphi}{\partial x^2} + \frac{\partial}{\partial z} \left(\varepsilon_{33}^* \frac{\partial \varphi}{\partial z} \right) = q \cdot (n - p + N_A^- - N_D^+) + \frac{\partial P_z^{tot}}{\partial z} \quad (37)$$

Here, the effective dielectric constants, ε_{11}^* and ε_{33}^* , in Eq. 37 are defined as follow:

$$\varepsilon_{11}^* = \varepsilon_0 \varepsilon_{11} + \left(\frac{e_{15}^2}{C_{44}} \right) \quad (38)$$

$$\varepsilon_{33}^* = \varepsilon_0 \varepsilon_{33} + \left(\frac{e_{33}^2}{C_{33}} \right) \quad (39)$$

where ε_0 is inductive capacity of vacuum, ε_{11} and ε_{33} are the components of the dielectric tensor of material, respectively.

2.5 Electron and hole transport

2D carrier transport inside heterostructure can be expressed by following differential equations for Fermi levels:

$$\nabla \cdot (\mu_n n \nabla F_n) = -q(G - R) \quad (40)$$

$$\nabla \cdot (\mu_p p \nabla F_p) = +q(G - R) \quad (41)$$

where μ_n and μ_p are mobilities of electron and hole, and R is the recombination rate depending on the carrier concentration as below:

$$R = np \left\{ 1 - \exp\left(-\frac{F_n - F_p}{kT}\right) \right\} \cdot \left[\frac{1}{\tau_p n + \tau_n p} + B + C_n n + C_p p \right] \quad (42)$$

where τ_p and τ_n are non-radiative lifetimes of electron and hole, B is radiative recombination constant, C_n and C_p are Auger recombination coefficients. Here, non-radiative lifetimes ($\tau_{n,p}$) are computed by following equations:

$$\tau_n = \frac{\tau_n^{SR} \tau_n^{dis}}{\tau_n^{SR} + \tau_n^{dis}} \quad (43)$$

$$\tau_p = \frac{\tau_p^{SR} \tau_p^{dis}}{\tau_p^{SR} + \tau_p^{dis}} \quad (44)$$

where $\tau_{n,p}^{dis}$ and $\tau_{n,p}^{SR}$ are the components aroused by recombination on the dislocations and other defects, respectively. Moreover, non-radiative lifetime related to the dislocations, $\tau_{n,p}^{dis}$, are basically calculated by following equation:

$$\tau_{n,p}^{dis} = \frac{1}{4\pi D_{n,p} N_{dis}} \left\{ \ln \left(\frac{1}{\pi a^2 N_{dis}} \right) - \frac{3}{2} + \frac{2D_{n,p}}{aV_{n,p}} \right\} \quad (45)$$

where $D_{n,p}$ is the diffusion coefficient of electrons or holes, N_{dis} is the dislocation density, a is the lattice constant (radius of a dislocation core), and $V_{n,p}$ is the carrier thermal velocity. On the other hand, non-radiative lifetime caused by defects, $\tau_{n,p}^{SR}$, are specified by user directly.

2. Data base – used parameters

The following values are used for simulation.

	GaN	InN
Band structure properties		
Electron affinity (eV)	3.10	5.40
Bandgap in G-valley at 0K (eV)	3.507	0.690
Varshni parameter-alpha (eV/K)	0.909e-3	0.404e-3
Varshni parameter-beta (K)	830	454
Lateral electron mass (mo)	0.209	0.068
Longitudinal electron mass (mo)	0.186	0.065
Impurity		
Electron g-factor	2	2

Hole g-factor	4	4
Donor ionization energy (eV)	0.013	0.013
Acceptor ionization energy (eV)	0.170	0.170
Polarization		
Lateral lattice constant (nm)	0.3188	0.3540
Longitudinal lattice constant (nm)	0.5186	0.5705
Stiffness constant- C_{11} (GPa)	374	223
Stiffness constant- C_{12} (GPa)	140	115
Stiffness constant- C_{13} (GPa)	106	94
Stiffness constant- C_{33} (GPa)	395	200
Stiffness constant- C_{44} (GPa)	101	461
Piezoelectric constant- e_{33} (C/m ²)	0.65	0.43
Piezoelectric constant- e_{31} (C/m ²)	-0.33	-0.22
Piezoelectric constant- e_{15} (C/m ²)	-0.33	-0.22
Spontaneous electric polarization (C/m ²)	-0.029	-0.032
Other		
Electron mobility-low field (cm ² /V/s)	~400	~400
Hole mobility-low field (cm ² /V/s)	~50	~50
Radiative recombination constant (cm ³ /s)	$2.4e-11*(300/T)^{1.5}$	$6.6e-12*(300/T)^{1.5}$
Electron Auger recombination constant (cm ⁶ /s)	1e-31	2.5e-30
Hole Auger recombination constant (cm ⁶ /s)	1e-31	2.5e-30

Physical constants	
Boltzmann constant (eV/K)	8.6175e-5
Free electron mass- m_0 (kg)	9.1094e-31
Planck constant (J*s)	1.0546e-34
Elementary charge (C)	1.6022e-19
Absolute dielectric constant (A*s/V/m)	8.8542e-12
Absolute magnetic constant (V*s/A/m)	1.2566e-6
Velocity of light in vacuum (m/s)	2.9979e+8
Bohr radius (m)	0.5292e-10
Ridberg energy (eV)	13.606
Gravitation constant ($m^3/kg/s^2$)	6.6973e-11
Avogadro number (1/mol)	6.0221e+23
Ideal gas constant (J/K/mol)	8.3145
Stephan-Bolzmann constant ($W/m^2/k^4$)	5.6705e-8

Acknowledgments

Firstly, I would like to thank my supervisor Prof. Hiroshi Amano for giving me such great opportunity to study in Nagoya University. The Ph.D course at the Amano laboratory has been the most valuable time of my life. Because of his kindness concern and pertinent advices, I could learn a lot of things ranging from scientific knowledge to enthusiasm as a researcher. I believe that this wonderful experience will help me a lot in my future life. I would also like to thank Prof. Yoshio Honda who carefully advises me on research fields and academic works. His proper advices have been a great help to me during my Ph. D course. Also, I'd like to thank all the reviewers of my Ph. D (Prof. Kodo Kawase, Prof. Seiichi Miyazaki Dr. Masatomo Sumiya) for giving me significant advices and opinions. All the comments are really helpful to me to make up my thesis.

Special thanks are given to Prof. Okhyun Nam and CANS laboratory members (especially Dr. Jongjin Jang and Daehong Min) in Korea Polytechnique University. Due to their kindness supports, I could do my research more effectively. Moreover, I had a lot of help and support from all the members of the Amano Laboratory, particularly Eguchi san, Hosoe san, Tatsumi san, Kusimoto san and Usami san. I would like to express my special appreciation to them. Additionally, I would like to thank Siyoung and Hojun oppa who always help and encourage me a lot. Finally, I'd like to thank my family from the bottom of my heart for their understanding and support everything. Because of their kindness concern, I could finish the Ph. D course without any troubles. Really thanks again for all the people who helped me during my Ph. D course.

Achievement List

A. Publications – (* : First Author)

01) “Study of Enhanced photovoltaic behavior in InGaN-based solar cells by using SiNx insertion layer : Influence of dislocations”, **Seunga Lee***, Yoshio Honda, Hiroshi Amano, Jongjin Jang, Okhyun Nam, Japanese Journal of Applied Physics (2016) – *accepted*.

02) “Effect of piezoelectric field on carrier dynamics in InGaN-based solar cells”, **Seunga Lee***, Yoshio Honda, Hiroshi Amano, *Journal of Physics D: Applied Physics* **49**, 025103 (2016)

03) “Highly-ordered catalyst-free InGaN/GaN core-shell architecture array with expanded active area region”, Byung Oh Jung*, Si-Young Bae, Sang Yun Kim, **Seunga Lee**, Jeong Yong Lee, Dong-Seon Lee, Yoshihiro Kato, Yoshio Honda, and Hiroshi Amano, *Nano Energy* **11**, 294(2014).

04) “Correlation between Luminescence and Defects in Nonpolar and Semipolar InGaN/GaN Quantum Wells on Planar and Patterned Sapphire Substrates”, **Seunga Lee***, Geunho Yoo, Jongjin Jang, Youngjong Won, and Okhyun Nam, *Electron Material Letter* **10**, 67 (2014).

05) “Effect of defects on the luminescence in semipolar InGaN/GaN quantum wells on planar and patterned m-plane sapphire substrate”, **Seunga Lee***, Jongjin Jang, Kwan-Hyun Lee, Jung-Hwan Hwang, Joochel Jeong, and Okhyun Nam, *Physica Status Solidi A* **209**, 1526 (2012).

06) “Improvement of crystal quality and optical property in (11-22) semipolar InGaN/GaN LEDs grown on patterned m-plane sapphire substrate”, Jongjin Jang*, Kwnahyun Lee,

Junghwan Hwang, Joocheol Jung, Seunga Lee, Kyuho Lee, Bohyun Kong, Hyunghoun Cho, Okhyun Nam, *Journal of Crystal Growth* **361**, 166 (2012).

07) “Characterization of a-plane GaN layers grown on patterned r-sapphire substrate by metal organic chemical vapor deposition”, Geungo Yoo*, Hyunsung Park, Donghun Lee, Hyoungjin Lim, Seunga Lee, Bohyun Kong, Hyunkoun Cho, Hyoungwon Park, Heon Lee, Okhyun Nam, *Current Applied Physics* **11**, S90(2011).

08) “A Nonpolar a-Plane GaN grown on a Hemispherical Patterned r-Plane Sapphire Substrate”, Geungo Yoo*, Hyunsung Park, Hyoungjin Lim, Seunga Lee, Okhyun Nam, Younboo Moon, Chaerok Lim, Bohyun Kong, and Hyungkoun Cho, *Japanese Journal of Applied Physics* **50**, 042103(2011).

09) “Structural and optical characterization of (11-22) semipolar GaN on m-plane sapphire without low temperature buffer layer”, Sung-Nam Lee*, Hyunsung Park, Hyoungjin Lim, Seunga Lee, Okhyun Nam, *Phys. Stat. Solidi C* **7**, 2043 (2010).

B. International Conference Presentation – (* : Presenter)

01) “Photovoltaic Characteristics Dependence on Optical and Structural Properties in Semipolar (11-22) InGaN/GaN MQWs Solar Cells”, Seunga Lee*, Yoshio Honda, Hiroshi Amano, Jongjin Jang, and Okhyun Nam, *International Conference on Advanced Electromaterials : 2015/11/17~20 (Poster)*.

02) “Numerical Study of InGaN-based Solar Cell with Direction of Piezoelectric Field”,

Seunga Lee*, Yoshio Honda, Hiroshi Amano, *The 6th World Conference on Photovoltaic Energy Conversion: 2014/11/23-27 (Poster)*.

03) “Optical Characterization and Structural Investigation of GaN Nanorod Arrays and its Based InGaN/GaN MQWs Core-Shell Nanoarchitecture Arrays”, Byung Oh Jung, Si-Young Bae, **Seunga Lee**, Sang Yun Kim, Masataka Imura, Yoshio Honda, Hiroshi Amano, *Materials Research Society Spring Meeting & Exhibit :2014/04/21-25 (Poster)*.

04) “Effect of piezoelectric field on carrier dynamics in InGaN-based solar cells”, **Seunga Lee***, Yoshio Honda, Hiroshi Amano, *International Symposium on Advanced Plasma Science and its Applications for Nitrides and Nanomaterials: 2014/3/2-6 (Oral)*.

05) “Characteristics of Double Quantum Well structure of (11-22) semipolar InGaN Light Emitting Diodes”, Joocheol Jeong*, Chilsung Jung, Jinwan Kim, Kyungjae Lee, **Seunga Lee**, and Okhyun Nam, *International Conference on Metal Organic Vapor Phase Epitaxy : 2012/05/20-25 (Poster)*.

06) “Effect of Defects on the Luminescence in Semipolar InGaN/GaN Quantum Wells on Planar and Patterned M-plane Sapphire Substrate”, **Seunga Lee***, Jongjin Jang, Kwanhyun Lee, Junghwan Hwang, Joocheol Jeong, Okhyun Nam, *International Conference on Advanced Electromaterials: 2011/11/8~10 (Oral)*.

07) “Strain distribution in a-plane GaN grown on hemispherical patterned r-plane sapphire substrate”, **Seunga Lee***, Geunho Yoo, Hyunsung Park, Hyoungjin Lim, Okhyun Nam, *International Conference on Nitride Semiconductors : 2011/07/10-15 (Poster)*.

08) “Improvement of optical property and crystal quality in (11-22) semipolar InGaN/GaN LEDs grown on patterned m-plane sapphire substrate”, Jongjin Jang*, Kwanhyun Lee, Junghwan Hwang, **Seung-A Lee**, Kyuho Lee, Okhyun Nam, *International*

Conference on Nitride Semiconductors : 2011/07/10-15 (Poster).

09) “Characterization of Si-doped semi-polar GaN grown on m-sapphire by MOCVD”, Jongjin Jang*, Kwanhyun Lee, Donghun Lee, Junghwan Hwang, **Seunga Lee**, Sunnam Lee, Okhyun Nam, *International Union of Materials Research Societies – International Conference on Electronic Materials : 2010/08/22-27 (Poster).*

10) “Characterization of a-plane GaN layers grown on patterned r-sapphire substrate by MOCVD”, Geungo Yoo*, Hyunsung Park, Donghun Lee, Hyoungjin Lim, **Seunga Lee**, Bohyun Kong, Hyunkoun Cho, Hyoungwon Park, Heon Lee, Okhyun Nam, *International Union of Materials Research Societies – International Conference on Electronic Materials : 2010/08/22-27 (Oral).*

11) “Improvement of crystal quality in nonpolar and semipolar GaN layers grown on nanoporous template”, Donghun Lee*, Jongjin Jang, Geunho Yoo, Kwanhyun Lee, Hyunsung Park, Junghwan Hwang, Hyoungjin Lim, **Seunga Lee**, Bo-Hyun Kong, Hyung-Koun Cho, and Okhyun Nam, *International Union of Materials Research Societies – International Conference on Electronic Materials : 2010/08/22-27 (Poster).*

12) “Characterization of a-plane GaN layers patterned r-sapphire substrate by MOCVD”, Geunho Yoo*, Hyunsung Park, Donghun Lee, Hyoungjin Lim, **Seunga Lee**, *International Conference on Metal Organic Vapor Phase Epitaxy : 2010/05/23-28 (Poster).*

C. Domestic Conference Presentation – (* : Presenter)

01) “Effect of defects on the luminescence in semipolar and nonpolar InGaN/GaN quantum wells on sapphire substrate”, **Seunga Lee***, Jongjin Jang, Geunho Yoo, Kwanhyun Lee,

Junghwan Hwang, Hyoungjin Lim, Joocheol Jeong, Okhyun Nam, LED and Solid State Lighting Conference : 2012/08/29-30 (Oral).

02) “Characterization of semipolar (11-22) InGaN/GaN LED on patterned m-plane sapphire substrate”, Jongjin Jang*, Kwan-Hyun Lee, Jung-Hwan Hwang, Seunga Lee, Kyuho Lee, and Okhyun Nam, LED and Solid State Lighting Conference : 2011/04/11-12 (Oral).

03) “Characterization of a-plane GaN layers grown on patterned r-sapphire substrate by Metalorganic chemical vapor deposition”, Geungo Yoo*, Hyunsung Park, Donghun Lee, Hyoungjin Lim, Seunga Lee, Bohyun Kong, Hyunkoun Cho, Hyoungwon Park, Heon Lee, Okhyun Nam, LED and Solid State Lighting Conference : 2010/08/26-27 (Oral).